

Electronic Thesis and Dissertation Repository

---

3-6-2024 1:00 PM

## The Study of Titan's Surface using Impact Craters and Analogues

Jahnvi Shah, *University of Western Ontario*

Supervisor: Neish, Catherine D., *The University of Western Ontario*

A thesis submitted in partial fulfillment of the requirements for the Doctor of Philosophy degree in Geophysics

© Jahnvi Shah 2024

Follow this and additional works at: <https://ir.lib.uwo.ca/etd>



Part of the [Geology Commons](#), [Geomorphology Commons](#), and the [Geophysics and Seismology Commons](#)

---

### Recommended Citation

Shah, Jahnvi, "The Study of Titan's Surface using Impact Craters and Analogues" (2024). *Electronic Thesis and Dissertation Repository*. 9993.

<https://ir.lib.uwo.ca/etd/9993>

This Dissertation/Thesis is brought to you for free and open access by Scholarship@Western. It has been accepted for inclusion in Electronic Thesis and Dissertation Repository by an authorized administrator of Scholarship@Western. For more information, please contact [wlsadmin@uwo.ca](mailto:wlsadmin@uwo.ca).

## Abstract

Titan, Saturn's largest moon, is an icy world harbouring a subsurface water ocean, a substantial atmosphere, and a flowing liquid on its surface. These distinctive characteristics give rise to complex chemical reactions on Titan, and also render it akin to Earth in terms of its landforms and processes. This positions Titan as a key target for studying prebiotic chemistry. NASA's fourth New Frontiers mission, Dragonfly, is poised to explore Titan's surface in the 2030s. Dragonfly's primary study site will be Selk crater, a relatively fresh impact crater located in Titan's equatorial sand seas. Impact craters serve as valuable markers for comprehending how geological processes shape and modify Titan's surface. The central theme of this thesis revolves around investigating the impact cratering process on Titan, using remote sensing and numerical modeling techniques. Specifically, we seek to use the morphology and morphometry of Titan's impact craters to constrain the amount of erosion that has occurred there. Given Titan's similarities to Earth, we study terrestrial craters in radar images as analogues to constrain the crater population on Titan, and hence, its surface age. Furthermore, we explore the extent of erosion that may have occurred at Titan's craters by simulating the formation of fresh craters on Titan. These simulations investigate the influence of the thermal properties of methane clathrates on crater depths. These studies collectively contribute to a more nuanced understanding of the impact cratering process on Titan. The Dragonfly mission, in its exploration of Selk crater, will provide further insights into Titan's geological history and subsurface structure, refining the surface age and erosion constraints presented in this work. To support future operations in Selk crater, we conducted an analogue mission simulation using an Unoccupied Aircraft System and applied lessons learned to the currently planned strategies for Dragonfly.

## Keywords

Titan, impact cratering, surface processes, radar remote sensing, Earth, analogue studies, Dragonfly mission, science operations

## Summary for Lay Audience

Titan is Saturn's largest moon and the second largest moon in our solar system. It has a thick atmosphere and liquid flowing on its surface. In this sense, it is very similar to our planet Earth. However, Titan is a very cold place with an ice shell on its surface and an underground water ocean. These characteristics combine to sustain a water cycle much like on Earth, but with methane as the liquid. Weather on Titan works to reshape the planet's surface, especially the impact craters seen there. Impact craters are bowl-shaped depressions that form when asteroids travelling at high speeds collide with a planetary surface. These craters are good markers for studying how the surface of Titan changes over time. This work focuses on better understanding these impact craters and the information they provide about Titan. First, we study these craters to figure out how many might have been completely erased due to the erosion on Titan. This helps us to figure out how old Titan's surface might be. We, then, model what fresh craters might look like to estimate the level of erosion on Titan. Lastly, we examine drone images of a planetary analogue site on Earth to find strategies to better explore the Selk crater on Titan with NASA's Dragonfly spacecraft in the future.

# Co-Authorship Statement

**Chapter 1** was written by myself, with edits from Dr. Neish.

**Chapter 2** was written by myself with multiple rounds of edits from Dr. Neish. Co-authors C. D. Neish and S. Trozzo set up the crowdsourcing platform and helped with the survey data analysis. This work has been submitted to *Icarus* and is currently under review. It also incorporates some helpful feedback from two anonymous reviewers.

- **Shah J**, Neish CD, and Trozzo S (2023) An analogue study of impact craters on Titan: Implications for Titan's surface age. *Icarus* (*under review*).

**Chapter 3** was written by myself with edits from Dr. Neish. It is a modified article set to be submitted to the *Planetary Science Journal* for publication. The chapter incorporates science discussions from all the co-authors.

- **Shah J**, Neish CD, Wakita S, Soderblom JM, Johnson BC, and Steckloff JK. The effect of the crustal thermal gradient on fresh crater morphometries on Titan. *Planetary Science Journal* (*in prep*).

**Chapter 4** was written by myself with edits from Dr. Neish. This is a manuscript, currently in preparation, is intended to be submitted to the *Planetary Science Journal*. It incorporates data collected by and discussions from the co-authors and the RAVEN team. The draft is being developed as part of a larger special RAVEN issue, and some of the information presented in this chapter will be incorporated into the main RAVEN UAS mission summary paper. The summary paper will encompass details about mission development, as well as mission science observations and interpretations.

- **Shah J**, Carr BB, Varnam M, Hadland N, Voigt JRC, Seelos K, Neish CD, and Hamilton CW. Lessons learned from the Rover-Aerial Vehicle Exploration Network (RAVEN) mission simulation: Applications for future operational procedures for Unoccupied Aircraft Systems (UAS) missions. *Planetary Science Journal* (*in prep*).

**Chapter 5** was written by myself, with suggestions from Dr. Neish.

## Acknowledgments

First and foremost, I would like to thank my advisor, Dr. Catherine Neish. She took me on as a student – a student with an interest but very little experience in planetary science – and has guided me in this field for the past few years. She provided me with the opportunity to pursue topics I was most interested in. Beyond that, she always encouraged me to explore other ideas outside of my thesis, enriching my grad school experience. Thanks to her encouragement, I have been able to participate in many exciting projects throughout my time here at Western. I also appreciate her for fostering an inclusive and engaging lab environment, where a true sense of camaraderie exists among the members. On that note, I would like to acknowledge the support of present and past Neish lab members. A special shoutout to Leah and Ashka for not only being fantastic labmates but also amazing friends. To my Titan buddies, Josh and Reid, thank you for your company at Titan meetings.

I extend my thanks to my thesis advisory committee members Dr. Peter Brown and Dr. Jason Soderblom for their insightful feedback and engaging discussions. I also want to thank those who have served as my advisors and mentors in an unofficial capacity, their influence has been significant nonetheless. This is an opportunity for me to express my thanks to my past mentors as well, each of whom has played a role in shaping my journey.

I also wish to acknowledge the various agencies that have funded my thesis work and fieldwork opportunities. This includes the Technologies for Exo-Planetary Science (TEPS) NSERC CREATE program, Ontario Graduate Scholarship, Canadian Space Agency, Western Space Institute, and Western University.

One of the aspects I've enjoyed most about the grad school journey is collaborating with diverse teams. It's easy to become fixated on the thesis as a graduate student, but by working with different groups on various projects, I've gained diverse perspectives and approaches to doing science, ultimately making me a better researcher. My heartfelt thanks to the 2019 LPI summer interns, RAVEN team, Dragonfly team, and the Titan Impacts group.

I acknowledge the developers of iSALE-2D (<https://isale-code.github.io/>), including Gareth Collins, Kai Wünnemann, Dirk Elbeshausen, Tom Davison, Boris Ivanov, and Jay Melosh. I also thank Tom Davison, the developer of the pySALEPlot package which was used to create some plots in this work. I thank the ComputeCanada SHARCNET supercomputer facilities (and technical support) used to run the simulations in this thesis. A special thank you to Dr. Shigeru Wakita for showing me the ropes of iSALE.

I want to express my appreciation to my close friends Alexx and Sarah for their remote support, and willingness to listen to me whenever grad life became overwhelming. My gratitude to Apurva and Saranya, who have been the best of friends for the past ten years and my main support system. I thank my brother, parents, and extended family for their love and encouragement behind the scenes. Lastly, my gratitude to Ankit for being a constant source of support, but more importantly for the late-evening and weekend work company during the final stretch of my thesis.

This list is by no means exhaustive, and I want to thank everyone who has supported me on this journey, including those whose names may not appear here. Your support has been invaluable, and I am sincerely grateful. Thank you.

## Landmark Acknowledgement

I would like to acknowledge that the University of Western Ontario is situated on the traditional lands of the Anishinaabek, Haudenosaunee, Lūnaapéewak, and Attawandaron peoples. Western resides on lands associated with the London Township and Sombra Treaties of 1796 and the Dish with One Spoon Covenant Wampum. This land has perpetually been the home of these Indigenous Nations, and it is essential for us to consistently recognize and honor their enduring connection to the land we inhabit.

# Table of Contents

Abstract .....	ii
Summary for Lay Audience .....	iv
Co-Authorship Statement.....	v
Acknowledgments.....	vi
Table of Contents .....	viii
List of Tables .....	xii
List of Figures .....	xiii
List of Appendices .....	xix
Chapter 1 .....	1
1 Introduction .....	1
1.1 Titan .....	1
1.1.1 Exploration of Titan.....	2
1.1.2 Titan’s Atmosphere.....	6
1.1.3 Titan’s Surface .....	8
1.1.4 Similarities to Earth .....	11
1.2 Impact Cratering .....	13
1.2.1 Crater Formation.....	13
1.2.2 Crater Morphology.....	15
1.2.3 Crater Morphometry .....	17
1.2.4 Titan Craters.....	17
1.2.5 Terrestrial Craters .....	19
1.3 Remote Sensing .....	19
1.3.1 Radar Remote Sensing.....	20
1.4 Numerical Modelling .....	23



1.5 Summary .....	28
1.6 References .....	29
Chapter 2 .....	47
2 An Analogue Study of Impact Craters on Titan: Implications for Titan’s Surface Age .....	47
2.1 Introduction .....	47
2.2 Methodology .....	51
2.2.1 Crater Visibility Criteria .....	53
2.3 Results .....	56
2.3.1 Characterization of Visibility .....	56
2.3.2 Topography Data .....	61
2.3.3 Crowdsourcing Study .....	64
2.4 Discussion .....	67
2.5 Conclusions .....	71
2.6 References .....	73
Chapter 3 .....	79
3 The Effect of the Crustal Thermal Gradient on Fresh Crater Morphometries on Titan .....	79
3.1 Introduction .....	80
3.2 Methods .....	82
3.3 Results .....	85
3.3.1 Effect of Thermal Gradient .....	85
3.3.2 Effect of Ice Thickness .....	90
3.3.3 Effect of Impact Velocity .....	91
3.4 Discussion .....	91
3.4.1 Constraints on Erosion .....	91
3.4.2 Other Factors that Shallow Craters on Titan .....	94

3.4.3	iSALE Limitations .....	95
3.5	Conclusions.....	96
3.6	References.....	97
Chapter 4	.....	107
4	Lessons Learned from the Rover-Aerial Vehicle Exploration Network (RAVEN): Applications for Future Operational Procedures for Unoccupied Aircraft Systems (UAS) Missions.....	107
4.1	Introduction.....	108
4.1.1	Rover-Aerial Vehicle Exploration Network .....	109
4.2	Mission Development .....	110
4.2.1	Team Structure.....	112
4.2.2	Planning Procedures.....	113
4.2.3	Science Operations.....	114
4.3	Results.....	115
4.3.1	Mission Summary .....	115
4.3.2	Simulation Results .....	116
4.3.3	Ground-truthing Results.....	119
4.4	Discussion.....	121
4.4.1	Applications to Dragonfly.....	122
4.4.2	Limitations .....	125
4.5	Conclusions.....	126
4.6	References.....	128
Chapter 5	.....	133
5	Discussion and Conclusions.....	133
5.1	Discussion.....	133
5.1.1	Cratering as a Window into Surface Processes.....	133
5.1.2	Informing Operational Strategies for Dragonfly.....	135

5.2 Conclusions.....	136
5.3 References.....	137
Appendices.....	139
Curriculum Vitae .....	149

## List of Tables

Table 1: Comparison of Titan and Earth parameters. Modified from Collins (2005). .....	13
Table 2: Summary of input parameters (Bray et al., 2014 and references therein) .....	84
Table 3: Crater diameters and depths. Impact velocity fixed at 11 km/s and convective temperature is set to 255 K. ....	89
Table 4: Possible erosional rates [m/yr] for a ~80 km crater in different thermal gradients..	94

# List of Figures

Figure 1.1: SAR image of Selk crater (left) with the landing ellipse for Dragonfly shown in yellow. The geologic features Dragonfly will cover during its traverse from the landing site north to Selk crater is shown on the right. Figure modified from Barnes et al. (2021). ..... 5

Figure 1.2: A diagram illustrating Titan's methane cycle. Methane clathrates (green) serve as potential sources of methane. The cycle involves methane moving from pole to pole, forming lakes (blue). Throughout this cycle, increasing humidity facilitates periodic rainfall (red), although methane undergoes destruction due to radiation. Meanwhile, organic hydrocarbons (purple) are formed by photochemistry in the atmosphere and settle on the surface, potentially forming the dunes (orange). Figure from Lunine & Atreya (2008). ..... 7

Figure 1.3: Comparison of temperature fields in Titan's crust in the presence of a (a) 0 km and (b) 10 km thick methane clathrate layer. The white line represents the stagnant lid and the black contour lines correspond to temperature in Kelvin. Note that in the presence of a thick clathrate layer (b), warm material is brought closer to the surface. Figure adapted from Kalousová & Sotin (2020). ..... 8

Figure 1.4: Images of the Huygens landing site and the surrounding features taken from the Descent Imager/Spectral Radiometer (DISR). Insets (A-C) show the drainage networks and (D) shows the landing site with rounded clasts that are up to tens of centimeters long. Figure from Lopes et al. (2020). All images are courtesy of National Aeronautics and Space Administration (NASA)/Jet Propulsion Laboratory (JPL)/European Space Agency (ESA)/U. Arizona. .... 10

Figure 1.5: A global map of Titan's major geomorphologic units mapped using mainly SAR images, and other correlating datasets (including the Imaging Science Subsystem (ISS), Visible and Infrared Mapping Spectrometer (VIMS), and radiometry) for areas not covered by SAR. Figure modified from Lopes et al. (2020). ..... 11

Figure 1.6: Examples of similar terrains shaped by the hydrological processes present on both Titan (left panel) and Earth (right panel), as seen in radar images. (a-b) show shorelines of Kraken Mare and Chesapeake Bay. (c-d) show river channel and alluvial fans. (e-f) show

longitudinal sand dunes seen in Cassini Titan Flyby T-49 and in Namibia. (g-h) show the minimally degraded impact craters Sinlap and Barringer crater. Figure modified from MacKenzie et al. (2021)..... 12

Figure 1.7: Schematic cross-sections illustrating – (a) contact and compression stage, (b) excavation stage, and (c) modification stage – the three primary stages in the formation of simple (left) and complex (right) impact craters. Figure modified from Osinski et al. (2011). ..... 15

Figure 1.8: Schematic cross-sections illustrating the two classes of craters (a) simple and (b) complex. Figure modified from Osinski et al. (2011). ..... 16

Figure 1.9: Cassini RADAR images of craters of varying sizes on Titan. (i) is an image of the largest crater observed on Titan, Menrva (D ~ 425 km). Figure from Neish et al. (2013)..... 19

Figure 1.10: Radar backscatter as a function of surface roughness and incidence angle. (a) Smoother surfaces function as reflectors, diverting the radar signal away from the receiver and resulting in low backscatter. Rougher terrains scatter the signal in multiple directions, including back towards the sensor, thereby amplifying the recorded backscatter. In addition to surface roughness, the backscatter is dependent on incidence angle (b); all surface types tend to exhibit increased reflection at lower incident angles due to quasi-specular scattering. Figure modified from Farr (1993)..... 21

Figure 1.11: Illustration of a dinosaur jumping of a diving board (a) showing the differences between (b) Lagrangian and (c) Eulerian material descriptions. In (b) the Lagrangian formulation, material is fixed to a cell and the cell deforms under external forces. While in (c) the Eulerian setup, the material flows between the cells while the mesh remains fixed. Figure adapted from Collins (2002)..... 25

Figure 1.12: The mesh grid setup in iSALE is divided into a high resolution zone (shown in red) and an extension zone. The high resolution zone is large enough to cover an area in which the crater will form and has a constant cell size. In the extension zone, the cell size increases in a geometric fashion and thus decreases the total number of cells which helps to decrease computation time. The left boundary of the grid represents the axis of symmetry. In

this thesis, the left and right boundary conditions are set to free slip (green), top to outflow (purple), and the bottom is no slip (blue). Figure adapted from Potter (2012). ..... 27

Figure 2.1: (a) Cassini HiSAR global mosaic of Titan (Elachi et al., 2005; Stephan et al., 2009) showing 90 possible impact craters represented by red circles (modified from Hedgepeth et al., 2020). (b) A global map of 200 confirmed impact craters on Earth. Of the 200, 67 are buried (yellow) and 133 are non-buried (red) craters (Impact Earth Database). Circle size is scaled in proportion to the crater diameter. .... 51

Figure 2.2: (a) PALSAR image (© JAXA, METI 2007) of the ~17 km diameter Lawn Hill crater in Queensland, Australia showing a radar bright rim/ejecta blanket and a radar dark crater floor. Characteristic field photographs of the (b) radar bright rim and (c) radar dark floor are shown on the right, with an arm and a lens cap for scale, respectively. Lawn Hill crater photo credits: R. Lorenz, J. Radebaugh, and J. Barnes. .... 54

Figure 2.3: (a) Sentinel-1 image of the fresh 1.2 km diameter Barringer crater in Arizona, U.S.A and (b) PALSAR image (© JAXA, METI 2007) of the degraded 12 km diameter Gweni-Fada crater in Chad. (c) Cassini RADAR image of the fresh Sinlap crater and (d) the degraded Soi crater on Titan, both ~80 km in diameter (Neish et al., 2016). (e) Sentinel-1 image of the 12 km diameter Karla crater in Russia and (f) Sentinel-1 image of the 60 km diameter Beaverhead crater in Montana, U.S.A. The green dashed circles represent the nominal location of these “invisible” craters. .... 55

Figure 2.4: Examples of ambiguous craters: (a) Sentinel-1 image of the 70 km diameter Charlevoix crater in Quebec, Canada and (b) the 13 km diameter Zhamanshin crater in Kazakhstan. The green dashed circles represent the nominal location of the craters. The Charlevoix and Zhamanshin craters were eventually characterized as visible and not visible, respectively. .... 57

Figure 2.5: Latitudinal variation in the radar visibility of craters. (a) The distribution of visible and non-visible craters compared to the total number of non-buried craters for 10° latitude bins. (b) The variation in percent of radar visibility of craters for 10° latitude bins. 59

Figure 2.6: The distribution of visible and non-visible craters compared to the crater diameter. .... 60

Figure 2.7: The distribution of visible and non-visible craters compared to the impact target rock type..... 60

Figure 2.8: The distribution of visible and non-visible craters compared to the estimated ages of the craters..... 61

Figure 2.9: (a) Sentinel-1 radar image and (b) a 30 m resolution SRTM DEM of the 12 km diameter Vargeão Dome crater located in Brazil, overlaid on the Sentinel-1 radar image. (c) Sentinel-1 radar image and (d) a 30 m resolution SRTM DEM of the 16 km diameter Aorounga crater located in Chad. The craters are indicated with white arrows in (b) and (d). The circular feature located on a topographic high in the upper left in (d) is the Emi Koussi volcano..... 63

Figure 2.10: Percentage of correct answers for the R (a), X (b), and Y (c) parameters, of those participants who drew a crater in the study area. We used three different cut-offs for the radius measurement (within 10, 15, and 20% of the true crater radius) and two different cut-offs for the location measurements (within 1 and 2 km of the true crater location). The locations of only 6/16 craters and the radii of only 5/16 craters were easily found by our participants (i.e., >50% correct, shown by the dotted red line). ..... 67

Figure 2.11: The distribution of visible and non-visible craters compared to the age of the target rock. Note that the age of the target rock is different than the age of the crater shown in Figure 2.8. .... 71

Figure 3.1: Schematic of the model setup depicting how the thermal gradient of the ice crust affects the interior structure. Increasing thermal gradient (from left to right) of the ice crust brings warm material closer to the surface (Kalousová and Sotin, 2020). The 10 K/km case is representative of thermal properties in the presence of methane clathrates. The black dashed line represents the material boundary between the ice crust and the ocean (which varies from 50 to 150 km in depth for our models). ..... 85

Figure 3.2: Time series of crater formation for a 5 km diameter impactor hitting an ice crust with thickness of 50 km and thermal gradient of 5 K/km. Colour indicates the temperature in Kelvin..... 87



Figure 3.3: Crater diameters and depths for varying thermal gradients. The blue circles represent a thermal gradient of 3 K/km, yellow squares a gradient of 5 K/km, and red triangles a gradient of 10 K/km. .... 88

Figure 3.4: Time series of crater formation for a 10 km diameter impactor hitting an ice crust with thickness of 50 km and thermal gradient of 10 K/km. Colour indicates the temperature in Kelvin and the solid black line represents the material boundary between the ice crust and the water ocean. .... 89

Figure 3.5: Crater diameters and depths for varying ice shell thickness. The thickness is represented by the marker shape (circle = 50 km, square = 100 km, triangle = 150 km). The thermal gradient is set to 3 K/km and the impactor size is varied from 2 to 5 km. .... 90

Figure 3.6: Model output depths of ‘fresh’ craters compared to observed depths on Titan with Cassini data from Hedgepeth et al. (2020). The blue circles represent a thermal gradient of 3 K/km, yellow squares a gradient of 5 K/km, and red triangles a gradient of 10 K/km. The black diamonds represent Cassini observed crater depths. .... 92

Figure 4.1: (a) A schematic of the DJI Matrice 600 UAS with custom landing gear and scoop (with swappable jaws). (b) DJI Matrice 600 with the sampling scoop and (c) DJI Matrice 300 with the P1 camera landed in the field site. .... 112

Figure 4.2: Map showing the UAS landing sites (in green) and flight paths (in orange) with the sol number annotated, overlain on the UltraCam-Xp pre-mission basemap. .... 115

Figure 4.3: (a) Sol 102 UAS grounded image of a feature interpreted to be a rotated lava flow crust. (b) A zoomed in and stretched version of image (a). (c) Field image of the same feature. .... 118

Figure 4.4: Sol 111 UAS grounded image on the lava flow. .... 118

Figure 4.5: Select UAS images of the sandsheet in the study area showing large ripples made up of two different (light and dark-toned) sediments. .... 120

Figure 4.6: (a) Image acquired with the UAS microimager on Sol 105 of the lava flow compared to (b) the field image of a similar feature. .... 121

Figure 4.7: (a) Schematic of the DragonCam layout on the Dragonfly spacecraft. Each blue region is a different component of the DragonCam suite. (b) A labelled schematic of DragonCam with the locations of the different cameras. This exact configuration is subject to change. Credit: David Napolillo and Magda Saina/APL..... 124

Figure 4.8: Types of aerial flights planned for Dragonfly surface operations. Scout flights (blue) are used to identify future landing sites. Jump flights (orange) are used to exit the local exploration region. Leapfrog flights (purple) are used to scout the next landing site, flying over a previously scouted landing site and then returning to land there. Credit: APL. .... 125

## List of Appendices

Appendix A: iSALE asteroid input file .....	139
Appendix B: iSALE material input file .....	141
Appendix C: Characteristics of all 132 non-buried terrestrial craters. The last three columns are the characterizations made in this study regarding the crater's visibility in radar (C-band and L-band) and DEM. ....	142
Appendix D: Results of the Zooniverse crowdsourcing campaign for 16 craters (plus 4 controls). For reference, in four areas with no craters (1) 35.3% of 34 users, (2) 61.3% of 31 users, (3) 64.7% of 34 users, and (4) 25.8% of 31 users identified no craters. ....	148

# Chapter 1

## 1 Introduction

Icy satellites in our solar system, particularly those hosting a water ocean like Titan, Europa, and Enceladus, have captivated the planetary science community due to their unique geologic histories and the potential to harbour life (e.g. Nimmo and Pappalardo, 2016; Hendrix et al., 2019; Hand et al., 2020). These planetary bodies exhibit geological and chemical processes both similar to and distinct from those observed on terrestrial worlds. For example, on the surface of Titan, we observe Earth-like dunes and rivers (e.g. Lorenz et al., 2006; Le Gall et al., 2011; Burr et al., 2013; Neish et al., 2016). In contrast, signs of viscous relaxation of the icy surface are evident on Ganymede (e.g., Dombard and McKinnon, 2006). To better comprehend these processes, it is crucial to study surface markers, such as impact craters, that capture the evolution of these phenomena. The focus of this thesis is on studying the impact cratering process on Titan. Understanding and constraining the impact of these processes on the surface contribute to a better understanding of Titan's geologic history and evolution. This comprehensive understanding not only provides insights into other icy worlds but also enhances our understanding of terrestrial worlds, including Earth. In this chapter, I present a broad overview of impact cratering and the methods by which we studied them in this thesis.

### 1.1 Titan

Titan is the largest moon of Saturn, and the second largest moon in the solar system after Ganymede. Titan is an icy world thought to possess a ~100 km thick ice crust overlaying a liquid water ocean (Mitri and Showman, 2008; Nimmo and Bills, 2010; Collins and Johnson, 2014). It has a thick, nitrogen-rich atmosphere, with a few percent methane (Lindal et al., 1983; Tomasko et al., 2005; Coustenis, 2014; Hörst, 2017). Titan's atmosphere, and its surface, also harbour complex organic compounds (e.g. Gupta et al, 1981; Lorenz et al., 2008), resulting from reactions of solar and cosmic radiation with molecules in Titan's atmosphere (Sagan and Khare, 1979; Sagan and Thompson, 1984; Krasnopolsky et al., 2014). This combination forms the basis for a complex climate system

on Titan, contributing to the formation of diverse surface features such as sand dunes, methane river networks, lakes, and seas (Lunine and Atreya, 2008; Lopes et al., 2020). The ongoing interplay between the atmosphere and surface makes Titan one of the most chemically rich and astrobiologically significant places in the solar system (Raulin, 2008), and thus a captivating subject of scientific inquiry and exploration.

The investigation of Titan's astrobiological potential is the primary objective of National Aeronautics and Space Administration's (NASA) fourth New Frontiers mission to Titan, Dragonfly (Turtle et al., 2020). Dragonfly is a rotorcraft lander that aims to study the chemistry, surface geology, and atmosphere of Titan, with one of its prime study sites being Selk crater, one of the largest and freshest craters on Titan (Neish et al., 2018; Turtle et al., 2020). To aid in our preparations for the Dragonfly mission, this thesis focuses on enhancing our understanding of the impact cratering process on Titan and associated surface processes. In turn, this will offer enhanced insights into Titan as a whole, its methane cycle, and the co-evolution of its surface and methane-rich atmosphere.

### 1.1.1 Exploration of Titan

Titan was first discovered by a Dutch astronomer named Christiaan Huygens in 1655. However, detailed exploration of Titan only began in the 1900s with the discovery of methane in its atmosphere (Kuiper, 1944). In the 1970s and 1980s, the Pioneer 11 and Voyager spacecraft were able to take a closer look at Titan's atmosphere, but they could not see past the haze to observe its surface. Further telescopic studies continued in the late twentieth century, but the most detailed observations of Titan came from the Cassini-Huygens mission.

The Cassini-Huygens spacecraft, a joint NASA-ESA (European Space Agency) mission, was launched in October 1997 and reached the Saturnian system in July 2004 (Coustenis and Hirtzig, 2009). The primary mission goals were to explore Titan and its atmosphere, Saturn, and the Saturnian ring-moon system (European Space Agency, 1988; Matson et al., 2003). The spacecraft was made up of two main components: the Cassini orbiter and the Huygens probe. The orbiter was equipped with 12 instruments focused on studying the entire Saturnian system. Key instruments in this suite for surface imaging

included the Imaging Science System (ISS), Visible and Infrared Mapping Spectrometer (VIMS), and the Radio Detection And Ranging (RADAR) instrument, designed to function at visible, infrared, microwave, and radio wavelengths (Brown et al., 2004; Elachi et al., 2004; Porco et al., 2004). Throughout its mission, the Cassini orbiter conducted a total of 127 flybys of Titan. The Huygens probe, equipped with six instruments, was specifically designed to study Titan's atmosphere (European Space Agency, 1988; Lebreton and Matson, 2003), landing on its surface in January 2005 (Lebreton et al., 2005). A few of the descent images and interpretations of the Huygens landing site will be discussed later in **Section 1.1.3**. Even after the wealth of data delivered by the Cassini-Huygens mission, there is much more of Titan to explore. Given the intricate climate system that gives rise to Earth-like features on its surface, further exploration is necessary to gain a better understanding of this icy moon.

#### 1.1.1.1 Future Exploration of Titan

The Cassini-Huygens mission provided a wealth of scientific insights into Titan. However, much remains to be explored, particularly regarding Titan's chemistry and surface. Consequently, there is an upcoming mission to Titan, with the hope for more to follow in the future. With these new missions, there arises a need for a renewed approach to mission design and operations.

NASA's fourth New Frontiers mission, Dragonfly, marks the first return to Titan since Cassini-Huygens (Lorenz et al., 2021). Dragonfly, a rotorcraft lander, leverages Titan's dense atmosphere to explore various sites on its surface. While alternative aerial exploration strategies, such as balloons and airplanes (Lorenz, 2008; Levine and Wright, 2005; Barnes et al., 2012), have been proposed for Titan, these designs would pose challenges in accessing surface materials. Consequently, a lander with aerial mobility, specifically a rotorcraft, is deemed a more efficient approach. Titan's low surface gravity and higher atmospheric density compared to Earth make heavier-than-air mobility highly efficient on Titan (Lorenz, 2000, 2001).

The Dragonfly mission has five primary science goals: 1) investigate prebiotic chemistry by sampling Titan's surface, 2) gain insights into Titan's methane cycle, 3)

conduct further studies on Titan's geology, 4) explore areas where water and organics may have mixed, and 5) identify biosignatures to enhance our understanding of Titan's astrobiology and habitability (Barnes et al., 2021). To achieve these objectives, Dragonfly will be equipped with a comprehensive suite of instruments: 1) a **camera** suite (DragonCam), 2) a **geophysics** and **meteorology** package (DraGMet), 3) a **drill** for **acquisition of complex organics** (DrACO) and transporting them to 4) a **mass spectrometer** (DraMS), and 5) a **gamma-ray** and **neutron spectrometer** (DraGNS) for determining bulk surface composition (Barnes et al., 2021).

Dragonfly will land in the interdunes of the Shangri-La sand sea, a relatively flat, smooth, and rock-free area chosen to minimize landing risks (Lorenz et al., 2021). Spectral observations of Titan's interdunes suggest the likely presence of water-ice gravels (Barnes et al., 2008; Le Gall et al., 2011; Bonnefoy et al., 2016; Niemann et al., 2005; Tomasko et al., 2005; Zarnecki et al., 2005; Lorenz et al., 2006; Keller et al., 2008; Williams et al., 2012; Lorenz, 2014; Karkoschka & Schröder, 2016). This landing site offers Dragonfly the opportunity to sample both organic-rich and water-ice-rich materials (Barnes et al., 2021). Dragonfly will then travel north, studying the dunes along the way, ultimately reaching Selk crater, its primary study site (**Figure 1.1**).

Selk is a relatively fresh 80 km diameter impact crater, exhibiting spectral signatures of water-ice and organics in both the crater floor and its surrounding area (Soderblom et al., 2010; Lorenz et al., 2021). Numerical simulations suggest that impact melt could have been deposited within the crater, making Selk an ideal location to sample previously melted water ice (Artemieva & Lunine, 2003; Wakita et al., 2023; Barnes et al., 2021). Overall, Selk crater is a candidate site for addressing Dragonfly's science goals, providing an opportunity to sample various surface materials and contributing to our understanding of the impact cratering process on Titan, which is the focus of this thesis.

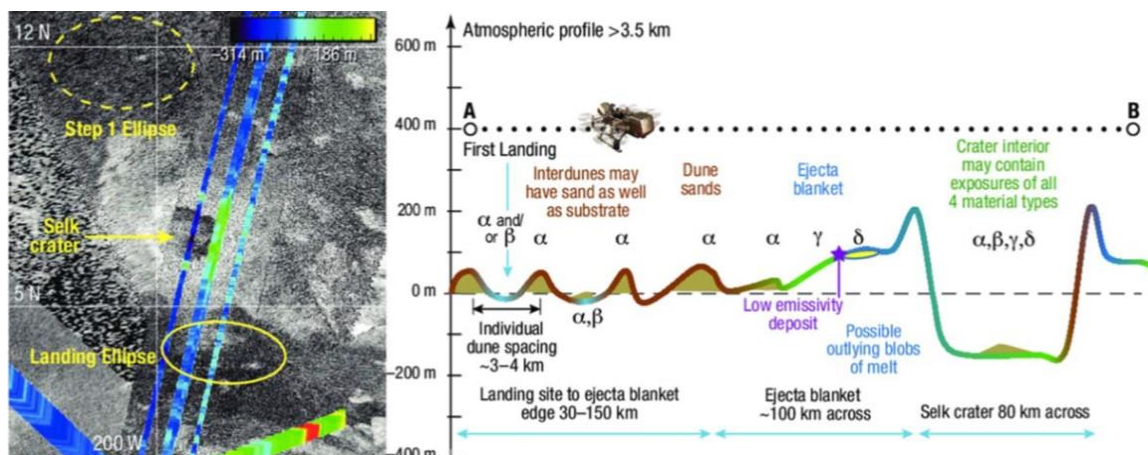


**Figure 1.1: SAR image of Selk crater (left) with the landing ellipse for Dragonfly shown in yellow. The geologic features Dragonfly will cover during its traverse from the landing site north to Selk crater is shown on the right. Figure modified from Barnes et al. (2021).**

#### 1.1.1.1.1 Mission Design and Operations

Dragonfly represents a novel approach to planetary surface exploration, engaging in both in-flight and landed operations. Traditionally, in-situ surface exploration has been confined to landers and rovers, exemplified by missions such as the Viking landers, Mars Exploration Rovers (Spirit and Opportunity), the Curiosity rover, and the Perseverance rover. The recent deployment of the Ingenuity helicopter, as part of the Mars 2020 mission, serves as a technology demonstration to inform future Unoccupied Aircraft Systems (UAS) style missions to Mars (Balaram et al., 2021). Consequently, operational strategies for a UAS-based mission, similar to Dragonfly, are not fully developed or tested. This gap is where simulated mission operations in planetary analog terrains come into play.

The Rover-Aerial Vehicle Exploration Network (RAVEN<sup>1</sup>), funded through NASA's Planetary Science and Technology through Analog Research (PSTAR) program, is designed to develop new planetary mission designs that integrate Unoccupied Aircraft

<sup>1</sup> <https://raven.lpl.arizona.edu>



Systems (UAS) and rovers. The goals of the RAVEN project are to test three mission architectures: 1) rover-only (Gwizd et al., 2023), 2) UAS-only (Shah et al., 2023) (both completed in 2022), and 3) a combined rover-UAS (completed in 2023) to enhance the scientific output of sample return missions to Mars. Specifically, the aim is to test different science operations strategies at a Mars analogue site located at the Holuhraun lava flow-field in Iceland (Hamilton et al., 2015, 2023; Voigt et al., 2023). For the scope of this thesis, we report only on operational results from the UAS-only mission simulation (Shah et al., 2023) and its potential applications for the Dragonfly mission.

### 1.1.2 Titan's Atmosphere

Exploration of Titan, before and including the Cassini-Huygens mission, has yielded valuable information about its atmosphere. The existence of Titan's atmosphere was initially proposed in the early 1900s and later confirmed following the spectroscopic identification of methane on Titan (Comas Solá, 1908; Kuiper, 1944). Ground-based infrared telescopic observations offered additional insights into the atmospheric composition and structure, revealing a greenhouse effect (e.g. Morrison et al., 1972; Danielson et al., 1973; Trafton, 1972; Gillett et al., 1973; Gillett, 1975; Hörst, 2017 and references therein). Quantitative measurements of Titan's atmosphere were obtained from the Voyager spacecraft, demonstrating that the atmosphere primarily consists of nitrogen (~98%) with a small percentage of methane (~2% in the stratosphere at an altitude ~250 km) (Lindal et al., 1983; Coustenis, 2014; Tomasko et al., 2005; Flasar et al., 2005; Bézard, 2014). Voyager also unveiled a variety of organic molecules in Titan's atmosphere, resulting from complex photochemical processes (Hanel et al., 1981; Kunde et al., 1981). Solar radiation interacts with atmospheric molecules, ionizing and dissociating them. These particles then recombine to form heavy complex organic compounds (Waite, 2005; Tomasko et al., 2005; Hörst, 2017), which form a haze layer around Titan that scatters visible light.

The presence of methane and organic compounds in Titan's atmosphere gives rise to a methane-based "hydrological" cycle (**Figure 1.2**). While the source of methane could be primordial, the ongoing destruction of methane in the atmosphere over a timescale of  $10^7$ - $10^8$  years suggests an additional source from the interior (Lunine & Atreya, 2008).

Methane is thought to have been released through outgassing from Titan's interior in the past, replenishing atmospheric methane (Choukroun et al., 2010; Choukroun and Sotin, 2012; Tobie et al., 2006). Tobie et al. (2006) presents a theoretical evolution of Titan's interior involving multiple methane outgassing events. Initially, during the overturn of Titan's initial core, the outgassing of methane produces a thick layer of methane clathrate on the surface (Sloan, 1998; Tobie et al., 2006). Methane clathrate, and more broadly clathrates, are ice lattices with trapped compounds; methane clathrates exhibit different rheological and thermal properties compared to water ice (Durham et al., 2010; **Figure 1.3**). The low conductivity of the clathrate layer insulates and warms the ocean, resulting in methane release. The presence of methane clathrate on Titan's surface and its associated thermal properties will be further discussed in **Chapter 3**.

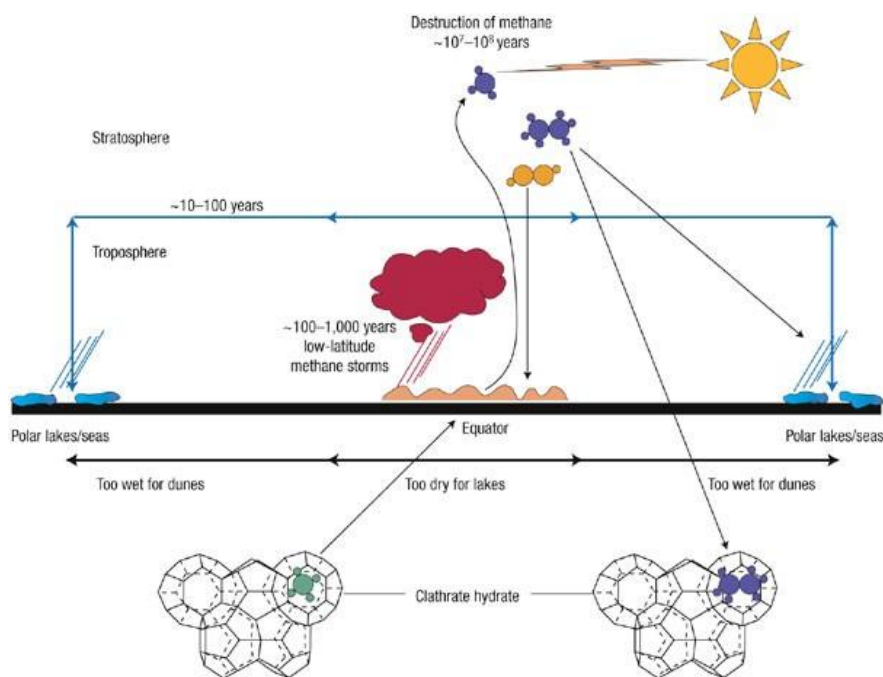


**Figure 1.2: A diagram illustrating Titan's methane cycle. Methane clathrates (green) serve as potential sources of methane. The cycle involves methane moving from pole to pole, forming lakes (blue). Throughout this cycle, increasing humidity facilitates periodic rainfall (red), although methane undergoes destruction due to radiation. Meanwhile, organic hydrocarbons (purple) are formed by photochemistry in the atmosphere and settle on the surface, potentially forming the dunes (orange). Figure from Lunine & Atreya (2008).**

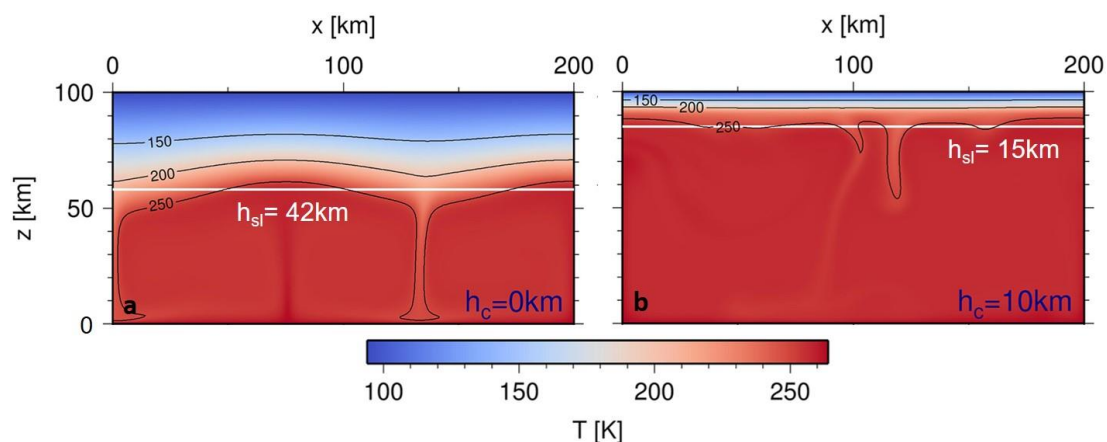


**Figure 1.3: Comparison of temperature fields in Titan’s crust in the presence of a (a) 0 km and (b) 10 km thick methane clathrate layer. The white line represents the stagnant lid and the black contour lines correspond to temperature in Kelvin. Note that in the presence of a thick clathrate layer (b), warm material is brought closer to the surface. Figure adapted from Kalousová & Sotin (2020).**

### 1.1.3 Titan’s Surface

Titan's methane-based hydrologic cycle (Hayes et al., 2018) shapes one of the most geologically diverse surfaces in the solar system (Lopes et al., 2020). The initial glimpses of Titan’s surface were provided by the Cassini-Huygens mission. The Huygens landing site is inferred to be a dry riverbed with a bedrock primarily composed of water ice (Tomasko et al., 2005; **Figure 1.4**). The Descent Imager/Spectral Radiometer (DISR) images revealed river channels and rounded pebbles of water ice, likely eroded due to the fluvial nature of the site (Lorenz, 2006; Tomasko et al., 2005). Cassini observations also revealed a vast network of lakes and seas of hydrocarbons on Titan, primarily concentrated in the polar regions (Birch et al., 2017). Specifically, fluvial networks cover 10% of Titan’s surface (Burr et al., 2009; Lorenz et al., 2008). Cassini data suggests a wide range of fluvial morphologies, including channels with liquid present that are hundreds of meters deep (Burr et al., 2013, 2009; Poggiali et al., 2016). These fluvial environments of Titan serve as a record of both past and current climate conditions and surface evolution processes (Birch et al, 2018; Turtle et al., 2018).

Another significant component of the surface is a thin layer of small (micron-sized) organic haze particles likely sourced from Titan's atmosphere (Attkinson et al., 2010; Janssen et al., 2016; Lorenz, 2006). Compositional data from Cassini suggests that the dunes are similar in composition to these organics, but each sand particle is ten million times larger in volume (Le Gall et al., 2011; Lorenz, 2006; Soderblom et al., 2007; Barnes et al., 2015). The dunes, hundreds of kilometers long and ~100 m in height (Lorenz et al., 2006; Neish et al., 2010), wrap around Titan's equator. They resemble the size and morphology of linear dunes on Earth and constitute the second-most extensive unit on Titan's surface after the plains unit (Lopes et al., 2020; see **Figure 1.5**).

Impact craters also dot Titan's surface, covering less than 1% of its total area (Lopes et al., 2020). The craters exhibit evidence of aeolian and fluvial erosional processes (Neish & Lorenz, 2012; Neish et al., 2013; Neish et al., 2016; Hedgepeth et al., 2020). There is some latitudinal variation in their distribution; most are situated near the equatorial region and there is a scarcity of craters near the poles, likely due to fluvial erosion and impacts into current and former marine environments (Neish et al., 2014, 2016). Compositional signatures of craters suggest a mixture of water ice and organics (Neish et al., 2015; Solomonidou et al., 2020).

Titan also features topographically high formations known as hummocky terrains, consisting of mountain chains and isolated terrains (Malaska et al., 2016; Lopes et al., 2020). Radio and microwave signals show high scattering and low emissivity in these areas, suggesting a composition of water-ice-rich materials (Barnes et al., 2007). These terrains are believed to be exposed parts of Titan's icy crust (Lopes et al., 2010).

Two other geomorphologic units also exist on Titan: labyrinth and plains. The labyrinth terrain comprises highly incised plateaus located in the higher latitudes. Cassini data suggests that the unit is locally elevated and is composed of organics (Elachi et al., 2005, Lopes et al., 2020). The last and most extensive unit, covering 65% of Titan's surface, is the plains unit. (Lopes et al., 2020). These plains are thought to be composed of a layer of organic-rich material of unknown thickness and lack notable topographic relief

(Lopes et al., 2016). **Figure 1.5** shows the latitudinal and surface area distribution of the six geomorphologic units on Titan's surface.

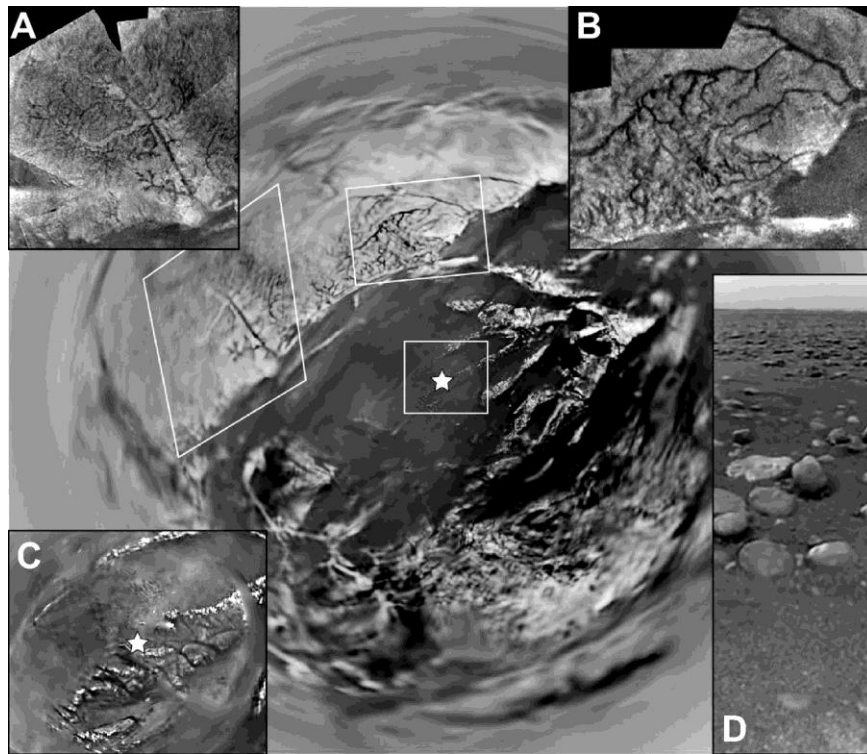


**Figure 1.4: Images of the Huygens landing site and the surrounding features taken from the Descent Imager/Spectral Radiometer (DISR). Insets (A-C) show the drainage networks and (D) shows the landing site with rounded clasts that are up to tens of centimeters long. Figure from Lopes et al. (2020). All images are courtesy of National Aeronautics and Space Administration (NASA)/Jet Propulsion Laboratory (JPL)/European Space Agency (ESA)/U. Arizona.**

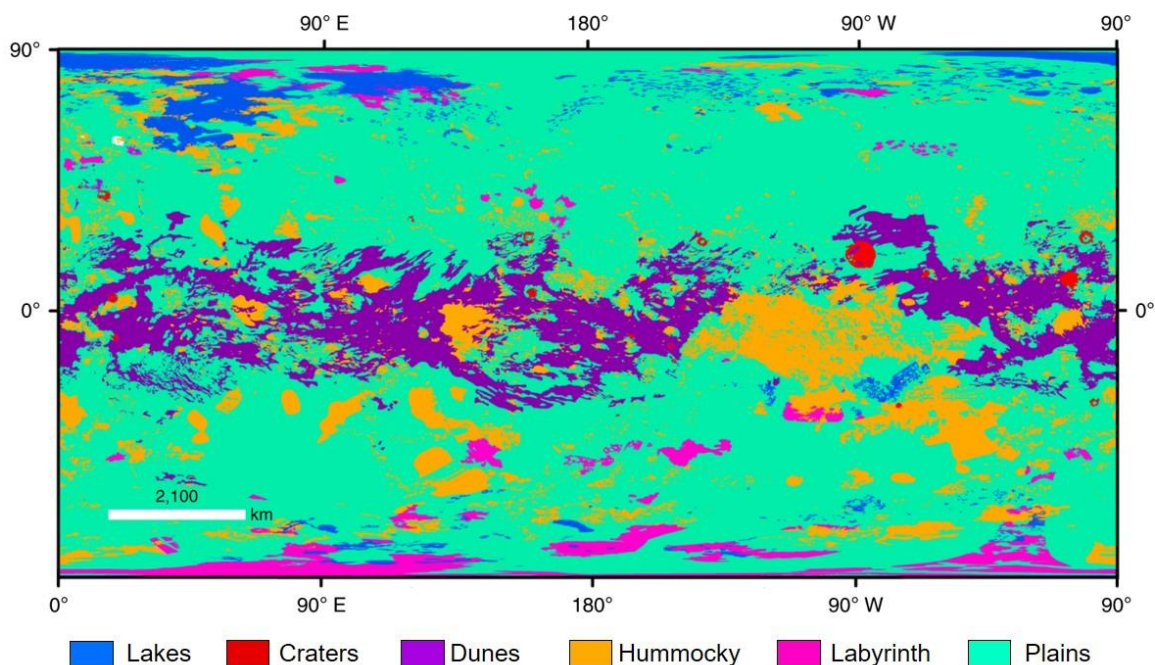


**Figure 1.5:** A global map of Titan’s major geomorphologic units mapped using mainly SAR images, and other correlating datasets (including the Imaging Science Subsystem (ISS), Visible and Infrared Mapping Spectrometer (VIMS), and radiometry) for areas not covered by SAR. Figure modified from Lopes et al. (2020).

#### 1.1.4 Similarities to Earth

The interaction of Titan’s atmosphere with its surface, resulting from its hydrological cycle (Hayes et al., 2018), produces landforms similar to those found on Earth (MacKenzie et al., 2021). **Figure 1.6** illustrates select examples of terrains observed on both Earth and Titan, ranging from lakes to craters. Of note are the similarities in crater degradation processes that work to modify and erase impact craters on both worlds. This similarity makes Earth a strong analogue for studying impact craters and their degradation processes on Titan. The following table (**Table 1**) summarizes the high-level comparisons between Earth and Titan that are relevant to the work in this thesis. The two planets share a thick, nitrogen-rich atmosphere and a surface fluid. They differ most significantly in gravity and surface composition.

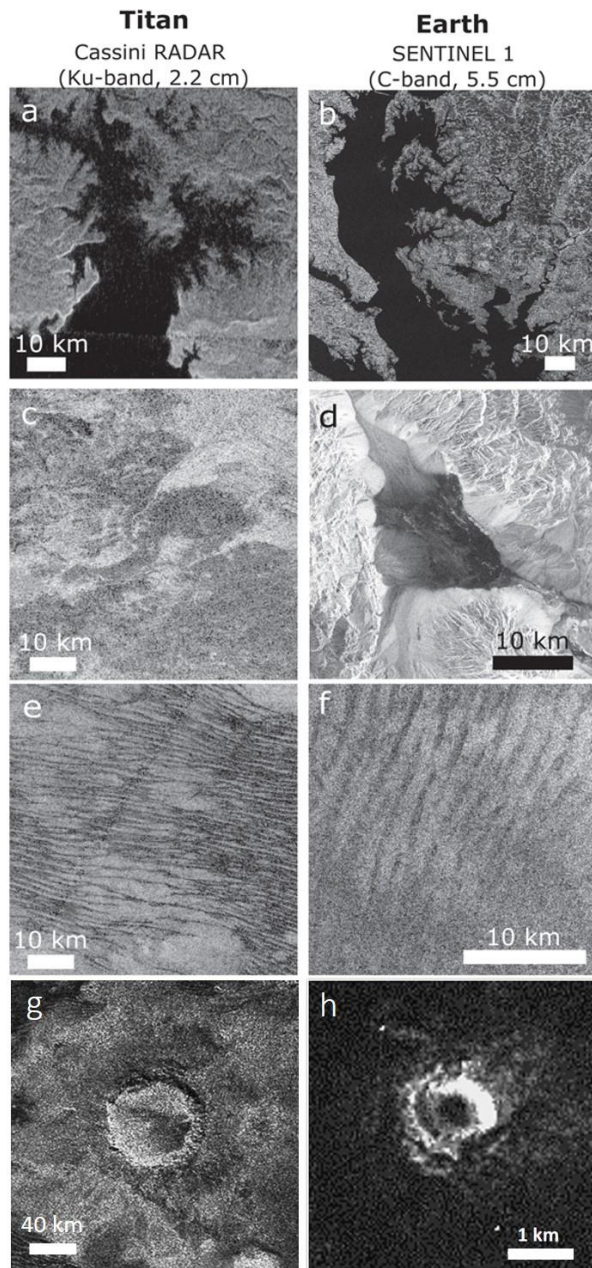


**Figure 1.6: Examples of similar terrains shaped by the hydrological processes present on both Titan (left panel) and Earth (right panel), as seen in radar images. (a-b) show shorelines of Kraken Mare and Chesapeake Bay. (c-d) show river channel and alluvial fans. (e-f) show longitudinal sand dunes seen in Cassini Titan Flyby T-49 and in Namibia. (g-h) show the minimally degraded impact craters Sinlap and Barringer crater. Figure modified from MacKenzie et al. (2021).**

**Table 1: Comparison of Titan and Earth parameters. Modified from Collins (2005).**

	<b>Titan</b>	<b>Earth</b>
<b>Surface fluid</b>	Methane	Water
<b>Atmosphere composition</b>	95% nitrogen, 2% methane (in the stratosphere)	78% nitrogen, 21% oxygen, 1% other gases
<b>Atmosphere scale height<sup>a</sup> (km)</b>	15 – 50	5 – 8
<b>Surface pressure (bar)</b>	1.5	1
<b>Crustal composition</b>	Water-ice, methane clathrate	Silicate
<b>Surface gravity (m/s<sup>2</sup>)</b>	1.35	9.8

<sup>a</sup>Flasar et al. (2014); Hörst (2017)

## 1.2 Impact Cratering

Impact craters are roughly circular depressions formed when an asteroid or comet collides with the surface of a planetary body at hypervelocities (Melosh, 1989). Impact cratering is a fundamental geologic process that modifies all planetary bodies with solid surfaces throughout the solar system. The distribution and morphology of craters provide information about the physical and chemical properties of a planetary surface, as well as its age. Thus, impact craters serve as important geological tools with which we can better understand the interior structure and surface processes of planetary bodies (Melosh, 1989; Osinski & Pierazzo, 2012).

### 1.2.1 Crater Formation

Impact craters form when projectiles travelling at hypervelocities (many kilometers per second) collide with a planetary surface (Gault et al., 1968; Melosh, 1989). The impact releases high levels of energy and pressure in a short amount of time (on the order of seconds) resulting in compression and excavation of the target material. Crater formation occurs in three stages that overlap in time slightly as the crater forms on the order of minutes.

The first stage of formation, contact and compression (**Figure 1.7a**), begins when the projectile comes in contact with the target surface. The surface compresses as the kinetic energy of the impactor converts into shockwaves that propagate into the target, dissipating with distance. When the shockwave reaches back to the projectile, it is reflected



as a tensional wave (rarefaction) (Grieve et al., 2014; Melosh, 1989, 2011). This rarefaction wave includes melt in the projectile. In the region of the highest shock pressure, the target material melts and/or vaporizes (Ahrens & O'Keefe, 1972; Grieve et al., 1977). The target material will only melt if high enough shock pressures are reached in order to induce incipient and total melt for a given material. Moving away from the impact site, the dissipating shockwave melts target material, and eventually transitions into brittle damage and fracturing of the target (Osinski et al., 2012). The compression stage comes to a close when the shockwave reaches back to the projectile; this rarefaction wave also vaporizes and/or melts the projectile (Melosh, 1989; Melosh, 2012).

The excavation stage of crater formation (**Figure 1.7b**) is composed of the opening of the deep bowl-shaped cavity, also known as the transient cavity, as a result of the rarefaction wave (Melosh, 1989). It is during this stage that target material is excavated and transported outside of the transient crater rim; these are defined as impact ejecta deposits. The excavation flow comes to a stop as the kinetic energy of the shockwave depletes and is unable to move material against its own weight (gravity-dominated cratering) or the cohesive strength of the material (strength-dominated cratering) (Kenkmann et al., 2012). At this stage, the transient cavity also stops growing; the resulting size of the cavity depends on many factors such as the impactor velocity and target material, but is approximately 10-20 times the impactor diameter (Osinski et al., 2012).

The modification stage (**Figure 1.7c**) is the last stage of crater formation. It begins when the transient cavity reaches its maximum horizontal extent, at which point the material motion shifts from outward to inward. This stage concludes when significant motion ceases. The duration of this stage depends on the impact energy and the strength of the target material, but typically lasts around 15-20 minutes for a crater of approximately 100 kilometers in size (Kenkmann et al., 2012). The extent of modification that occurs ultimately determines the resulting crater's morphology. The timeline of excavation and modification stages overlap as during this process, the transient cavity continues to expand horizontally but stops deepening. Excavation flow refers to the material moving away from the impact center, which opens the transient cavity. In contrast, modification flow entails

material moving in the opposite direction, closing the transient cavity. The primary force driving the cavity's collapse is gravity.

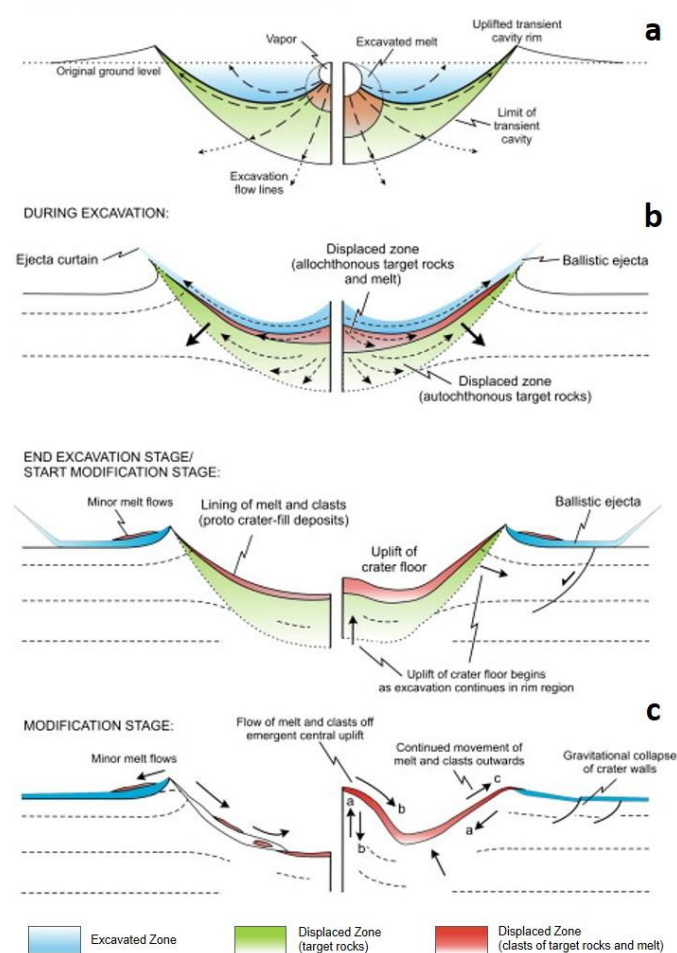


**Figure 1.7: Schematic cross-sections illustrating – (a) contact and compression stage, (b) excavation stage, and (c) modification stage – the three primary stages in the formation of simple (left) and complex (right) impact craters. Figure modified from Osinski et al. (2011).**

## 1.2.2 Crater Morphology

Crater morphology is primarily determined by the crater size and falls into two categories: simple and complex craters (Dence, 1965; see **Figure 1.8**). Simple craters are bowl-shaped with a raised rim, forming a parabolic profile (Kenkmann et al., 2012).

Complex craters contain uplifted crater floors which commonly forms central uplifts, but can also form peak rings or more complex topography. Complex craters, being larger than simple craters, experience significant wall slumping; their transient cavity is extensively altered during the modification stage due to ejecta being deposited inside the final crater rim. Additionally, complex craters may also contain central pits, which are elliptical depressions in the crater center. These pits may form due to vapourization of subsurface volatiles on planetary bodies such as Mars and Ganymede (Carr et al., 1977; Passey and Shoemaker, 1982; Barlow, 2010; Senft and Stewart, 2009). The central pits can also form due to the drainage of impact melt into the fractured ice beneath the impact crater; this theory works only for targets made of ice because silicate impact melt would freeze before a large volume is able to drain into the fractures (Elder et al., 2012). Furthermore, complex craters can take on a less constrained shape known as multi-ringed basins. The immense size of these craters results in the complete collapse of their walls, obliterating much of the original rim and creating rings where the walls have slid downwards (Melosh 1989; Osinski & Pierazzo, 2012).

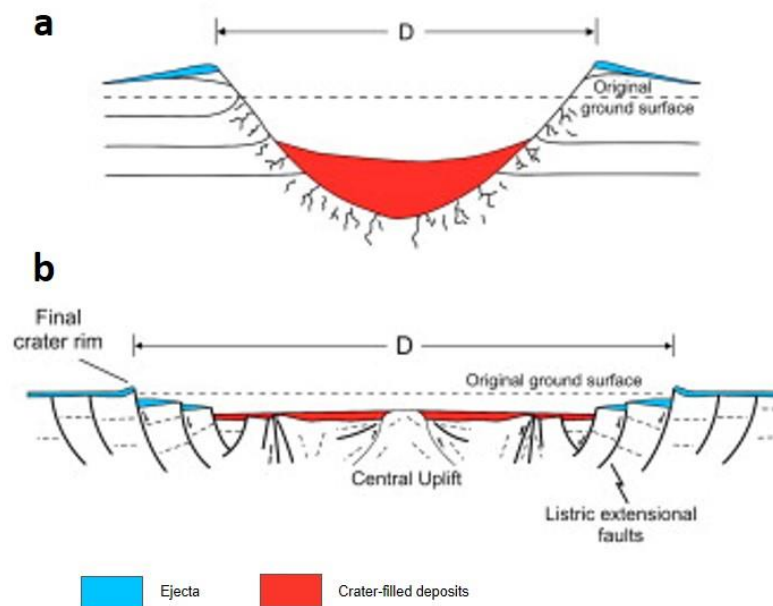


**Figure 1.8: Schematic cross-sections illustrating the two classes of craters (a) simple and (b) complex. Figure modified from Osinski et al. (2011).**

### 1.2.3 Crater Morphometry

Crater morphometry is defined by the quantitative measurements of crater dimensions. Morphologic features such as a crater's diameter, rim-to-floor diameter, rim-to-surface heights, wall slopes can be subjected to morphometric analysis. As mentioned above, craters can exhibit different morphologies, ranging from simple to complex to multiring; this transition is unique for each planetary body (Bray et al., 2008; Schenk, 2002, 1989). The transition diameter is mainly governed by gravity, followed by the planet's interior thermal structure (Melosh, 1989; Schenk, 2002; Turtle and Pierazzo, 2001). A warmer interior will allow the material to be more ductile, resulting in plastic deformation compared to brittle deformation or faulting (Turcotte and Schubert, 2014). This is relevant for icy moons like Titan because the thermal structure determines the degree of viscous relaxation a crater undergoes, consequently influencing the final crater morphology and morphometry (Durham et al., 2010; Schurmeier and Dombard, 2018). The thermal structure also plays an important role in determining the initial size and depth of a crater (**Chapter 3**).

### 1.2.4 Titan Craters

There are a total of 90 possible impact craters on Titan, as observed by the Cassini mission (Hedgepeth et al., 2020). The crater sizes on Titan range from 3 to 400 kilometers in diameter. **Figure 1.9** is a collage of some craters on Titan observed with Cassini's RADAR instrument. As mentioned in **Section 1.2.3**, the transition from simple to complex craters is primarily dictated by gravity (Melosh and Ivanov, 1999; Pike, 1980), but also target material (Schenk, 1991; Schenk et al., 2004). On Titan, the transition diameter from simple to complex craters is expected to be approximately 2–3 km (cf. Schenk, 2002). However, due to atmospheric shielding breaking up impactors, the smallest craters on Titan are anticipated to have a diameter of around 2 km (Korycansky and Zahnle, 2005), as observed with Cassini. Given that this represents the transition diameter, Titan lacks craters exhibiting a simple morphology (Soderblom et al., 2010). Titan's atmosphere decelerates and breaks up impactors less than 1 km in diameter, resulting in a dearth of impact craters less than ~20 km in diameter (Artemieva and Lunine, 2003).

Craters on Titan undergo modifications due to both endogenic and exogenic processes. Endogenic processes such as tectonics and viscous relaxation likely occur on a longer-term timescale for icy bodies. Viscous relaxation, resulting from the insulating effect of the large sediment cover, plays a role in modifying the larger craters (Bland et al., 2017; Dombard and McKinnon, 2000, 2006; Schurmeier and Dombard, 2018). Although, future studies will investigate the role of a methane clathrate layer that insulate and warm the surface enough for viscous relaxation to occur. However, it is thought that the primary mode of crater degradation on Titan is through exogenic processes, namely fluvial erosion and aeolian infilling. Erosion due to sand infill is likely more prominent compared to fluvial erosion, given the global distribution of crater depths and their observed morphologies (Neish et al., 2016, 2013). Craters located in the equatorial region, covered by sand seas, will experience the most modification due to aeolian infilling (Neish et al., 2015; Werynski et al., 2019). Outside the equatorial regions, there will likely be more fluvial erosion, especially near the poles, where rainfall is more frequent (e.g. Burr et al, 2013). There is also evidence of seas of liquid hydrocarbons near the poles, both in the present day and the recent past (e.g. Lunine et al., 1983; Mitri et al., 2007; Stofan et al., 2007; Lopes et al, 2008; Hayes et al., 2016). Craters formed in these shallow marine environments may not exhibit shapes recognizable from orbit (Collins and Wünnemann, 2005; Neish and Lorenz, 2014; Wakita et al., 2022). In addition to the poles, there is evidence of fluvial erosion in lower latitudes as well, seen through the absence of central peaks and pits in craters on Titan (Neish et al., 2016), and their decreased rim height compared to similar craters on Ganymede (Hedgepeth et al., 2020). Craters on Earth exhibit similar signs of degradation through aeolian and fluvial erosion (e.g. Grieve, 1987; Grant & Schultz, 1993; Grant, 1999).

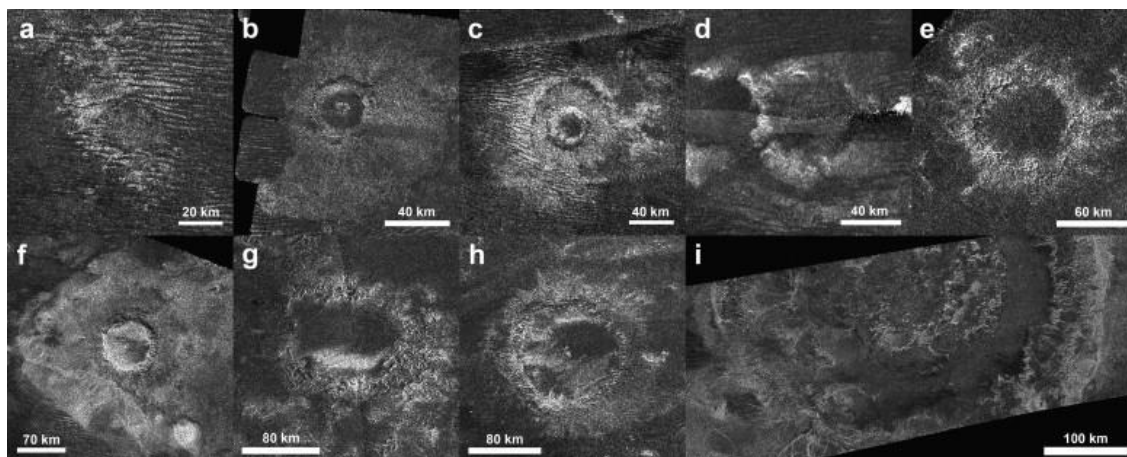


**Figure 1.9: Cassini RADAR images of craters of varying sizes on Titan. (i) is an image of the largest crater observed on Titan, Menrva (D ~ 425 km). Figure from Neish et al. (2013).**

### 1.2.5 Terrestrial Craters

There are currently 200 confirmed impact structures on Earth, as validated through remote sensing and field studies (Osinski & Grieve, 2019; Kenkmann, 2021; Osinski et al., 2022). However, numerous craters are extensively eroded and buried, suggesting there are more structures on Earth that have yet to be identified. Furthermore, considering that two-thirds of Earth's surface is covered by oceans and seas, it is possible that additional craters exist but remain undetectable. Erosional processes, including aeolian, fluvial, and biogenic factors, also contribute to the degradation of these craters. Unlike Titan, Earth also experiences tectonic deformation as a major force acting to erase or obscure craters (Martino et al., 2019).

## 1.3 Remote Sensing

One method through which we can study these impact craters on other planetary bodies is remote sensing. It involves using incident electromagnetic radiation to target a surface of interest and analyzing the reflected or emitted energy. Remote sensing methods, such as satellite imagery, provide global or regional information about planetary surfaces. It presents a quicker and more efficient way to map a surface, compared to traditional field mapping techniques, which are more time consuming, expensive, and sometimes

inaccessible. As such, it is an important tool in planetary science used to study surfaces and atmospheres of planetary bodies in our solar system and beyond.

Passive remote sensing systems have an external source of energy or radiation, typically the sun. As a result, passive remote sensing is only conducted when the sun is illuminating the target of interest. In contrast, active remote sensors have their own light source and can thus better control how the target of interest is illuminated.

### 1.3.1 Radar Remote Sensing

Radio detection and ranging (radar) is a remote sensing technique that produces images by transmitting a radio wave towards a target (e.g., planetary surface) and measuring the backscattered echoes (Moreira et al., 2013; Neish & Carter, 2014). Radar is an active sensor, providing users with more control over the recorded data. The radar transmitters and receivers can be collocated (monostatic) or separated (bistatic) in space (Neish & Carter, 2014).

One of the benefits of radar is that radio waves can penetrate atmospheres that are opaque to visible wavelengths (Elachi, 1987), making radar a useful tool for studying planets with thick atmospheres, such as those of Earth, Venus, and Titan. Additionally, radar is primarily sensitive to the physical and electrical properties of the surface and near subsurface (depth from centimeters to meters). This sensitivity helps highlight differences in slope, composition, and roughness of a surface, which is relevant for studying impact craters. This is in contrast to visual-infrared imagery, which is primarily sensitive to varying chemical compositions in the upper micron of the surface (Neish & Carter, 2014).

The main categories of radar systems include imagers (which produce 2D images of the surface), sounders (which probe the subsurface structure), and altimeters (which measure the height of the surface).

Synthetic Aperture Radar (SAR) is a type of radar imager that generates high-resolution data using a synthetic aperture, as the name suggests. In radar data, spatial resolution is related to the ratio of the sensor wavelength and length of the sensor's antenna. Consequently, a longer antenna, for a given wavelength, offers higher resolution.

Achieving fine resolution would necessitate an antenna hundreds to thousands of meters long, making it impractical for airborne or spaceborne radar platforms. In SAR, a series of acquisitions from a shorter antenna are combined to simulate a much larger antenna. SAR is a useful technique for studying surface roughness (**Figure 1.10**). It is most sensitive to surface roughness at the scale of radar sensor wavelength, typically ranging from centimeters to decimeters. Rougher surfaces produce more backscatter resulting in a brighter image while smoother surfaces produce backscatter in the opposite direction resulting in a darker image. Backscatter is also affected by other surface properties such as the dielectric constant of the surface and large-scale topography.

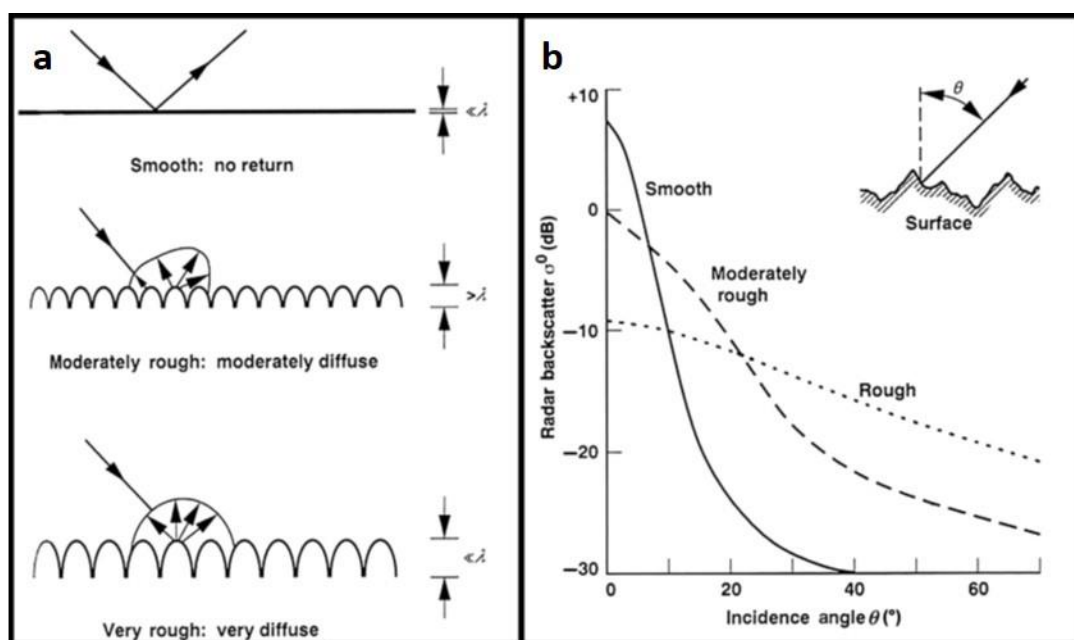


**Figure 1.10: Radar backscatter as a function of surface roughness and incidence angle. (a) Smoother surfaces function as reflectors, diverting the radar signal away from the receiver and resulting in low backscatter. Rougher terrains scatter the signal in multiple directions, including back towards the sensor, thereby amplifying the recorded backscatter. In addition to surface roughness, the backscatter is dependent on incidence angle (b); all surface types tend to exhibit increased reflection at lower incident angles due to quasi-specular scattering. Figure modified from Farr (1993).**



An important consideration is that radar return is sensitive to the composition and dielectric properties of the surface, a factor crucial for comparing radar images of Earth and Titan. Titan's materials demonstrate transparency at centimeter wavelengths and low temperatures, allowing for penetration depths of at least meters (Paillou et al., 2008). The significance of volume scattering in water ice on Titan sets it apart from most Earth materials, such as silicates or basalts, where this phenomenon is irrelevant. This disparity can have a noticeable effect in radar images. For example, at Selk crater on Titan, the effect of volume scattering is pronounced, resulting in a distinctly radar-bright appearance in images (Bonney et al., 2022).

In this dissertation, we use data from several different radar sensors. The Cassini RADAR instrument included a SAR imager, radiometer, and altimeter, all operating at a wavelength of 2.17 cm (Ku-band) and thus sensitive to surface properties at centimeter scales. The highest resolution SAR images of the surface were acquired at 175 meters per pixel, equivalent to a spatial resolution of 350 m (Elachi et al., 2004; Lopes et al., 2010). The radiometer measured brightness temperatures providing information about surface and near-subsurface properties, including dielectric constant and the amount of volume scattering. Lastly, the altimeter measured the topography of Titan's landforms (e.g. Mastrogiuseppe et al., 2014). In addition to altimetry, a new technique called SARTopo was developed using swatches of SAR imagery to increase the coverage of topographic data on Titan. It uses the backscatter differences between each SAR swatch, made with 5 antenna beams, to calculate surface height (Stiles et al., 2009).

Several terrestrial radar datasets are available, and the specific ones used in this thesis are outlined in **Chapter 2**. We note that, in addition to radar remote sensing, there are many techniques with which terrestrial craters have been characterized; these techniques are not currently available for Titan. Geophysical exploration stands out as a significant tool, particularly for studying buried craters that may not be visible through satellite imagery (Pilkington and Grieve, 1992). Gravity and magnetic surveys have proven successful in identifying craters (McBride, 2019; Bianchi et al., 1984). Additionally, seismic surveys have provided valuable insights into the subsurface structure of craters (McBride, 2019).

## 1.4 Numerical Modelling

In addition to remote sensing methods, numerical modelling is another approach to studying the impact cratering process. This is commonly done with the use of hydrocodes, as they are well suited for highly dynamic shock events such as a hypervelocity impact (Anderson, 1987). Hydrocodes are computational tools used to model behaviour of continuous media in order to predict the media's response to deformation. There are three main components to a hydrocode: 1) Newton's laws of motion, 2) equation of state, and 3) the constitutive model (Collins, 2002).

A hydrocode provides solutions to the differential equations (below) that describe the conservation laws for flow of continuous media:

$$\text{Conservation of momentum: } \frac{Du_i}{Dt} = f_i + \frac{1}{\rho} \frac{\partial \sigma_{ji}}{\partial x_i} \quad \text{(Equation 1)}$$

$$\text{Conservation of mass: } \frac{D\rho}{Dt} + \rho \frac{\partial u_i}{\partial x_i} = 0 \quad \text{(Equation 2)}$$

$$\text{Conservation of energy: } \frac{DI}{Dt} = \frac{1}{\rho} \Pi_{ij} \dot{\epsilon}'_{ij} - \frac{p}{\rho} \frac{\partial u_i}{\partial x_i} \quad \text{(Equation 3)}$$

where  $u_i$  is the velocity,  $\rho$  is the material density,  $f_i$  is the external body forces per unit mass,  $I$  is the specific internal energy,  $\sigma_{ji}$  is the stress tensor composed of a hydrostatic component, the pressure  $p$ , and a deviatoric part, the deviatoric stress tensor  $\Pi_{ij}$ , and  $\dot{\epsilon}'_{ij}$  is the deviatoric strain rate.

The second component of a hydrocode is the equation of state which relates pressure ( $p$ ) to the density ( $\rho$ ) and the internal energy ( $I$ ) as follows:

$$\text{Equation of state: } p = p(\rho, I) \quad \text{(Equation 4)}$$

This equation accounts for the irreversible thermodynamic changes (such as heating due to a high shock event) and compressibility changes (such as changes in density).

Lastly, the constitutive model describes the deformation effects (such as changes in shape or strength properties). It relates the stress ( $\sigma_{ji}$ ) to the strain ( $\epsilon_{ij}$ ), strain rate ( $\dot{\epsilon}_{ij}$ ), internal energy ( $I$ ), and damage ( $D$ ):

$$\text{Constitutive model: } \sigma_{ji} = g(\epsilon_{ij}, \dot{\epsilon}_{ij}, I, D) \quad \text{(Equation 5)}$$

Numerical modelling of impacts presented in this thesis was conducted using the iSALE (impact Simplified Arbitrary Lagrangian Eulerian) shock physics code (Wünnemann et al., 2006), an extension of the SALE hydrocode (Amsden et al., 1980). To simulate hypervelocity impacts into solid materials, modifications were made to SALE, incorporating an elasto-plastic constitutive model, fragmentation models, various equations of state (EoS), and the ability to model multiple materials (Melosh et al., 1992; Ivanov et al., 1997). Recent iterations also include the integration of a modified strength model (Collins et al., 2004), a porosity compaction model (Wünnemann et al., 2006; Collins et al., 2011), and a dilatancy model (Collins, 2014).

The continuous media being modelled are divided into a number of separate elements, discretized in space and time, to account for the finite memory on a computer. In order to solve the conservation equations (**Equations 1-3**), a two-dimensional axisymmetric grid, formed by connecting quadrilateral-shaped cells, is setup. The vertices of the cells are defined by Cartesian or cylindrical coordinates. Due to its axisymmetric nature, the simulations are limited to only vertical impacts. However, there is a three-dimensional version, iSALE-3D (Elbeshausen et al., 2009), based upon SALE3D (Amsden & Ruppel, 1981) which has the capability to model the more common oblique impacts (Gilbert, 1893; Shoemaker, 1962). In this thesis, we only employ the two-dimensional version of iSALE.

The behaviour of the grid depends on the reference frame formulation that describes the flow of material within the grid: a) Lagrangian or b) Eulerian. Figure **1.11** illustrates the two different formulations in the form of a dinosaur jumping off a diving board. In the Lagrangian (or material) method, the cells move and deform throughout the duration of the simulation, while the material remains fixed within each cell. In contrast, the grid remains

fixed, while the material (mass, momentum, and energy) moves through cell boundaries in the Eulerian (or spatial) method. iSALE can employ the Lagrangian or Eulerian or a combination of the two descriptions. The hybrid approach, ALE (arbitrary Lagrangian Eulerian), first uses the Lagrangian method to compute forces and stresses, restructures the grid, and updates material velocities in the simulation. Then, the Eulerian method is employed to remap the deformed cell vertices back to the original grid.

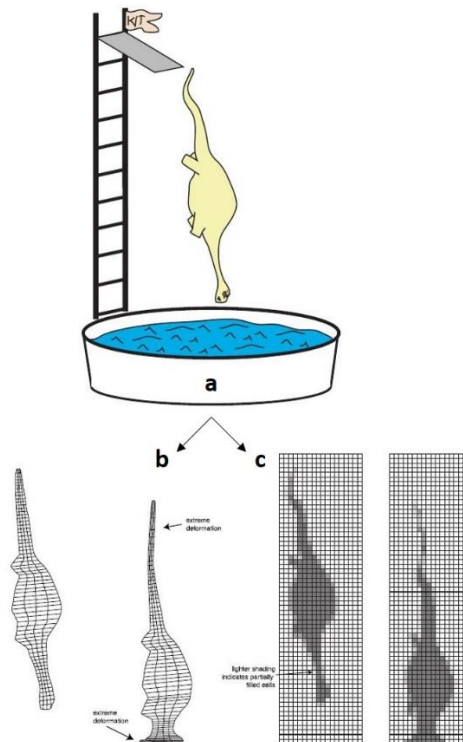


**Figure 1.11: Illustration of a dinosaur jumping of a diving board (a) showing the differences between (b) Lagrangian and (c) Eulerian material descriptions. In (b) the Lagrangian formulation, material is fixed to a cell and the cell deforms under external forces. While in (c) the Eulerian setup, the material flows between the cells while the mesh remains fixed. Figure adapted from Collins (2002).**

The size of mesh needs to be large enough to contain the event being modelled (i.e. propagation of the impact shockwave and crater formation). The mesh is set up to have a high resolution zone and an extension zone (**Figure 1.12**). The high resolution zone is vertically large enough to contain the impactor and the target layers of interest, and extends at least two crater radii horizontally. The cell size in the high resolution zone remains constant, whereas the cell size is varied to decrease the number of total cells.

The boundary conditions of the mesh (**Figure 1.12**) used in this thesis are set to free slip on the left and right, meaning the normal wall velocities are zero through the simulation. The bottom boundary condition is set to no slip, where both velocity components are zero. The top boundary is set to outflow, where the velocities (and densities, energies, etc.) are defined externally and equal to the adjacent cell within the mesh.

The resolution is represented through size of the individual cells in a grid. It is defined in iSALE as computations cells per projectile radius (CPPR):

$$CPPR = \frac{d_{imp}}{2 \times GRDSPC} \quad \text{(Equation 6)}$$

where  $d_{imp}$  is the diameter of the impactor and  $GRDSPC$  is the grid spacing or the cell size.

Smaller cells or a finer grid increase the total number of cells within the grid and result in a higher resolution simulation. The higher the resolution, the more defined the shockwave front and material boundaries will be, which is important for impact modelling. However, the resolution needs to be balanced with computational space and time. For the simulations in this thesis, a CPPR of 10 to 20 sufficient to resolve crater diameters and depth within 10% error (Silber and Johnson, 2017 and references therein). Higher resolution studies are required when tracking peak pressures and temperatures to simulate impact melt formation and evolution.

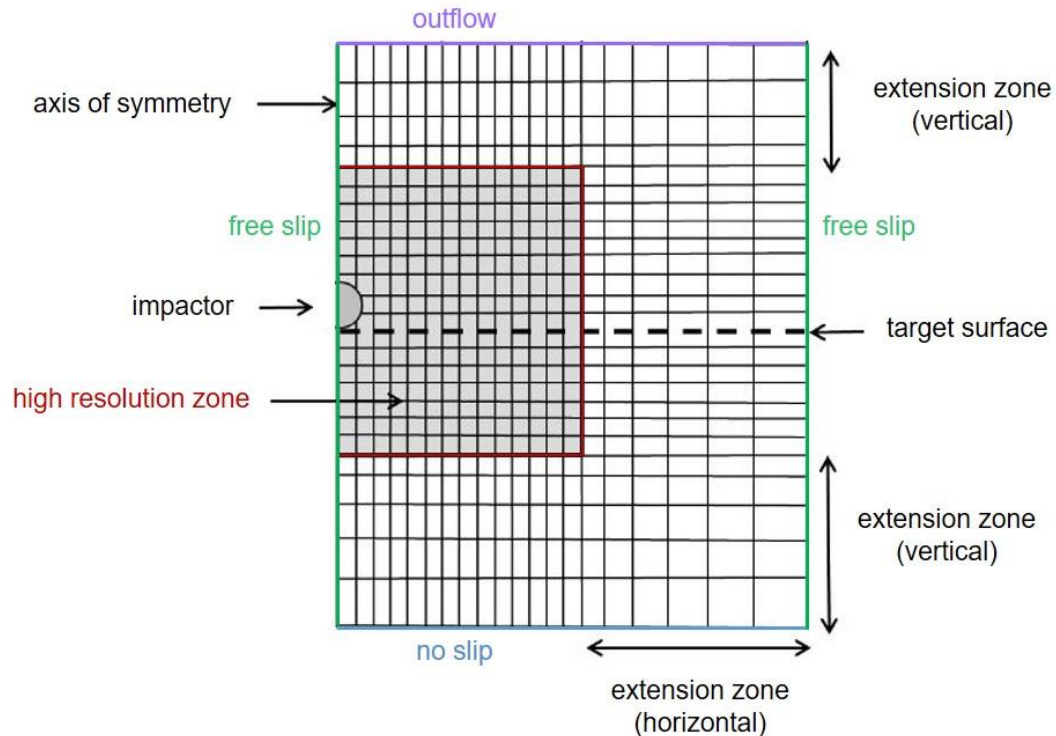


**Figure 1.12:** The mesh grid setup in iSALE is divided into a high resolution zone (shown in red) and an extension zone. The high resolution zone is large enough to cover an area in which the crater will form and has a constant cell size. In the extension zone, the cell size increases in a geometric fashion and thus decreases the total number of cells which helps to decrease computation time. The left boundary of the grid represents the axis of symmetry. In this thesis, the left and right boundary conditions are set to free slip (green), top to outflow (purple), and the bottom is no slip (blue). Figure adapted from Potter (2012).

To run the simulations in iSALE, two input files are required. The first, the asteroid input file, contains details for the mesh geometry including the cell size, spatial resolution, impactor size, as well as the extent of the high-resolution and extension zones (**Figure 1.12**). It also defines the simulation duration, the output variables of interest, and structure of the target. The corresponding input file contains information about materials – only water-ice and water in this work. Samples of the asteroid and material input files used for the Titan impact simulations in this study are included in **Appendix A and B**. The iSALE-Dellen manual (Collins et al., 2016) outlines the model and parameters in detail.

## 1.5 Summary

This thesis consists of three main chapters, in addition to Introduction (Chapter 1) and Discussion (Chapter 5) chapters. **Chapter 1** covers key topics and background information to provide context for the following chapters.

**Chapter 2** is based on a paper submitted to and under review in *Icarus*, “An Analogue Study of Impact Craters on Titan: Implications for Titan’s Surface Age” (Shah et al., 2023). In this work, we characterize the visibility of terrestrial craters in radar images as an analogue for constraining the crater population on Titan.

**Chapter 3** is based on a paper to be submitted to the *Planetary Science Journal*, titled “The Effect of the Crustal Thermal Gradient on Fresh Crater Morphometries on Titan.” In this work, we explore the influence of the thermal gradient of the ice crust on initial crater depths on Titan, and its implications for erosion.

**Chapter 4** is based on a paper to be submitted to the *Planetary Science Journal*, titled “Lessons Learned from the Rover-Aerial Vehicle Exploration Network (RAVEN) Mission Simulation: Applications for Future Operational Procedures for Unoccupied Aircraft Systems (UAS) Missions.” This work presents lessons learned from a UAS-style mission simulation conducted in a Mars analogue terrain and its potential applications for the Dragonfly mission.

**Chapter 5** discusses the overall results of Chapters 2-4 and their implications for our understanding of the impact cratering process on Titan. It also covers the general implications of the work in this thesis.

## 1.6 References

- Ahrens TJ, O'Keefe JD (1972) Shock melting and vaporization of Lunar rocks and minerals. *Moon* 4:214–249.
- Amsden AA, Ruppel HM (1981) SALE-3D: a simplified ALE computer program for calculating three-dimensional fluid flow. United States.
- Amsden AA, Ruppel HM, Hirt CW (1980) SALE: A Simplified ALE computer program for fluid flow at all speeds. Los Alamos National Lab Report LA-8095 101. <https://doi.org/10.2172/5176006>
- Anderson CE (1987) An overview of the theory of hydrocodes. *Intl J of Impact Eng*, 5:33–59.
- Artemieva N, Lunine J (2003) Cratering on Titan: impact melt, ejecta, and the fate of surface organics. *Icarus* 164:471–480. [https://doi.org/10.1016/S0019-1035\(03\)00148-9](https://doi.org/10.1016/S0019-1035(03)00148-9)
- Atkinson KR, Zarnecki JC, Towner MC, et al (2010) Penetrometry of granular and moist planetary surface materials: Application to the Huygens landing site on Titan. *Icarus* 210:843–851. <https://doi.org/10.1016/j.icarus.2010.07.019>
- Balaram J, Aung MM, Golombek MP (2021) The Ingenuity Helicopter on the Perseverance Rover. *Space Sci Rev* 217:1–11. <https://doi.org/10.1007/s11214-021-00815-w>
- Barlow NG (2010) What we know about Mars from its impact craters. *Bull Geol Soc Am* 122:644–657. <https://doi.org/10.1130/B30182.1>
- Barnes JW, Brown RH, Soderblom L, et al (2008) Spectroscopy, morphometry, and photoclinometry of Titan's dunefields from Cassini/VIMS. *Icarus* 195:400–414. <https://doi.org/10.1016/j.icarus.2007.12.006>



Barnes JW, Radebaugh J, Brown RH, et al (2007) Near-infrared spectral mapping of Titan's mountains and channels. *J Geophys Res Planets* 112:1–13.

<https://doi.org/10.1029/2007JE002932>

Barnes JW, Lemke L, Foch R et al (2012) AVIATR—Aerial Vehicle for In-situ and Airborne Titan Reconnaissance. *Exp Astron* 33:55–127.

<https://doi.org/10.1007/s10686-011-9275-9>

Barnes JW, Lorenz RD, Radebaugh J, et al (2015) Production and global transport of Titan's sand particles. *Planet Sci* 4:1–19.

<https://doi.org/10.1186/s13535-015-0004-y>

Barnes JW, Turtle EP, Trainer MG, et al (2021) Science Goals and Objectives for the Dragonfly Titan Rotorcraft Relocatable Lander. *Planet Sci J* 2:130.

<https://doi.org/10.3847/PSJ/abfdcf>

Bézar B (2014) The methane mole fraction in Titan's stratosphere from DISR measurements during the Huygens probe's descent. *Icarus* 242:64–73

<https://doi.org/10.1016/j.icarus.2014.07.013>

Bianchi R, Capaccioni F, Cerroni P, et al (1984) Radiofrequency emissions observed during macroscopic hypervelocity impact experiments. *Nature* 308:830–832.

<https://doi.org/10.1038/308830a0>

Birch SPD, Hayes AG, Corlies P, et al (2018) Morphological evidence that Titan's southern hemisphere basins are paleoseas. *Icarus* 310:140–148.

<https://doi.org/10.1016/J.ICARUS.2017.12.016>

Birch SPD, Hayes AG, Dietrich WE, et al (2017) Geomorphologic mapping of Titan's polar terrains: Constraining surface processes and landscape evolution. *Icarus* 282:214–236.

<https://doi.org/10.1016/J.ICARUS.2016.08.003>

Bland MT, Singer KN, McKinnon WB, Schenk PM (2017) Viscous relaxation of Ganymede's impact craters: Constraints on heat flux. *Icarus* 296:275–288.

<https://doi.org/10.1016/J.ICARUS.2017.06.012>

- Bonnefoy LE, Hayes AG, Hayne PO, et al (2016) Compositional and spatial variations in Titan dune and interdune regions from Cassini VIMS and RADAR. *Icarus* 270:222–237. <https://doi.org/10.1016/J.ICARUS.2015.09.014>
- Bonnefoy LE, Lucas A, Hayes AG, et al (2022) Composition, Roughness, and Topography from Radar Backscatter at Selk Crater, the Dragonfly Landing Site. *Planet Sci J* 3:201. <https://doi.org/10.3847/PSJ/ac8428>
- Brown RH, Baines KH, Bellucci G, et al (2005) The Cassini visual and infrared mapping spectrometer (VIMS) investigation. *Space Sci Rev* 115:111–168. <https://doi.org/10.1007/s11214-004-1453-x>
- Burr DM, Jacobsen RE, Roth DL, et al (2009) Fluvial network analysis on Titan: Evidence for subsurface structures and west-to-east wind flow, southwestern Xanadu. *Geophys Res Lett* 36:1–5. <https://doi.org/10.1029/2009GL040909>
- Burr DM, Taylor Perron J, Lamb MP, et al (2013) Fluvial features on Titan: Insights from morphology and modeling. *Bull Geol Soc Am* 125:299–321. <https://doi.org/10.1130/B30612.1>
- Carr MH, Crumpler LS, Cutts JA, et al (1977) Martian impact craters and emplacement of ejecta by surface flow. *J Geophys Res* 82:4055–4065. <https://doi.org/10.1029/JS082i028p04055>
- Choukroun M, Grasset O, Tobie G, Sotin C (2010) Stability of methane clathrate hydrates under pressure: Influence on outgassing processes of methane on Titan. *Icarus* 205:581–593. <https://doi.org/10.1016/J.ICARUS.2009.08.011>
- Choukroun M, Sotin C (2012) Is Titan's shape caused by its meteorology and carbon cycle? *Geophys Res Lett* 39:1–5. <https://doi.org/10.1029/2011GL050747>
- Collins GS, 2002. An Introduction to Hydrocode Modeling. Applied Modelling and Computation Group, Imperial College London, unpublished.

- Collins GC (2005) Relative rates of fluvial bedrock incision on Titan and Earth. *Geophys Res Lett* 32:1–4. <https://doi.org/10.1029/2005GL024551>
- Collins GS (2014) Numerical simulations of impact crater formation with dilatancy. *J Geophys Res Planets* 119:2600–2619. <https://doi.org/10.1002/2014JE004708>
- Collins GS, Elbenschauen D, Wunnemann K, et al (2016) iSALE: A multi-material, multi-rheology shock physics code for simulating impact phenomena in two and three dimensions. iSALE-Dellen release.
- Collins GS, Johnson TV (2014) Ganymede and Callisto. In: *Encyclopedia of the Solar System*. Elsevier, pp. 813–829
- Collins GS, Melosh HJ, Ivanov BA (2004) Modeling damage and deformation in impact simulations. *Meteorit Planet Sci* 39:217–231. <https://doi.org/10.1111/j.1945-5100.2004.tb00337.x>
- Collins GS, Melosh HJ, Wunnemann K (2011) Improvements to the  $\epsilon$ - $\alpha$  porous compaction model for simulating impacts into high-porosity solar system objects. *Int J Impact Eng* 38:434–439. <https://doi.org/https://doi.org/10.1016/j.ijimpeng.2010.10.013>
- Collins GS, Wu K (2005) How big was the Chesapeake Bay impact? Insight from numerical modeling. *Geology* 33:925–928. <https://doi.org/10.1130/G21854.1>
- Comas Solá J (1908) Observations des satellites principaux de Jupiter et de Titan. *Astron Nachr* 179:289–290.
- Coustonis A (2014) Titan. In: *Encyclopedia of the Solar System*. Elsevier, pp. 883–905
- Coustonis A, Hirtzig M (2009) Cassini – Huygens results on Titan’s surface. *Res Astron Astrophys* 9:249–268. <https://doi.org/10.1088/1674-4527/9/3/001>
- Danielson RE, Caldwell JJ, Larach DR (1973) An inversion in the atmosphere of Titan, *Icarus* 20:437–443. [https://doi.org/10.1016/0019-1035\(73\)90016-X](https://doi.org/10.1016/0019-1035(73)90016-X)

- Dence MR (1965) The extraterrestrial origin of Canadian craters. *Annals of the New York Academy of Sciences* 123:941–969.
- Dombard AJ, McKinnon WB (2000) Long-term retention of impact crater topography on Ganymede. *Geophys Res Lett* 27:3663–3666.  
<https://doi.org/https://doi.org/10.1029/2000GL011695>
- Dombard AJ, McKinnon WB (2006) Elastoviscoplastic relaxation of impact crater topography with application to Ganymede and Callisto. *J Geophys Res Planets* 111:1–22. <https://doi.org/10.1029/2005JE002445>
- Durham, WB, Prieto-Ballesteros O, Goldsby DL et al (2010) Rheological and Thermal Properties of Icy Materials. *Space Sci Rev* 153:273–298.  
<https://doi.org/10.1007/s11214-009-9619-1>
- Elachi C (1987) *Spaceborne radar remote sensing: Applications and techniques*. New York: IEEE Press
- Elachi C, Allison MD, Borgarelli L, et al (2004) Radar: The Cassini Titan Radar Mapper. In: *The Cassini-Huygens Mission*. Springer, pp. 71–110.  
[https://doi.org/10.1007/1-4020-3874-7\\_2](https://doi.org/10.1007/1-4020-3874-7_2)
- Elachi C, Wall S, Allison M, et al (2005) Cassini radar views the surface of Titan. *Science* 308:970–974. <https://doi.org/10.1126/science.1109919>
- Elbeshhausen D, Wünnemann K, Collins GS (2009) Scaling of oblique impacts in frictional targets: Implications for crater size and formation mechanisms. *Icarus* 204:716–731. <https://doi.org/10.1016/J.ICARUS.2009.07.018>
- Elder CM, Bray VJ, Melosh HJ (2012) The theoretical plausibility of central pit crater formation via melt drainage. *Icarus* 221:831–843.  
<https://doi.org/10.1016/J.ICARUS.2012.09.014>
- European Space Agency (1988) *Cassini Saturn Orbiter and Titan Probe. Report on the Phase A Study*

- Farr (1993) Radar interactions with geologic surfaces. In: Guide to Magellan image interpretation. JPL, pp 45–56
- Flasar F, Achterberg R, Conrath B, et al (2005) Titan's Atmospheric Temperatures, Winds, and Composition. *Science* 308:975–978.  
<https://doi.org/10.1126/science.1111150>
- Flasar FM, Achterberg RK, Schinder PJ (2014) Thermal Structure of Titan's Troposphere and Middle Atmosphere. Cambridge Univ. Press, pp. 102–121
- Gault DE, Quaide WL, Oberbeck VR (1968) Impact cratering mechanics and structures. In: Shock Metamorphism of Natural Materials. Mono Book Corp, pp 87–99
- Gilbert GK (1893) The moon's face: A study of the origin of its features. *Science* 21:305–307. <https://doi.org/10.1126/science.ns-21.539.305-c>
- Gillett FC (1975) Further observations of the 8–13 micron spectrum of Titan. *Astrophys J* 201:L41–L43. <https://doi.org/10.1086/181937>
- Gillett FC, Forrest WJ, Merrill KM (1973) 8–13 micron observations of Titan. *Astrophys J* 184: L93–L95. <https://doi.org/10.1086/181296>
- Grant JA (1999) Evaluating the evolution of process specific degradation signatures around impact craters. *Int J Impact Eng* 23:331–340.  
[https://doi.org/10.1016/S0734-743X\(99\)00084-6](https://doi.org/10.1016/S0734-743X(99)00084-6)
- Grant JA, Schultz PH (1993) Degradation of selected terrestrial and Martian impact craters. *J Geophys Res Planets* 98:11025–11042.  
<https://doi.org/10.1029/93JE00121>
- Grieve RAF (1987) Terrestrial Impact Structures. *Annu Rev Earth Planet Sci* 15:245–270. <https://doi.org/10.1146/annurev.ea.15.050187.001333>

- Grieve RAF, Dence MR, Robertson PB (1977) Cratering processes: as interpreted from the occurrences of impact melts. In: Impact and Explosion Cratering. Pergamon Press, pp 791–814
- Grieve RAF, Osinski GR, Tornabene LL (2014) Planetary Impacts. In: Encyclopedia of the Solar System. Elsevier, pp. 83–99
- Gupta S, Ochiai E, Ponnampereuma C (1981) Organic synthesis in the atmosphere of Titan. *Nature* 293:725–727
- Gwizd S, Stack KM, Calef F, et al (2023) Rover-Aerial Vehicle Exploration Network (RAVEN): Mission Planning, Implementation, and Results from the 2022 Rover-Only Field Campaign at Holuhraun, Iceland. In: LPI Contributions. p 1748
- Hamilton CW. (2015) Team gets firsthand look at the new Holuhraun eruption site. *Eos* 96. <https://doi.org/10.1029/2015EO041197>
- Hamilton CW, Voigt JRC, Zanetti M, et al (2023) The Holuhraun Region of Iceland as a High-Fidelity Planetary Analog Site for Science and Exploration. In: LPI Contributions. p 3010
- Hand KP, Sotin C, Hayes A, Coustenis A (2020) On the Habitability and Future Exploration of Ocean Worlds. *Space Sci Rev* 216:95. <https://doi.org/10.1007/s11214-020-00713-7>
- Hanel R, Conrath B, Flasar FM, et al (1981) Infrared observations of the Saturnian system from Voyager 1. *Science* 212:192–200. <https://doi.org/10.1126/science.212.4491.192>
- Hayes AG (2016) The Lakes and Seas of Titan. *Annu Rev Earth Planet Sci* 44:57–83. <https://doi.org/10.1146/annurev-earth-060115-012247>
- Hayes AG, Lorenz RD, Lunine JI (2018) A post-Cassini view of Titan’s methane-based hydrologic cycle. *Nat Geosci* 11:306–313. <https://doi.org/10.1038/s41561-018-0103-y>

- Hedgepeth JE, Neish CD, Turtle EP, et al (2020) Titan's impact crater population after Cassini. *Icarus* 344:113664. <https://doi.org/10.1016/j.icarus.2020.113664>
- Hendrix AR, Hurford TA, Barge LM, et al (2018) The NASA Roadmap to Ocean Worlds. *Astrobiology* 19:1–27. <https://doi.org/10.1089/ast.2018.1955>
- Hörst SM (2017) Titan's atmosphere and climate. *J Geophys Res Planets* 122:432–482. <https://doi.org/10.1002/2016JE005240>
- Ivanov BA, Deniem D, Neukum G (1997) Implementation of dynamic strength models into 2D hydrocodes: Applications for atmospheric breakup and impact cratering. *Int J Impact Eng* 20:411–430. [https://doi.org/10.1016/S0734-743X\(97\)87511-2](https://doi.org/10.1016/S0734-743X(97)87511-2)
- Janssen MA, Le Gall A, Lopes RM, et al (2016) Titan's surface at 2.18-cm wavelength imaged by the Cassini RADAR radiometer: Results and interpretations through the first ten years of observation. *Icarus* 270:443–459. <https://doi.org/10.1016/J.ICARUS.2015.09.027>
- Karkoschka E, Schröder SE (2016) The DISR imaging mosaic of Titan's surface and its dependence on emission angle. *Icarus* 270:307–325. <https://doi.org/10.1016/J.ICARUS.2015.08.006>
- Kalousová K, Sotin C (2020) The Insulating Effect of Methane Clathrate Crust on Titan's Thermal Evolution. *Geophys Res Lett* 47. <https://doi.org/10.1029/2020GL087481>
- Keller HU, Grieger B, Küppers M, et al (2008) The properties of Titan's surface at the Huygens landing site from DISR observations. *Planet Space Sci* 56:728–752. <https://doi.org/10.1016/J.PSS.2007.11.020>
- Kenkmann T (2021) The terrestrial impact crater record: A statistical analysis of morphologies, structures, ages, lithologies, and more. *Meteorit Planet Sci* 56:1024–1070. <https://doi.org/https://doi.org/10.1111/maps.13657>

- Kenkmann T, Collins GS, Wünnemann K (2012) The modification stage of impact cratering. In: *Impact Cratering: Processes and Products*. Wiley-Blackwell, pp 60–75. <https://doi.org/10.1002/9781118447307.ch5>
- Krasnopolsky VA (2014). Chemical composition of Titan's atmosphere and ionosphere: Observations and the photochemical model. *Icarus* 236:83–91. <https://doi.org/10.1016/J.ICARUS.2014.03.041>
- Korycansky DG, Zahnle KJ (2005) Modeling crater populations on Venus and Titan. *Planet Space Sci* 53:695–710. <https://doi.org/10.1016/J.PSS.2005.03.002>
- Kuiper GP (1944) Titan: A satellite with an atmosphere. *Astrophys J* 100:378. <https://doi.org/10.1086/144679>
- Kunde VG, Aikin AC, Hanel RA, et al (1981) C<sub>4</sub>H<sub>2</sub>, HC<sub>3</sub>N and C<sub>2</sub>N<sub>2</sub> in Titan's atmosphere. *Nature* 292:686–688. <https://doi.org/10.1038/292686a0>
- Lebreton J-P, Matson DL (2003) The Huygens Probe: Science, Payload and Mission Overview. In: *The Cassini-Huygens Mission*. Springer Netherlands, pp. 59–100. [https://doi.org/10.1007/978-94-017-3251-2\\_2](https://doi.org/10.1007/978-94-017-3251-2_2)
- Lebreton J-P, Witasse O, Sollazzo C, et al (2005) An overview of the descent and landing of the Huygens probe on Titan. *Nature* 438:758–764. <https://doi.org/10.1038/nature04347>
- Le Gall A, Janssen MA, Wye LC, et al (2011) Cassini SAR, radiometry, scatterometry and altimetry observations of Titan's dune fields. *Icarus* 213:608–624. <https://doi.org/10.1016/j.icarus.2011.03.026>
- Levine JS, Wright HS (2005) NASA Technical Report.
- Lindal GF, Wood GE, Hotz HB, et al (1983) The atmosphere of Titan: An analysis of the Voyager 1 radio occultation measurements. *Icarus* 53:348–363. [https://doi.org/10.1016/0019-1035\(83\)90155-0](https://doi.org/10.1016/0019-1035(83)90155-0)



- Lopes RMC, Malaska MJ, Schoenfeld AM, et al (2020) A global geomorphologic map of Saturn's moon Titan. *Nat Astron* 4:228–233.  
<https://doi.org/10.1038/s41550-019-0917-6>
- Lopes RMC, Malaska MJ, Solomonidou A, et al (2016) Nature, distribution, and origin of Titan's Undifferentiated Plains. *Icarus* 270:162–182.  
<https://doi.org/10.1016/J.ICARUS.2015.11.034>
- Lopes RMC, Mitchell KL, Wall SD, et al (2007) The Lakes and Seas of Titan. *Eos* 66:569–576. <https://doi.org/10.1029/2007EO510001>
- Lopes RMC, Stofan ER, Peckyno R, et al (2010) Distribution and interplay of geologic processes on Titan from Cassini radar data. *Icarus* 205:540–558.  
<https://doi.org/10.1016/J.ICARUS.2009.08.010>
- Lorenz RD (2000) Post-Cassini Exploration of Titan: Science Rationale and Mission Concepts. *J British Interplanet Soc* 53:218-234.
- Lorenz RD (2001) Flight Power Scaling of Airplanes, Airships, and Helicopters: Application to Planetary Exploration. *J Aircraft* 38:208-214.
- Lorenz RD (2006) What Titan is really like: In-situ measurements of the Titan environment by the Huygens probe. *IEEE Aerosp Conf Proc* 2006 1-10.  
<https://doi.org/10.1109/aero.2006.1655736>
- Lorenz RD (2008) A Review of Balloon Concepts for Titan. *J British Interplanet Soc* 61:2-13.
- Lorenz RD, MacKenzie SM, Neish CD, et al (2021) Selection and Characteristics of the Dragonfly Landing Site near Selk Crater, Titan. *Planet Sci J* 2:24.  
<https://doi.org/10.3847/PSJ/abd08f>
- Lorenz RD, Mitchell KL, Kirk RL, et al (2008) Titan's inventory of organic surface materials. *Geophys Res Lett* 35:1–6. <https://doi.org/10.1029/2007GL032118>

- Lorenz RD, Lopes RM, Paganelli F, et al (2008) Fluvial channels on Titan: Initial Cassini RADAR observations. *Planet Space Sci* 56:1132–1144.  
<https://doi.org/10.1016/J.PSS.2008.02.009>
- Lorenz RD, Wall S, Radebaugh J, et al (2006) The sand seas of titan: Cassini RADAR observations of longitudinal dunes. *Science* 312:724–727.  
<https://doi.org/10.1126/science.1123257>
- Lorenz RD, Zimbelman JR (2014) Titan Dunes. In: *Dune Worlds*. Springer, pp. 157–167.  
[https://doi.org/10.1007/978-3-540-89725-5\\_13](https://doi.org/10.1007/978-3-540-89725-5_13)
- Lunine JJ, Atreya SK (2008) The methane cycle on Titan. *Nat Geosci* 1:159–164.  
<https://doi.org/10.1038/ngeo125>
- Lunine JJ, Stevenson DJ, Yung YL (1983) Ethane ocean on Titan. *Science* 222:1229–1230. <https://doi.org/10.1126/science.222.4629.1229>
- MacKenzie SM, Birch SPD, Hörst S, et al (2021) Titan: Earth-like on the Outside, Ocean World on the Inside. *Planet Sci J* 2:112. <https://doi.org/10.3847/PSJ/abf7c9>
- Malaska MJ, Lopes RM, Hayes AG, et al (2016) Material transport map of Titan: The fate of dunes. *Icarus* 270:183–196.  
<https://doi.org/10.1016/J.ICARUS.2015.09.029>
- Martino MD, Flamini E, Staffieri S (2019) Origin and Classification of Impacting Objects, and their Effects on the Earth Surface. In: *Encyclopedia Atlas of Terrestrial Impact Craters*. Springer, pp 7–18.  
[https://doi.org/10.1007/978-3-030-05451-9\\_2](https://doi.org/10.1007/978-3-030-05451-9_2)
- Mastrogiuseppe M, Poggiali V, Hayes A, et al (2014). The bathymetry of a Titan sea. *Geophys Res Lett* 41:1432–1437. <https://doi.org/10.1002/2013GL058618>
- Matson DL, Spilker LJ, Lebreton J-P (2003) The Cassini/Huygens Mission to the Saturnian System. In: *The Cassini-Huygens Mission*. Springer Netherlands, pp. 1–58. [https://doi.org/10.1007/978-94-017-3251-2\\_1](https://doi.org/10.1007/978-94-017-3251-2_1)

- McBride K (2019) The Planet Earth: A Review of the Influence of Cratering on the Geological Evolution of our Planet. In: Encyclopedia Atlas of Terrestrial Impact Craters. Springer, pp 29–40. [https://doi.org/10.1007/978-3-030-05451-9\\_4](https://doi.org/10.1007/978-3-030-05451-9_4)
- Melosh JH (1989) Impact cratering: A geological process. Oxford University Press
- Melosh J (2012) The contact and compression stage of impact cratering. In: Impact Cratering: Processes and Products. Wiley-Blackwell, pp 32–42  
<https://doi.org/10.1002/9781118447307.ch3>
- Melosh HJ, Ivanov BA (1999) Impact Crater Collapse. *Annu Rev Earth Planet Sci* 27:385–415. <https://doi.org/10.1146/annurev.earth.27.1.385>
- Melosh HJ, Ryan EV, Asphaug E (1992). Dynamic fragmentation in impacts: Hydrocode simulation of laboratory impacts. *J Geophys Res*, 97:14735–14759.  
<https://doi.org/10.1029/92JE01632>
- Mitri G, Showman AP (2008) Thermal convection in ice-I shells of Titan and Enceladus. *Icarus* 193:387–396. <https://doi.org/10.1016/j.icarus.2007.07.016>
- Mitri G, Showman AP, Lunine JJ, Lorenz RD (2007) Hydrocarbon lakes on Titan. *Icarus* 186:385–394. <https://doi.org/10.1016/J.ICARUS.2006.09.004>
- Moreira A, Prats-Iraola P, Younis M, et al (2013) A tutorial on synthetic aperture radar. *IEEE Geosci Remote Sens Mag* 1:6–43.  
<https://doi.org/10.1109/MGRS.2013.2248301>
- Morrison D, Cruikshank DP, Murphy RE (1972), Temperatures of Titan and the Galilean satellites at 20 microns, *Astrophys J* 173: L143–L146  
<https://doi.org/10.1086/180934>
- Neish CD, Carter LM (2014) Planetary Radar. In: Encyclopedia of the Solar System. Elsevier, pp 1133–1159. <https://doi.org/10.1016/B978-0-12-415845-0.00053-0>

- Neish CD, Barnes JW, Sotin C, et al (2015) Spectral properties of Titan's impact craters imply chemical weathering of its surface. *Geophys Res Lett* 42:3746–3754.  
<https://doi.org/10.1002/2015GL063824>
- Neish CD, Kirk RL, Lorenz RD, et al (2013) Crater topography on Titan: Implications for landscape evolution. *Icarus* 223:82–90.  
<https://doi.org/https://doi.org/10.1016/j.icarus.2012.11.030>
- Neish CD, Lorenz RD (2012) Titan's global crater population: A new assessment. *Planet Space Sci* 60:26–33. <https://doi.org/10.1016/j.pss.2011.02.016>
- Neish CD, Lorenz RD (2014) Elevation distribution of Titan's craters suggests extensive wetlands. *Icarus* 228:27-34. <https://doi.org/10.1016/j.icarus.2013.09.024>
- Neish CD, Lorenz RD, Kirk RL, Wye LC (2010) Radarclinometry of the sand seas of Africa's Namibia and Saturn's moon Titan. *Icarus* 208:385–394.  
<https://doi.org/10.1016/j.icarus.2010.01.023>
- Neish CD, Lorenz RD, Turtle EP, et al (2018) Strategies for detecting biological molecules on Titan. *Astrobiology* 18:571-585.  
<https://doi.org/10.1089/ast.2017.1758>
- Neish CD, Molaro JL, Lora JM, et al (2016) Fluvial erosion as a mechanism for crater modification on Titan. *Icarus* 270:114–129.  
<https://doi.org/10.1016/j.icarus.2015.07.022>
- Niemann HB, Atreya SK, Bauer SJ, et al (2005) The abundances of constituents of Titan's atmosphere from the GCMS instrument on the Huygens probe. *Nature* 438:779–784. <https://doi.org/10.1038/nature04122>
- Nimmo F, Bills BG (2010) Shell thickness variations and the long-wavelength topography of Titan. *Icarus* 208:896–904.  
<https://doi.org/10.1016/j.icarus.2010.02.020>

- Nimmo F, Pappalardo RT (2016) Ocean worlds in the outer solar system. *JGR Planets* 8:1378–1399. <https://doi.org/10.1002/2016JE005081>
- Osinski GR, Grieve RAF (2019) Impact Earth: A New Resource for Outreach, Teaching, and Research. *Elements* 15:70–71. <https://doi.org/10.2138/gselements.15.1.70>
- Osinski GR, Grieve RAF, Ferrière L et al (2022) Impact Earth: A review of the terrestrial impact record. *Earth Sci Rev* 232:104112. <https://doi.org/10.1016/J.EARSCIREV.2022.104112>
- Osinski GR, Grieve RAF, Tornabene LL (2012) Excavation and impact ejecta emplacement. In: *Impact Cratering: Processes and Products*. Wiley-Blackwell, pp 43–59. <https://doi.org/10.1002/9781118447307.ch4>
- Osinski GR, Pierazzo E (2012) Impact Cratering: Processes and Products. In: *Impact Cratering: Processes and Products*. Wiley-Blackwell pp 1–20. <https://doi.org/10.1002/9781118447307.ch1>
- Osinski GR, Tornabene LL, Grieve RAF (2011) Impact ejecta emplacement on terrestrial planets. *Earth Planet Sci Lett* 310:167–181. <https://doi.org/10.1016/j.epsl.2011.08.012>
- Paillou P, Lunine J, Ruffié G, et al (2008) Microwave dielectric constant of Titan-relevant materials. *Geophys Res Lett* 35:8–11. <https://doi.org/10.1029/2008GL035216>
- Passey QR, Shoemaker EM (1982) Craters and basins on Ganymede and Callisto - Morphological indicators of crustal evolution. In: *Satellites of Jupiter*, pp 379–434
- Pike RJ (1980) Formation of complex impact craters: Evidence from Mars and other planets. *Icarus* 43:1-19. [https://doi.org/10.1016/0019-1035\(80\)90083-4](https://doi.org/10.1016/0019-1035(80)90083-4)
- Pilkington M, Grieve RAF (1992) The geophysical signature of terrestrial impact craters. *Rev Geophys* 30:161–181. <https://doi.org/10.1029/92RG00192>

- Poggiali V, Mastrogiuseppe M, Hayes AG, et al (2016). Liquid-filled canyons on Titan. *Geophys Res Lett* 43:7887–7894. <https://doi.org/10.1002/2016GL069679>
- Porco CC, West RA, Squyres S, et al (2004) Cassini Imaging Science: Instrument Characteristics and Anticipated Scientific Investigations at Saturn. In: *The Cassini-Huygens Mission*. Springer pp 363–497. [https://doi.org/10.1007/1-4020-3874-7\\_6](https://doi.org/10.1007/1-4020-3874-7_6)
- Potter R (2012). Numerical modelling of basin-scale impact crater formation. Thesis. Imperial College London.
- Raulin F (2008) Astrobiology and Habitability of Titan. In: *Strategies of Life Detection*. Springer, pp 37–48 [https://doi.org/10.1007/978-0-387-77516-6\\_5](https://doi.org/10.1007/978-0-387-77516-6_5)
- Sagan C, Khare BN (1979) Tholins: organic chemistry of interstellar grains and gas. *Nature* 277:102–107.
- Sagan C, Thompson WR (1984) Production and condensation of organic gases in the atmosphere of Titan. *Icarus* 59:133–161. [https://doi.org/10.1016/0019-1035\(84\)90018-6](https://doi.org/10.1016/0019-1035(84)90018-6)
- Schenk PM (1991) Ganymede and Callisto: Complex crater formation and planetary crusts. *J Geophys Res* 96:15635–15664. <https://doi.org/10.1029/91JE00932>
- Schenk PM (2002) Thickness constraints on the icy shells of the galilean satellites from a comparison of crater shapes. *Nature* 417:419–421. <https://doi.org/10.1038/417419a>
- Schenk PM, Chapman CR, Zahnle K, Moore JM (2004) Ages and interiors: the cratering record of the Galilean satellites. In: *Jupiter. The Planet, Satellites and Magnetosphere*. Cambridge Univ Press, pp 427–456
- Schurmeier LR, Dombard AJ (2018) Crater relaxation on Titan aided by low thermal conductivity sand infill. *Icarus* 305:314–323. <https://doi.org/10.1016/J.ICARUS.2017.10.034>

- Silber EA, Johnson BC (2017) Impact crater morphology and the structure of Europa's ice shell. *J Geophys Res Planet* 122:2685–2701.  
<https://doi.org/10.1002/2017JE005456>
- Senft LE, Stewart ST (2009) Dynamic fault weakening and the formation of large impact craters. *Earth Planet Sci Lett* 287:471–482.  
<https://doi.org/10.1016/j.epsl.2009.08.033>
- Shah J, Carr BB, Hadland N, et al (2023) Evaluating the Use of Unoccupied Aircraft Systems (UAS) for Planetary Surface Exploration in Analog Terrain. In: *LPI Contributions*. p 1732
- Shoemaker EM (1962) Interpretation of lunar craters. In: *Physics and astronomy of the moon*. New York: Academic Press, pp. 283–359
- Sloan ED (1998) *Clathrate Hydrates of Natural Gases, Second Edition, Revised and Expanded*. Taylor & Francis
- Soderblom JM, Brown RH, Soderblom LA, et al (2010) Geology of the Selk crater region on Titan from Cassini VIMS observations. *Icarus* 208:905–912.  
<https://doi.org/10.1016/J.ICARUS.2010.03.001>
- Soderblom LA, Kirk RL, Lunine JJ, et al (2007). Correlations between Cassini VIMS spectra and RADAR SAR images: Implications for Titan's surface composition and the character of the Huygens Probe Landing Site. *Planet Space Sci* 55:2025–2036. <https://doi.org/10.1016/j.pss.2007.04.014>
- Solomonidou A, Neish C, Coustenis A, et al (2020) The chemical composition of impact craters on Titan: I. Implications for exogenic processing. *Astron Astrophys* 641.  
<https://doi.org/10.1051/0004-6361/202037866>
- Stiles BW, Hensley S, Gim Y, et al (2009) Determining Titan surface topography from Cassini SAR data. *Icarus* 202:584–598.  
<https://doi.org/10.1016/J.ICARUS.2009.03.032>

- Stofan ER, Elachi C, Lunine JJ, et al (2007) The lakes of Titan. *Nature* 445:61–64.  
<https://doi.org/10.1038/nature05438>
- Tobie G, Lunine JJ, Sotin C (2006) Episodic outgassing as the origin of atmospheric methane on Titan. *Nature* 440:61–64. <https://doi.org/10.1038/nature04497>
- Tomasko M, Archinal B, Becker T et al (2005) Rain, winds and haze during the Huygens probe's descent to Titan's surface. *Nature* 438:765–778.  
<https://doi.org/10.1038/nature04126>
- Trafton L (1972) The bulk composition of Titan's atmosphere. *Astrophys J* 175:295-305.  
<https://doi.org/10.1086/151557>
- Turcotte DL, Schubert G (2014) *Geodynamics, Third Edition*. Cambridge Univ Press
- Turtle EP, Perry JE, Barbara JM, et al (2018) Titan's Meteorology Over the Cassini Mission: Evidence for Extensive Subsurface Methane Reservoirs. *Geophys Res Lett* 45:5320–5328. <https://doi.org/10.1029/2018GL078170>
- Turtle EP, Pierazzo E (2001) Thickness of a European Ice Shell from Impact Crater Simulations. *Science* 294:1326–1328. <https://doi.org/10.1126/science.1062492>
- Turtle EP, Trainer MG, Barnes JW, et al (2020) Dragonfly: In situ exploration of Titan's organic chemistry and habitability. In: *LPI Contributions*. p 2288.
- Voigt JRC, Hamilton CW, Stack KM (2023) The 2014-2015 Holuhraun Lava Flow-Field in Iceland as an Analog Site for Young Volcanic Terrains in Elysium Planitia, Mars. In: *LPI Contributions*. p 1646
- Waite JH (2005) Ion Neutral Mass Spectrometer Results from the First Flyby of Titan. *Science* 308:982–986. <https://doi.org/10.1126/science.1110652>
- Wakita S, Johnson BC, Soderblom JM, et al (2022) Methane-saturated Layers Limit the Observability of Impact Craters on Titan. *Planet Sci J* 3:50.  
<https://doi.org/10.3847/psj/ac4e91>



- Wakita S, Johnson BC, Soderblom JM, et al (2023) Modeling the Formation of Selk Impact Crater on Titan: Implications for Dragonfly. *Planet Sci J* 4:51.  
<https://doi.org/10.3847/PSJ/acbe40>
- Werynski A, Neish CD, Le Gall A, Janssen MA (2019) Compositional variations of Titan's impact craters indicates active surface erosion. *Icarus* 321:508–521.  
<https://doi.org/10.1016/J.ICARUS.2018.12.007>
- Williams KE, McKay CP, Persson F (2012) The surface energy balance at the Huygens landing site and the moist surface conditions on Titan. *Planet Space Sci* 60:376–385. <https://doi.org/10.1016/J.PSS.2011.11.005>
- Wünnemann K, Collins GS, Melosh HJ (2006) A strain-based porosity model for use in hydrocode simulations of impacts and implications for transient crater growth in porous targets. *Icarus* 180:514–527. <https://doi.org/10.1016/j.icarus.2005.10.013>
- Zarnecki JC, Leese MR, Hathi B, et al (2005) A soft solid surface on Titan as revealed by the Huygens Surface Science Package. *Nature* 438:792–795.  
<https://doi.org/10.1038/nature04211>

## Chapter 2

### 2 An Analogue Study of Impact Craters on Titan: Implications for Titan's Surface Age

Titan is the only planetary body in our solar system, besides Earth, that has stable liquids on its surface and a thick, nitrogen-rich atmosphere. NASA's Cassini mission detected an unusually low number of impact craters on Titan's surface, possibly due to degradation and burial by fluvial erosion and aeolian infilling. This is similar to the reduced number of craters seen on Earth, which is a result of both endogenic and exogenic processes, like erosion and weathering. Given these similarities, Earth serves as a strong analogue for studying Titan's craters. There are 200 confirmed craters on Earth, of which 67 are buried and therefore unobservable from orbit. This study determines the percentage of the remaining 133 exposed terrestrial craters that can be identified in synthetic aperture radar data (SAR), in order to estimate the number of craters we may be missing in Cassini RADAR images of Titan. The results show that only ~50% of the terrestrial craters are distinctly visible in radar images; the remaining 50% were not clearly identified by the authors. These findings were further validated through a crowd-sourcing exercise, where users attempted to identify craters in a smaller sample of radar images. If a similar number of craters are obscured on Titan, it suggests that 50% of the craters are not visible in the Cassini RADAR data set. Thus, the surface age of Titan could be ~2x older (~400 Ma – 2 Ga) than currently hypothesized (~200 Ma – 1 Ga).

#### 2.1 Introduction

Impact cratering is a fundamental geologic process that is pervasive throughout the solar system. Impact craters are geologically important because they provide information about the composition, interior structure, and surface processes of planetary bodies (Melosh, 1989; Osinski & Pierazzo, 2012). Significant effort has thus been put into identifying, studying, and mapping impact craters in our solar system.

One planetary body of particular interest is Titan, Saturn's largest moon. Titan has a thick, nitrogen-rich atmosphere and flowing liquids (methane and possibly ethane) on its surface, which supports an active hydrological cycle similar to Earth (e.g. Atreya et al.,

2006; Tokano et al., 2006; Lunine & Atreya, 2008; Hayes et al., 2018). Studying craters on Titan teaches us about the evolution of its surface and provides better constraints for its surface age. In the 2030s, NASA's Dragonfly mission will explore the region around Selk crater (Lorenz et al., 2021). The data collected will provide further insight about the impact cratering process and surface evolution on Titan (Turtle et al., 2020; Barnes et al., 2021).

On planetary bodies with thick atmospheres, such as Titan, synthetic aperture radar (SAR) instruments are often used to image the surface. Radio waves are able to penetrate atmospheres that are opaque at visible wavelengths due to clouds or haze (Elachi, 1987). These radar images highlight differences in slope, composition, and roughness of a surface, key properties in crater mapping (Neish & Carter, 2014). The Radio Detection and Ranging (RADAR) instrument on board the Cassini spacecraft mapped more than two-thirds of the surface of Titan, at a maximum resolution of 175 m (Lopes et al., 2019). Hedgepeth et al. (2020) presented a final count of 90 possible craters on the surface of Titan, based on 69% surface coverage by the Cassini RADAR instrument; the distribution of these craters is shown in **Figure 2.1a**.

This is an extremely small number compared to the crater populations documented on other nearby Saturnian satellites (Lorenz et al., 2007). For example, the number of impact craters on Rhea, Titan's neighbouring satellite, is on the order of  $10^3$  craters for diameters  $D \geq 10$  km (Kirchoff & Schenk, 2008; 2009). In comparison, there are only 72 possible craters with diameters larger than 10 km on Titan (Hedgepeth et al., 2020). Even after correcting for incomplete SAR coverage, the crater count on Titan remains low (Hedgepeth et al., 2020). The low crater count on Titan may be a result of several factors including atmospheric shielding (for craters  $D < 20$  km), erosion and burial of craters by exogenic processes, impacts into marine environments, a rapid resurfacing mechanism on Titan in the recent past, and/or viscous relaxation (Korycansky & Zahnle, 2005; Neish et al., 2013; Neish & Lorenz, 2014; Neish et al., 2016; Schurmeier & Dombard, 2018; Schurmeier et al., 2023). The reduced number of craters on Titan compared to Rhea is similar to the relatively smaller number of craters on Earth compared to the heavily cratered lunar surface. Craters with diameters larger than 10 km on the Moon are on the order of  $\sim 10^3$  to  $10^4$  (e.g. Rodionova et al., 1987; Robbins, 2018), whereas there are only 86 on

Earth. Indeed, Earth is an excellent analogue for Titan because both worlds have active hydrological systems, with water as the working fluid on Earth and methane on Titan. Erosion and burial are therefore important processes responsible for crater degradation on both surfaces.

There are 200 confirmed craters on Earth (**Figure 2.1b**), which have been identified by a combination of remote sensing, field, and laboratory studies (Osinski & Grieve, 2019; Kenkmann, 2021; Osinski et al., 2022). Of these craters, 67 are buried and therefore unobservable from orbit. In particular, craters formed in marine environments (which are also present on Titan) lack significant surface topography that may prevent them from being recognized from orbit (Collins & Wünnemann, 2005; Neish & Lorenz, 2014; Wakita et al., 2022). On Earth, these craters are identified from drill cores, detailed gravity surveys, and seismic profiling (e.g., Poag et al., 1994). However, field studies and drill cores are not available for Titan. To properly compare the terrestrial impact crater population to that of Titan, Earth impacts have to be analyzed using the same instrumentation that is available for Titan, i.e., radar remote sensing. Previous radar studies of terrestrial impact structures have shown that radar sensitivity to surface composition enhances topographic features resulting from the impact (Mchone et al., 2002), and post-impact processes such as erosion can affect the radar signature (Smith et al., 1999).

In this work, we determine the visibility of all 133 non-buried terrestrial craters (i.e., craters that are exposed at the surface) in radar images. We exclude the buried craters from the study as they would be unobservable via orbit, and therefore, cannot be compared to Titan. This study will help us to determine a more accurate crater population and density for Titan, placing better constraints on the age of its surface. Surface age is a critical value for models of the formation and evolution of Titan (e.g. Tobie et al., 2006; Hörst, 2017). In addition, crater counts may provide insight into the changing atmospheric density of Titan over time (Engel et al., 1995). All these factors will help us to determine a comprehensive evolutionary history for Titan.

We note that vegetation cover and urbanization are factors that can impair the visibility of craters on Earth, factors that are not present on Titan. However, we assume

that these factors are minor compared to the large-scale erosion and infilling processes that impair the visibility of craters on both Earth and Titan in SAR images. Additionally, surrounding topography (i.e. volcanic features) can hinder crater identification in radar images. Since many volcanic features also appear circular, it can be difficult to distinguish them from impact craters in radar images, without topographic information. To mitigate this challenge, we include topography data in our analysis of terrestrial craters. We note there is a lack of topographic coverage on Titan, and so direct comparisons are not possible with Earth. However, our study serves as a test for the importance of topography data in crater identification. Given these considerations, we use the percentage of craters not visible on Earth as a first-order approximation for the observability of craters on Titan. This will help us to place a better constraint on Titan's surface age.

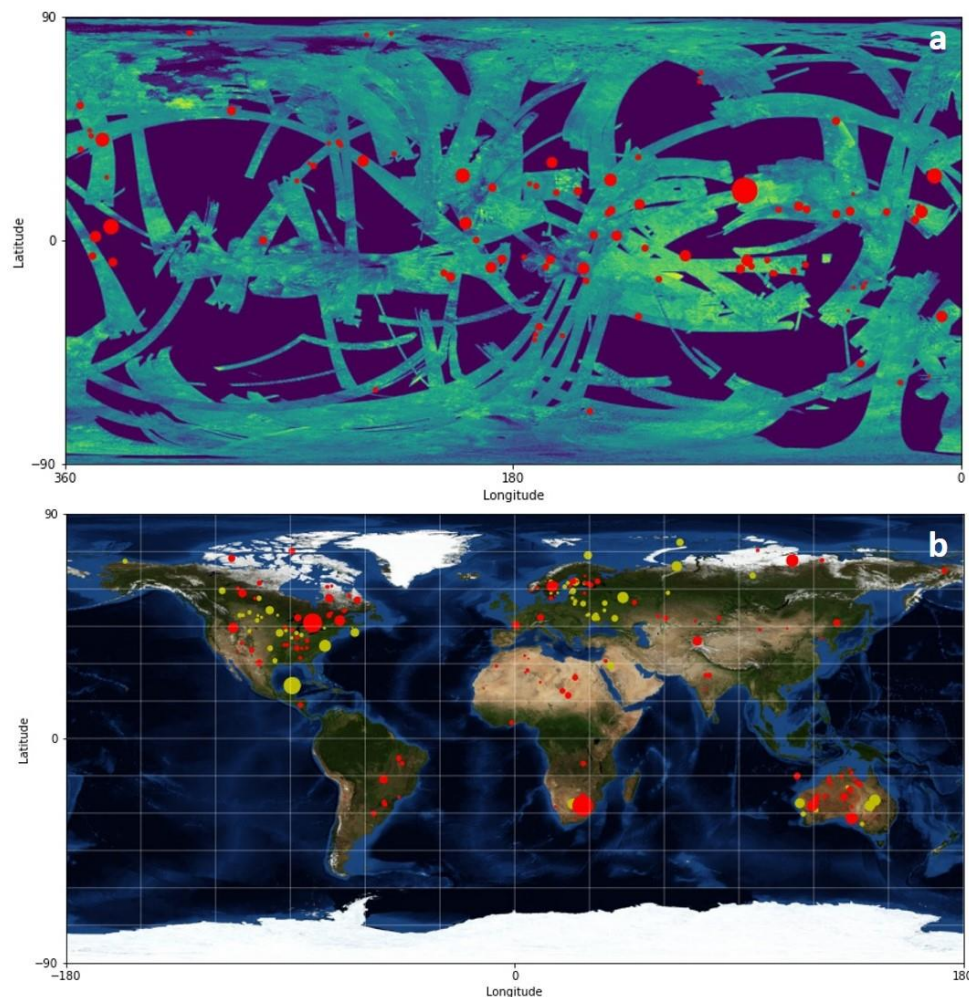


**Figure 2.1: (a) Cassini HiSAR global mosaic of Titan (Elachi et al., 2005; Stephan et al., 2009) showing 90 possible impact craters represented by red circles (modified from Hedgepeth et al., 2020). (b) A global map of 200 confirmed impact craters on Earth. Of the 200, 67 are buried (yellow) and 133 are non-buried (red) craters (Impact Earth Database). Circle size is scaled in proportion to the crater diameter.**

## 2.2 Methodology

To characterize terrestrial craters with radar images, we used data from two satellites: the European Space Agency’s (ESA) Sentinel-1 (Attema et al., 2009) and the Japanese Aerospace Exploration Agency’s (JAXA) Advanced Land Observation Satellite (ALOS) Phased Array type L-band Synthetic Aperture Radar (PALSAR) (Rosenqvist et al., 2007). We used Sentinel-1 and PALSAR data because of their global coverage; other

terrestrial sensors that operate at shorter wavelengths (e.g. TerraSAR-X) do not have publicly available global coverage. More specifically, we used Level-1 Interferometric Wide (IW) Swath Single Look Complex (SLC) products from Sentinel-1, which has 5x20 meter spatial resolution and a 250 km wide swath. Level 1.1 SLC products were sourced from PALSAR's Fine Beam Single (10 m resolution) and Double (20 m resolution) polarization modes which contain 70 km wide swaths. Sentinel-1 uses a shorter wavelength (5.6 cm) compared to PALSAR (24 cm), which allows for the investigation of surface roughness at both the centimeter and decimeter scales; radar is sensitive to roughness near the transmitting wavelength. For comparison, Cassini RADAR was a Ku-band (2.17 cm) sensor. Although the three sensors all operate at the centimeter and decimeter scale, they may produce different backscattered signatures from similarly rough surfaces due to SAR's high sensitivity to surface roughness. Nevertheless, for qualitative observations of craters, they still serve as reasonable comparisons.

We processed the terrestrial radar images in the Sentinel Application Platform (SNAP), a toolbox used for Earth Observation processing and analysis. There are three common processing steps for both datasets, and one only applicable to the Sentinel-1 data. 1) First, we applied a radiometric calibration so the pixel values represent the radar backscatter (Miranda & Meadows, 2015). 2) The next step was only applied to the Sentinel-1 data. The IW SLC products contain a series of burst images per sub-swath and one per polarisation channel, for a total of three (single polarisation) or six (dual polarisation) images. Each burst is processed as a separate SLC image, and therefore has to be merged into one product before continuing. 3) The following processing step (applicable to both datasets) is multilooking. This averages the range and/or azimuth pixels to increase the number of looks per pixel, and thus, reduces the speckle noise. This improves the signal to noise of the images, but degrades their spatial resolution. After this step, the image will have an approximately square pixel spacing after being converted from slant to ground range. In our processing, we specify the number of looks in range and azimuth such that the resulting mean pixel size is approximately 100 x 100 m. We use this average to strike a balance between noise and resolution, as a decrease in noise also results in a decrease in resolution. 4) The final step is applying a geometric range-Doppler terrain correction to correct the SAR geometric distortions using a Digital Elevation Model (DEM). The DEMs

used include a 30-meter resolution DEM from the Shuttle Radar Topography Mission (SRTM) (Farr et al., 2007), which extends to 60° N and 60° S, and a 90-meter TanDEM-X DEM (Zink et al., 2007) for craters in the polar regions. The terrain-corrected radar images of non-buried craters produced in this work will be made available on the Impact Earth Database (<https://impact.uwo.ca/map/>).

In addition to the radar data, we used the topography data listed above to aid in crater identification. The DEMs provide elevation data, which is useful in highlighting the characteristic circular depression of an impact crater.

### 2.2.1 Crater Visibility Criteria

The main objective of this work is to characterize the visibility of all exposed terrestrial craters in radar images. To do this, we used the following criteria to determine if a crater was visible in a radar image: (1) The presence of a circular feature, (2) a radar bright rim and ejecta blanket paired with (3) a radar dark crater floor. We note that not all craters are perfectly circular, and there are other geological features that have a circular shape (i.e. a volcanic caldera). As a result, we look for isolated circular features in order to avoid volcanic fields. Bright rims are common features observed in radar images of impact craters, because crater rims and ejecta are typically fractured and blocky, producing bright radar returns. A dark crater floor is likely the result of sediment infill, causing the crater floor to be filled with a smooth and/or absorbing material (common for Earth and Titan). An example of this is shown in a radar image of the Lawn Hill crater located in Queensland, Australia (**Figure 2.2**). In the case of Lawn Hill crater, the radar brightness of the rocky rim could be associated with a peak ring structure (Darlington and Blenkinsop, 2013; Lees and O’Donohue, 2024). Other examples of impact craters in a variety of degradation states on Earth and Titan are shown in **Figure 2.3**. **Figures 2.3a/b** show examples of fresh and degraded craters on Earth, whereas Figures 2.3c/d show similarly fresh and degraded craters on Titan. **Figures 2.3e/f** show craters that are characterized as not visible in radar images with their nominal locations highlighted.

To reduce ambiguity, we limited our characterization to only two categories: “visible” or “not visible”. In the case where a crater is deemed “not visible”, we added



topography data to look for the presence of a topographic depression. Topographic data is generally not available on Titan, but we wanted to determine how useful topography data is in identifying craters for use in future missions. We discuss the results of this analysis in **Section 2.3.2.**

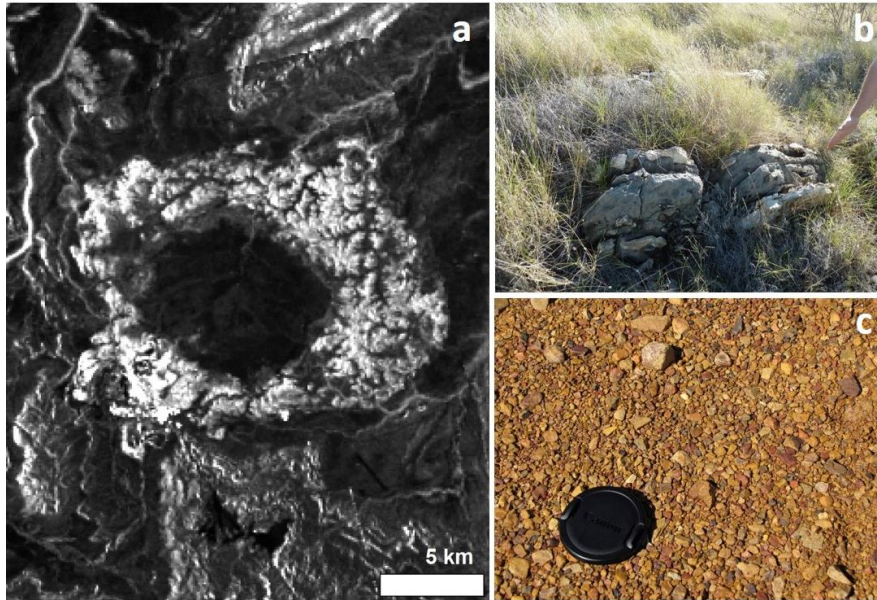


**Figure 2.2:** (a) PALSAR image (© JAXA, METI 2007) of the ~17 km diameter Lawn Hill crater in Queensland, Australia showing a radar bright rim/ejecta blanket and a radar dark crater floor. Characteristic field photographs of the (b) radar bright rim and (c) radar dark floor are shown on the right, with an arm and a lens cap for scale, respectively. Lawn Hill crater photo credits: R. Lorenz, J. Radebaugh, and J. Barnes.

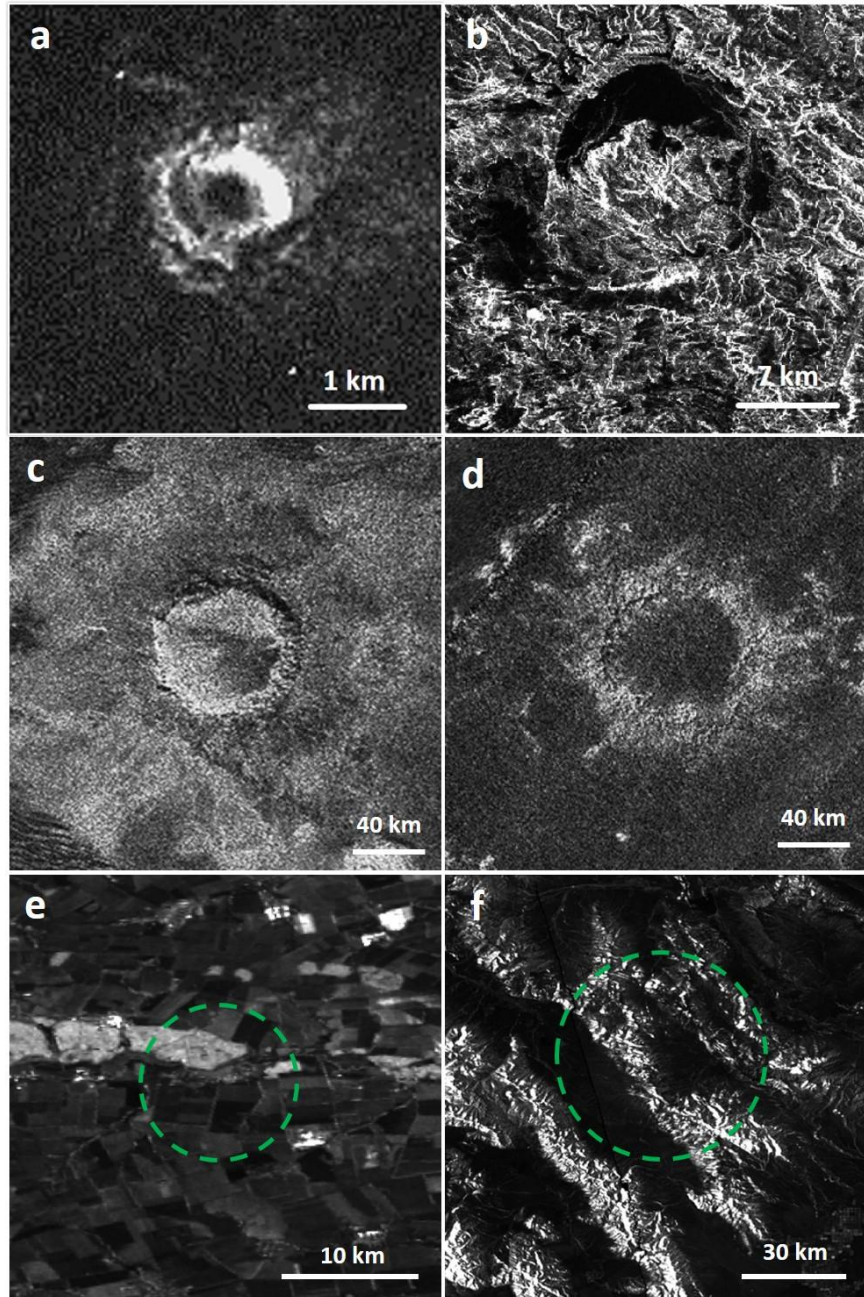


**Figure 2.3:** (a) Sentinel-1 image of the fresh 1.2 km diameter Barringer crater in Arizona, U.S.A and (b) PALSAR image (© *JAXA, METI 2007*) of the degraded 12 km diameter Gweni-Fada crater in Chad. (c) Cassini RADAR image of the fresh Sinlap crater and (d) the degraded Soi crater on Titan, both ~80 km in diameter (Neish et al., 2016). (e) Sentinel-1 image of the 12 km diameter Karla crater in Russia and (f) Sentinel-1 image of the 60 km diameter Beaverhead crater in Montana, U.S.A. The green dashed circles represent the nominal location of these “invisible” craters.

## 2.3 Results

### 2.3.1 Characterization of Visibility

There are 133 exposed (or non-buried) craters on Earth, which could theoretically be visible with orbital imaging data. The characterization of all exposed craters (except one - we omitted Wabar crater in Saudi Arabia from analysis because it lacked appropriate radar data) shows that only 71 out of 132 craters (54%) are visible in radar images, based on the criteria outlined above (**Appendix C**). It should be emphasized that there were some craters that were more difficult to identify or more ambiguous than others, so there is an associated error with our characterization. Some craters only partially fulfilled the visibility criteria resulting in characterization ambiguities. For example, the Charlevoix crater (**Figure 2.4a**) exhibits a semi-circular pattern while the other half is buried in a waterbody. It also does not exhibit a typical radar-bright rim or radar-dark floor. The Zhamanshin crater (**Figure 2.4b**) serves as another example. Here, there is a loosely circular feature and a generally radar-dark floor region, but it is missing a bright rim and has some radar-bright material in the center. Out of the 132 craters, 13 (~10%) were initially categorized as “ambiguous”. For simplicity’s sake, these ambiguous craters were re-assessed and of the 13, 4 were eventually characterized as visible, whereas the other 9 were characterized as not visible in radar images.

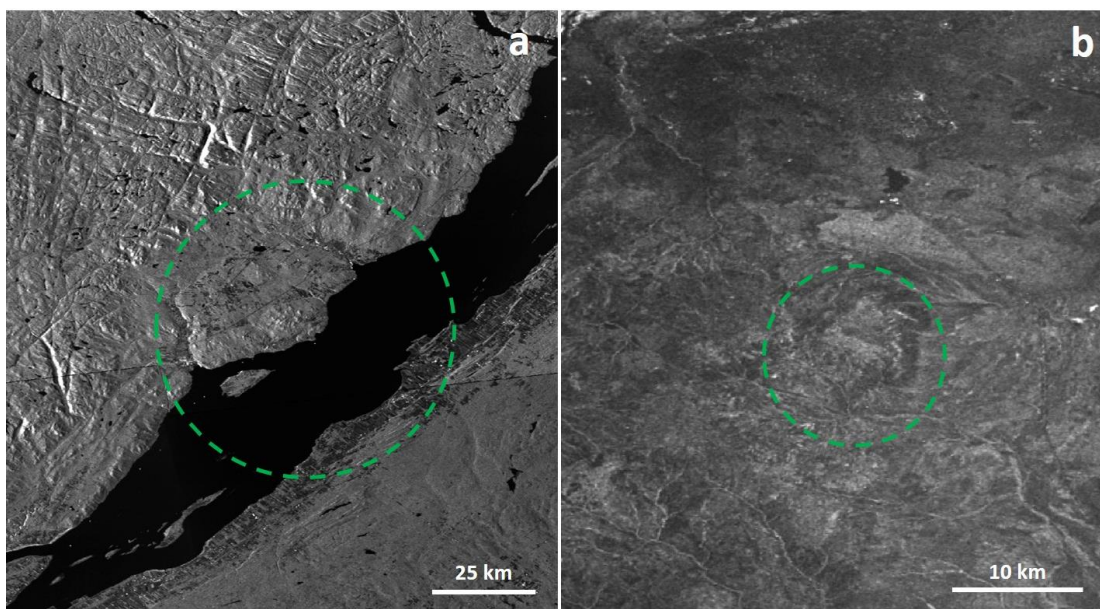


**Figure 2.4: Examples of ambiguous craters: (a) Sentinel-1 image of the 70 km diameter Charlevoix crater in Quebec, Canada and (b) the 13 km diameter Zhamanshin crater in Kazakhstan. The green dashed circles represent the nominal location of the craters. The Charlevoix and Zhamanshin craters were eventually characterized as visible and not visible, respectively.**

In addition to the characterization of their overall radar visibility, we investigate the distribution of visible vs. non-visible craters compared to parameters such as the crater's latitudinal location, size, target rock type, and age. Looking at the latitudinal variation (**Figure 2.5**), we see that the percentage of craters visible in radar is highest between  $30^{\circ}$  N and the equator. To determine if this is a statistically significant result, we performed a two sample Kolmogorov–Smirnov (K-S) test to assess if the visible and invisible craters are drawn from the same population; the underlying population distribution is assumed to be continuous. The null hypothesis is that the two distributions are drawn from the same population; a p-value of  $<0.05$  is required to reject this hypothesis. The test yielded a p-value of 0.275, meaning that the visible and non-visible distributions are drawn from the same population. This suggests that there is no underlying physical process responsible for the latitudinal variation we observe; the variations are not statistically significant. Note that there is a complete lack of craters south of  $40^{\circ}$ S, mainly due to the configuration of the continents (the only major landmass south of  $40^{\circ}$  is covered in ice.)

We next consider how crater visibility varies with crater diameter (**Figure 2.6**). We find that the smallest craters (<1 km diameter) are the most difficult to identify in radar images. This may be because the smallest craters are more difficult to resolve, since we are using a pixel spacing of only 100 m. However, visibility increases to 73% for craters 1-2 km in diameter. This aligns with the fact that small craters are more likely to be younger or “fresher” and therefore better preserved (e.g. Grieve & Robertson, 1979; Kenkmann, 2021). Craters 10-40 km in diameter have a relatively high percentage of radar visibility (60-80%), suggesting that these craters are also less degraded. Again, we performed a K-S test on the visible and invisible crater populations, and found a p-value of 0.075, which is not enough to reject the null hypothesis (p-value < 0.05) that both populations are drawn from the same distribution.

We also looked at the visibility of craters formed in different target rock types. Generally, crystalline material has higher material strength and therefore more resistant to erosion. In our study, we find that impacts into crystalline material are generally more visible (70%) compared to sedimentary or mixed material (~50%) (**Figure 2.7**). However, the K-S test suggests that the difference in visibility due to rock type is not statistically significant. Lastly, we looked at how the crater visibility varies with crater age. We did not observe any obvious trend related to the age of the crater, as the visibility percentage is ~50-60% for all age bins (associated with the four geological eras) (**Figure 2.8**).

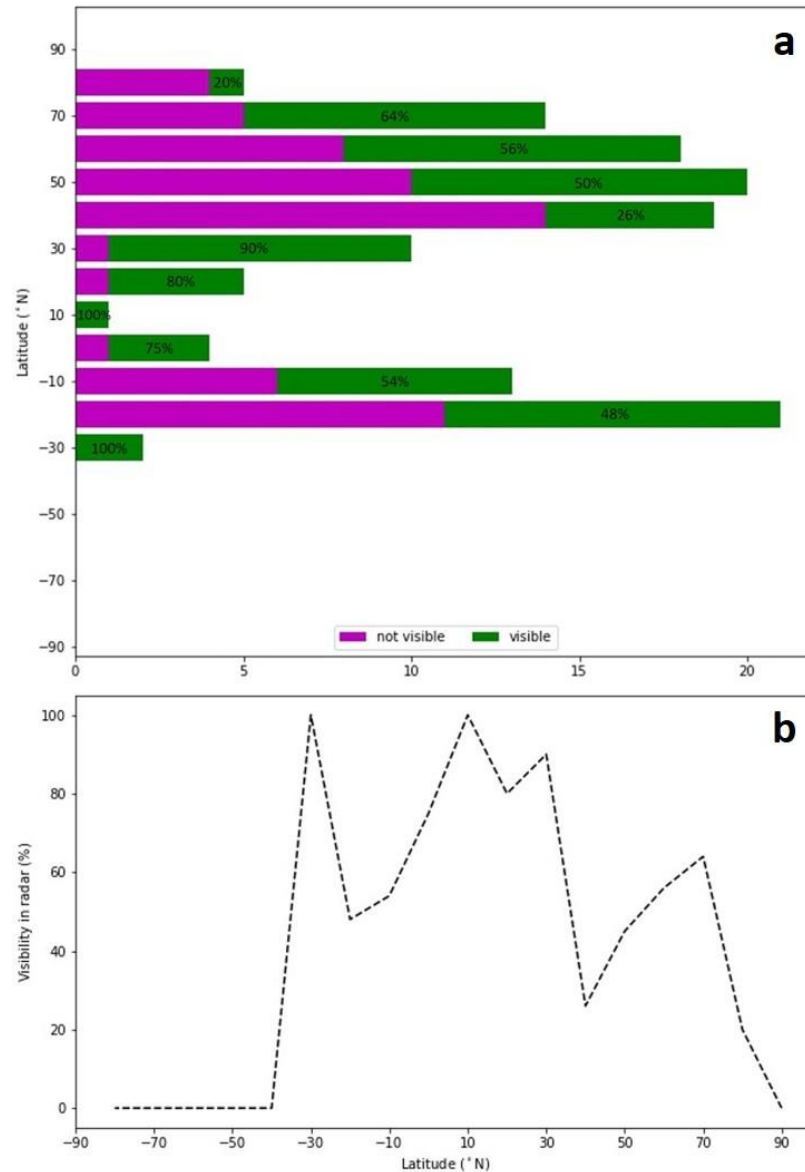


**Figure 2.5: Latitudinal variation in the radar visibility of craters. (a) The distribution of visible and non-visible craters compared to the total number of non-buried craters for 10° latitude bins. (b) The variation in percent of radar visibility of craters for 10° latitude bins.**

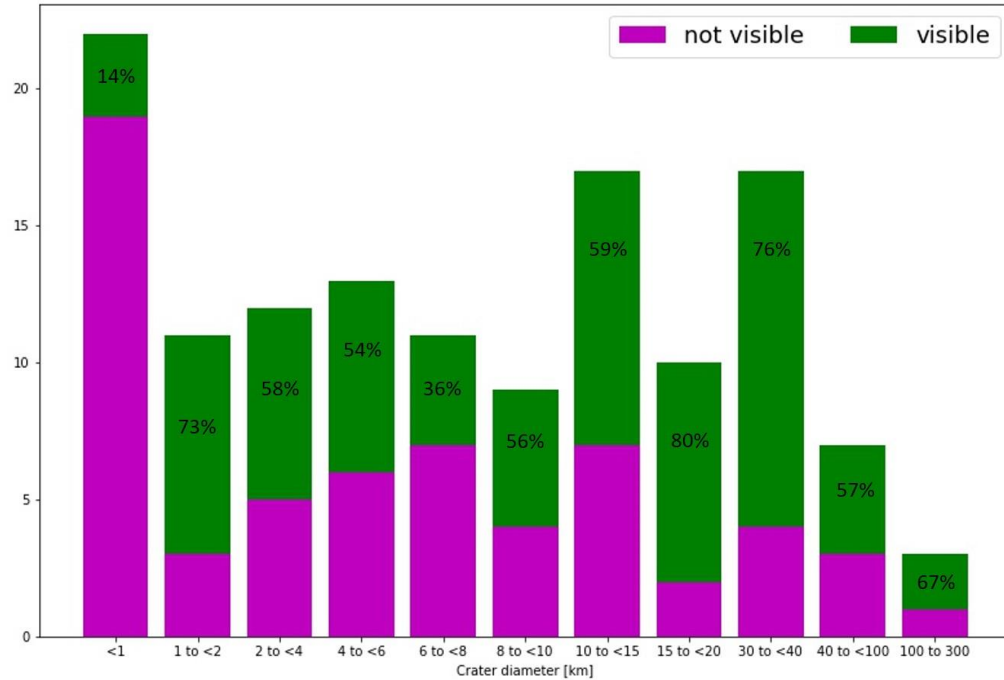


**Figure 2.6: The distribution of visible and non-visible craters compared to the crater diameter.**

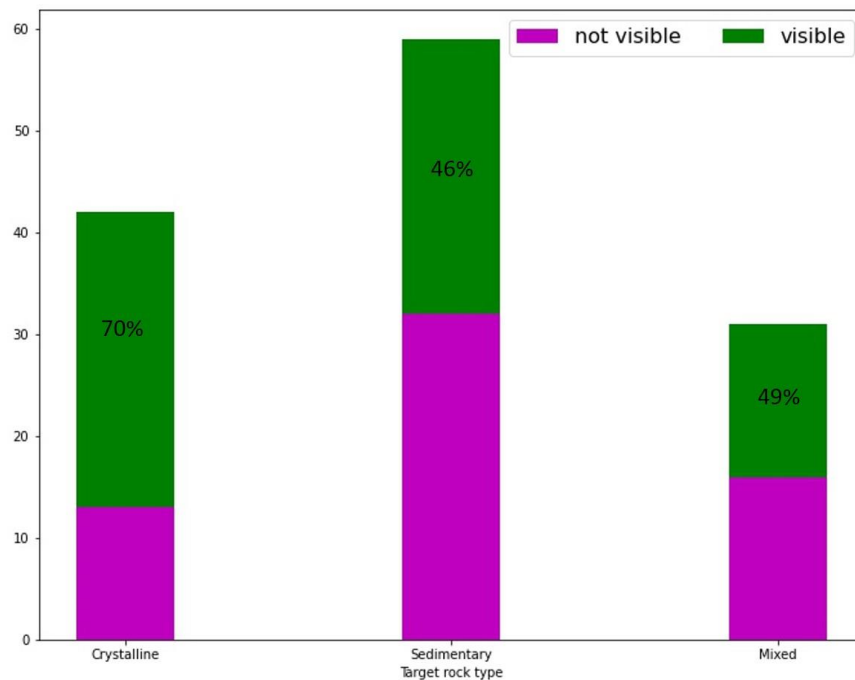


**Figure 2.7: The distribution of visible and non-visible craters compared to the impact target rock type.**

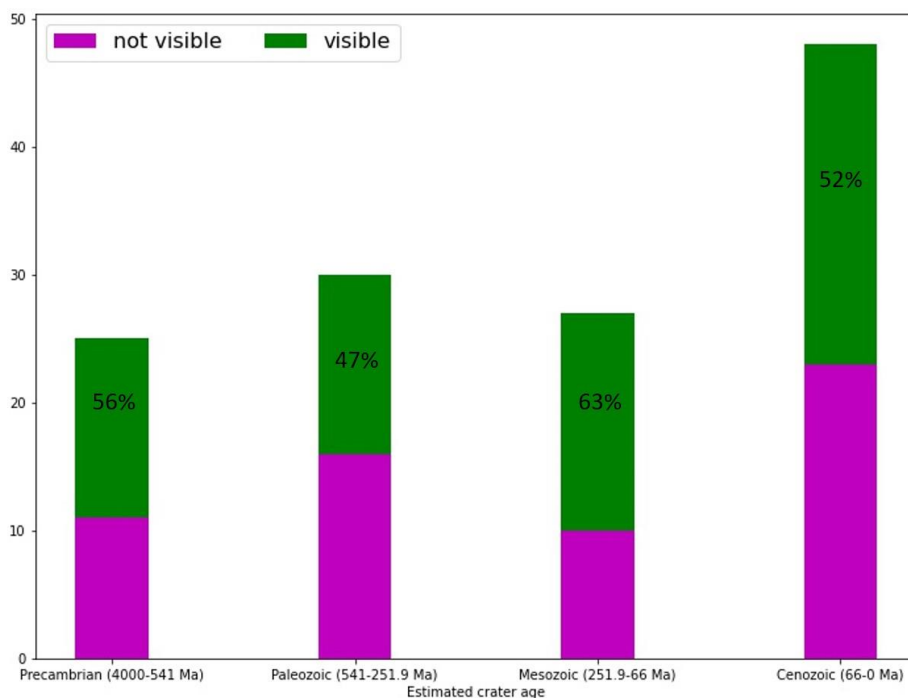


**Figure 2.8: The distribution of visible and non-visible craters compared to the estimated ages of the craters.**

### 2.3.2 Topography Data

We examined the topography data for all craters that were not visible in radar images to determine how topography data improves crater identification. There were 61 craters that were not visible in the radar data. With the addition of topography data, 12 more craters become apparent. This increases the total number of visible craters from 71 (~54%) to 83 (~63%) out of a total of 132. Therefore, topography data increases the visibility of craters by approximately 10%. Unfortunately, the topography data available for Titan are limited, especially at the scale required to identify impact craters (Lorenz et al., 2013). In particular, high-resolution stereo topography covers only ~2% of the surface (Kirk et al. 2012). These results suggest that acquiring more high-resolution stereo data with a future Titan mission would be beneficial for crater identification and characterization.



We found that topography data are useful to mitigate the challenges of crater identification in radar images. The addition of a DEM enhances crater visibility as seen in the case of the Vargeão Dome crater in **Figure 2.9**. There is extensive vegetation coverage in this region of Brazil, resulting in a uniformly bright radar image with minimal shading due to topography or surface roughness differences around the crater (**Figure 2.9a**). This can make it difficult to locate craters in terrestrial radar images. The DEM, on the other hand, displays a circular feature of uniformly low topography, aiding in our identification of the crater (**Figure 2.9b**). Additionally, the DEM helps us differentiate craters (generally, a topographic depression) from other circular features such as volcanic calderas. These are (typically) located on a topographic high, as seen in the case of Aorounga crater in **Figures 2.9c and 2.9d**. There are two circular features visible in the radar image (**Figure 2.9c**), which may be identified as a crater based on its radar bright rim and dark floor. However, it becomes apparent that the feature to the top left of **Figure 2.9c/d** is a volcano (Emi Koussi volcano, Chad) based on the DEM, which shows it is located on a topographic high. We note, however, that using a color-coded DEM in this context likely enhances the visibility of the crater structure. The human eye is generally more responsive to changes in color hues than to grayscale.

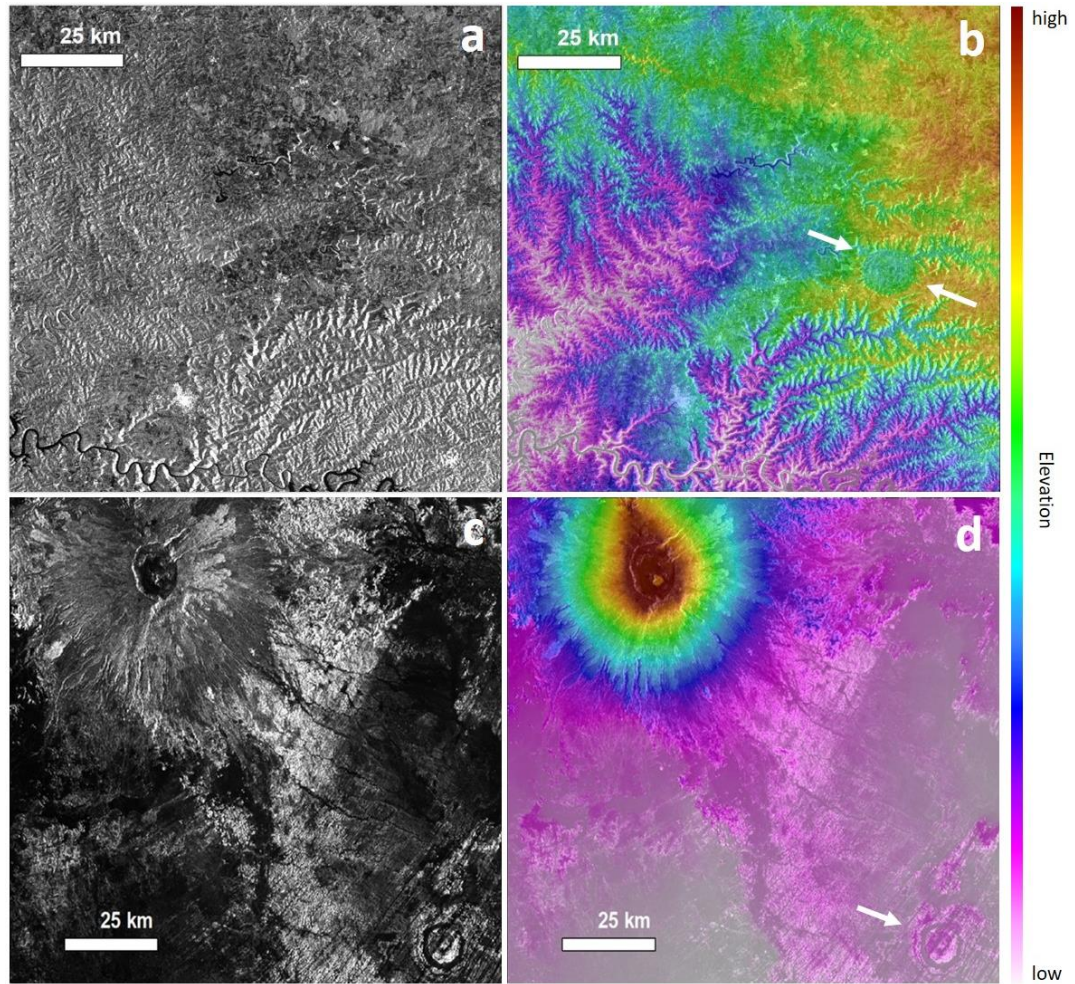


**Figure 2.9:** (a) Sentinel-1 radar image and (b) a 30 m resolution SRTM DEM of the 12 km diameter Vargeão Dome crater located in Brazil, overlaid on the Sentinel-1 radar image. (c) Sentinel-1 radar image and (d) a 30 m resolution SRTM DEM of the 16 km diameter Aorounga crater located in Chad. The craters are indicated with white arrows in (b) and (d). The circular feature located on a topographic high in the upper left in (d) is the Emi Koussi volcano.

### 2.3.3 Crowdsourcing Study

As previously mentioned, crater identification in radar images proved to be a difficult task with many ambiguities. The characterizations for the study were initially completed only by the lead author with input from the co-authors. Given that there is a general subjectivity to this task, we investigated whether there was significant observer bias via crowdsourcing. Other studies have employed crowdsourcing techniques for crater counting such as the Moon Zoo citizen science project (Bugiolacchi et al., 2016). This crowdsourcing project provided the volunteers with high resolution Lunar Reconnaissance Orbiter Camera (LROC) images to measure impact crater sizes and mark features of interest in the Apollo 17 region. The crowdsourced data was validated by an expert survey, which suggested that citizen science is a reliable method for conducting lunar surface studies, particularly crater counting. However, the study is limited to the one Apollo 17 region of the moon, and the expert validation surveys covered only a part of the crowdsourced region. Robbins et al. (2014) investigated the validity of such crowdsourcing studies by comparing the variability in lunar crater identification among expert and non-expert crater counters. This study employed different experts to study craters of different sizes (10 meters to a few kilometers in diameter) in different regions (highlands and mare) on the Moon. The level of agreement among the experts depended on the crater size, number of craters in the study region, and the terrain type. The results showed that although there is a large variation in crater identification among different users, many people identifying craters in the same area yields the most robust information. This is because even though an individual can perform more consistent counts compared to a group, there are biases and differences from day to day and even hour to hour for any given individual.

To investigate observer bias in our study, we set up a trial crowdsourcing campaign. As this was a trial, only 2 volunteers completed the entire survey; neither were an expert observer, but both had good knowledge of impact cratering and radar, and they were instructed to identify craters in radar images. The survey was set up with 13 images, out of which 3 were “blank” or “no crater” images. Based on this study, only 40% of the crowd marked craters matched the actual crater (with some diameter variations between users). Circular features (e.g. cinder cones) were often falsely identified as craters due to the lack

of topography data. Similarly, small cities (which sometimes appear radar bright and circular) were occasionally mapped due to lack of visible imagery to identify features such as buildings and roads. Another factor contributing to the difficulty in identifying the impact crater was the large area covered by the radar images (250 km wide swath images), which made it difficult to identify smaller craters.

We followed up on the initial trial by setting up a Zooniverse crowdsourcing project (<https://www.zooniverse.org/projects/sophiatrozzo/impact-crater-detections-on-earth-and-titan>), with 16 radar images of terrestrial craters and 4 blank images with no craters added as a control. The images were selected to prioritize landscape variability, and variable crater size. There were five images from Africa, five from Asia, seven from Australia, two from South America, and one from Europe. The different types of land masses included: volcanoes, sand dunes, desert landscapes, populated landscapes, rivers, and seas. The craters in the radar images varied in size (crater diameter) from 0.02 to 52 km. We adjusted the stretch, brightness, and contrast of the radar images for viewer clarity and added a scale bar prior to inclusion in the study. Most craters had two radar images (C-band and L-band); the image with the most clarity was selected for the survey. The twenty radar images were uploaded as JPEG files to Zooniverse, the largest universal citizen science crowd-sourcing site in the world. The Zooniverse project included a tutorial for survey participants; they were prompted to “draw a circle” around radar image features that represent impact craters (bright crater rim and dark crater floor). This criteria is analogous to the one used in the characterization process used by the lead author. The survey also included an example of an identified impact crater in a radar image. Zooniverse tracked the user’s crater radius (R) and the crater center location (X, Y). These results were then compared to results from two expert classifications.

There were on average 32 participants for each of the true crater images (crowdsourcing data is shown in **Appendix D**). Since the participants included both experts and public volunteers, we defined a successful crater identification as occurring where > 50% of users identified the crater. We used three different cut-offs for the radius measurement (within 10, 15, and 20% of the true crater radius). The radii of only 5/16 craters (31%) were easily found by our participants within the 15-20% crater radius error,

as shown in **Figure 2.10a**. This agrees well with the fact that radius is difficult to determine (Turtle et al., 2005), as it depends on the level of crater degradation. We used two different cut-offs for the location measurements (within 1 and 2 km of the true crater location). Based on this, the locations of only 6/16 craters (38%) were correctly identified within the 2 km error margin (see **Figures 2.10b/c**). These results are significant because they validate that terrestrial craters are difficult to identify in radar images, as suggested by the main study characterization. Crowdsourcing results suggest that only a third of craters are visible in radar images, while the main characterization completed by the authors indicate that about a half of the craters are visible. Given that participants in the crowdsourcing survey included non-experts in crater observation, this serves as the minimum percentage of craters that are visible in radar images. If only 38-54% of craters are visible in radar images on Earth, this implies that a large percentage of craters may be unobservable in radar images of Titan, and therefore missing from its crater record. In other words, 46-62% of the craters in the regions of Titan imaged with high-resolution SAR might be missing from its crater catalog. This is likely a minimum as Titan does not have global SAR coverage, so many more craters may remain unidentified.

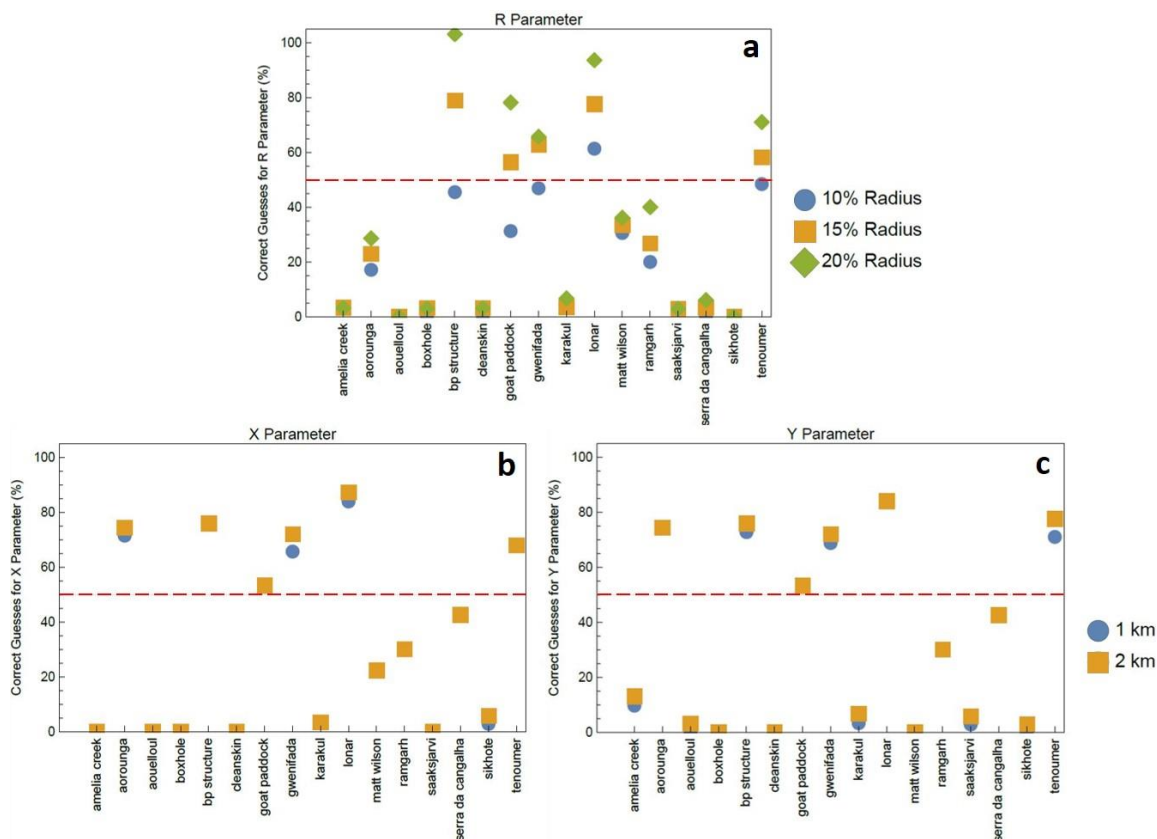


**Figure 2.10: Percentage of correct answers for the R (a), X (b), and Y (c) parameters, of those participants who drew a crater in the study area. We used three different cut-offs for the radius measurement (within 10, 15, and 20% of the true crater radius) and two different cut-offs for the location measurements (within 1 and 2 km of the true crater location). The locations of only 6/16 craters and the radii of only 5/16 craters were easily found by our participants (i.e., >50% correct, shown by the dotted red line).**

## 2.4 Discussion

Characterizing visibility of terrestrial craters in radar images implies that nearly half of craters (that would be theoretically observable via orbit) are not visible. Given the similarities of Earth and Titan, we extend this result to the crater population on Titan. This suggests that only 38-54% of the craters on Titan are visible in radar images. In other terms, 46-52% of craters are missing from its cratering record. The implication for the surface age of Titan is that it may be twice as old as currently hypothesized.

Results from radar mapping of Titan's surface suggest that erosion and burial are some of the most important processes responsible for crater degradation. These studies used measured crater densities to determine a global crater retention age of 200 Ma to 1 Ga for Titan (Lorenz et al., 2007; Wood et al., 2010; Neish & Lorenz 2012; Hedgepeth et al., 2020). These estimates are consistent with observations and models of Titan's evolution that suggest a methane outgassing event occurred ~500 Myr years ago (Hörst, 2017). Our results, however, suggest that the surface age may be much older, roughly 2x the age provided by cratering counting studies.

We can use these results to provide a new constraint for the surface age of Titan, and compare them to previous models for the evolution of Titan's surface. For example, Tobie et al. (2006) proposed that episodic outgassing of methane (stored as methane clathrates) is the source for the atmospheric methane on Titan based on a coupled thermal-orbital model. The model incorporated the low thermal conductivity of methane clathrate to determine the conditions and timings of the outgasings, and suggested three major outgassing episodes. The first episode occurred with the overturning of Titan's silicate core around 650 Myr (from the start of the solar system), forming a layer of methane clathrate above the ocean. The second outgassing occurs at 2 Gyr after differentiation when the core begins to convect. The third episode occurs around 4 Gyr (or 500 Ma) as the core begins to cool and the ocean begins to freeze. The ice layer begins to convect, forming thermal plumes that breach the clathrate layer and lead to clathrate dissociation. Tobie et al. (2006) suggest that Titan's surface age should align with the second outgassing event ~2 Gyr ago. This is because the initial two outgassing episodes likely caused a widespread distribution of liquid methane onto the surface for an extended duration, leading to significant modifications of large areas. In contrast, the most recent outgassing event would have been more controlled, affecting only specific localized regions. This estimate is in line with the new, revised age for Titan presented in this work (370 Ma to 2.6 Ga).

Other models provide a range of constraints on the age of Titan's methane-rich atmosphere. The age of Titan's methane-rich atmosphere may coincide with the age of its surface, if exogenic processes such as fluvial erosion are primarily responsible for the degradation of its impact craters. (Though, we note that a nitrogen-dominated atmosphere,

as suggested by Charnay et al. (2014), would not be capable of such erosion). For instance, evolution models examining  $^{12}\text{C}/^{13}\text{C}$  and D/H isotopic ratios suggest an age of 60-1660 Myr ago, assuming methane is depleted by photochemistry alone. The age decreases to less than 10 Myr ago in the presence of hydrodynamic escape of methane (Nixon et al., 2012; Hörst, 2017). Isotopic evolution models considering methane replenishment suggest a range of <470 Myr ago (without replenishment) to <940 Myr ago (with replenishment) (Mandt et al., 2012; Hörst, 2017).

One can also use dynamical models to constrain Titan's surface age. A recent study by Bottke et al. (2023) uses a new model to investigate the "missing" early history of the giant planet satellites and calculate their surface ages. They track the collisional and dynamical evolution of the primordial Kuiper belt (PKB), which the model suggests lasted approximately 20 Myr after the dissipation of the solar nebula. The collisional model inputs are based on their ability to reproduce crater size-frequency distributions (SFDs) on icy satellites. The results suggest that most of the satellites have been hit with impactors larger than what is seen from their cratering record. These large impacts occurred very early in the moons' history, which led to multiple surface resetting events. The study looked at a crater production model for different giant planet satellites, and suggests a surface age for Titan of 1.8 Gyr (B. Bottke, personal communication, 2023). These results are based on the observed craters on Titan's surface, though. If half of Titan's craters are unobservable, then Titan's surface age could be older than 3 Gyr. This does not agree with the ages predicted by the interior evolution model of Tobie et al. (2006) or the age of Titan's methane-rich atmosphere.

Here, we explore some of the limitations of the study. First and foremost, we assume that erosion and burial are the dominant processes for crater degradation, globally, on Earth and Titan. This assumption has some drawbacks, since plate tectonics would eventually erase many craters on Earth, whereas the craters on Titan are unlikely to be affected by this level of tectonism. However, we note that we do not see a strong correlation between the age of the target rock (which is different from the age of the crater) and the percent of preserved craters on Earth (**Figure 2.11**). This would suggest that erosion and weathering are more important for continental crater degradation than tectonism. In



addition to erosion and burial being the more important crater degradation processes, we assume global erosional rates. We have not taken into consideration that erosional rates are going to be different depending on the depositional environment. Therefore, another potential consideration for future work would be investigate the local and regional depositional environments of the non-buried craters on Titan. It would be interesting to look at the preservation rates (or percent visibility) in an arid environment versus an environment with more fluvial activity to better constrain the crater populations.

Moreover, vegetation cover and urbanization are other factors only present on Earth that might obscure crater visibility. For example, trees (due to their leaves and branches) cause volume scattering resulting in a strong radar backscatter (Elachi, 1987). Thus, areas with large vegetation cover result in uniformly bright radar images obscuring other bright features in the region, as seen in **Figure 2.9a**. Urban environments similarly appear as bright targets in a radar image because flat surfaces with right angles (such as apartment buildings and houses) reflect back much of the radar energy. There are examples of some craters in our study that were affected by the presence of human settlements, but this is not something we explicitly investigated further.

Radar images may also vary with wavelength, given that each wavelength is sensitive to a different roughness scale and penetration depth. We compared the difference in crater visibility between the C-band and L-band images, and found that they agreed for most cases except where L-band data had low to no coverage of the region. This further justifies that for the purposes of this study, any centimeter and decimeter scale sensor should be sufficient. Another factor to consider is the difference in substrate, i.e., rock versus ice, for Earth and Titan, respectively. Quantitatively, water-ice has a higher radar reflectivity compared to a rocky surface (e.g. Neish & Carter, 2014; Hofgartner & Hand, 2023). However, we are qualitatively looking for a relative brightness difference between the bright rim/dark floor and the surrounding terrain. Assuming the substrate is homogeneous, craters should look qualitatively similar in radar images regardless of the composition of the surface. Lastly, one important parameter is the sensor resolution. As mentioned previously, the approximate resolution for the terrestrial radar sensors is 100 m/pixel, where the Cassini RADAR resolution is at most 175 m/pixel (Lopes et al., 2019).

We degraded one of our terrestrial images to Cassini resolution to investigate the effect on crater identification. We find that for terrestrial craters similar in size to those on Titan ( $D > 20$  km), the difference in resolution from  $\sim 200$  to 100 m/pixel does not affect the visibility of the crater. Accounting for the sensor wavelength, sensor resolution, and substrate, the terrestrial radar sensors should be comparable to the Cassini RADAR for the purpose of crater identification.

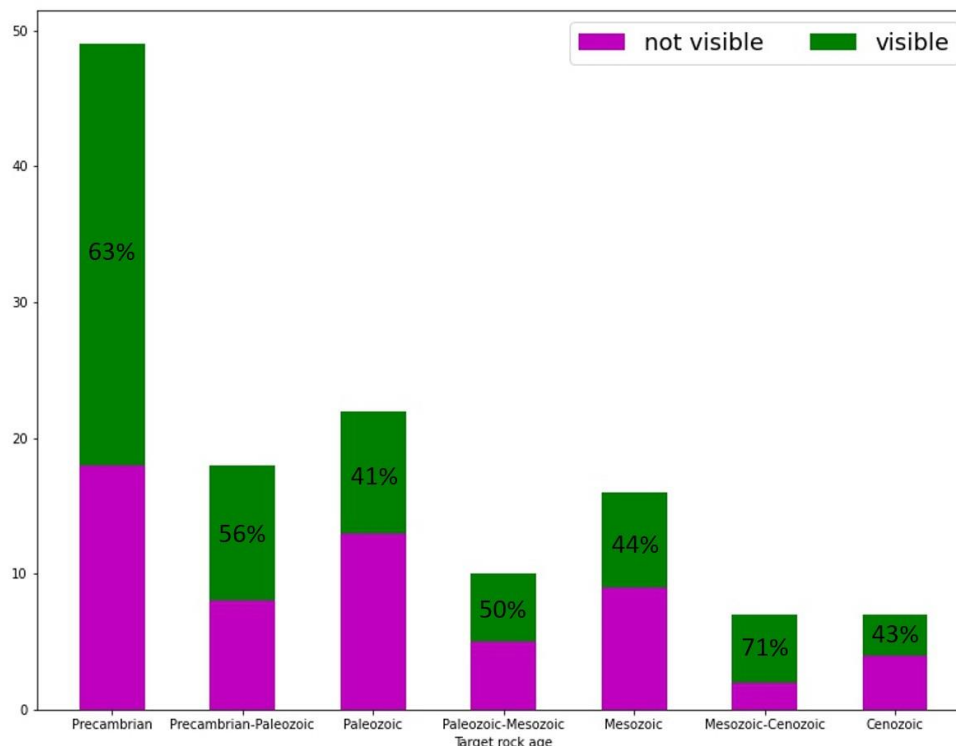


**Figure 2.11: The distribution of visible and non-visible craters compared to the age of the target rock. Note that the age of the target rock is different than the age of the crater shown in Figure 2.8.**

## 2.5 Conclusions

Currently, there are 200 known impact craters on Earth. Of these, 67 are buried, leaving them unobservable via orbit. A complete characterization of the remaining 133 exposed terrestrial craters helps us to better constrain the crater population and density on Titan, assuming both worlds are subject to erosion and weathering that degrades craters beyond recognition. These values are important for constraining the surface age of Titan,

and provide insight on surface processes and resurfacing mechanisms there. The results of this study suggest that about a half to two thirds of exposed craters on Earth are not visible in radar images. If similar processes are at work on Titan, the results suggest that approximately 46 to 62% of the craters there are not visible in the Cassini high-resolution SAR imagery. This has strong implications for the derived surface age of Titan, suggesting that the surface is older than currently believed. Using the previous age estimate of 200 Ma to 1 Ga, this suggests Titan's surface may be as old as ~400 Ma to 2 Ga.

## 2.6 References

- Atreya SK, Adams EY, Niemann HB, et al (2006) Titan's methane cycle. *Planet Space Sci* 54:1177–1187. <https://doi.org/10.1016/J.PSS.2006.05.028>
- Attema E, Davidson M, Snoeij P, et al (2009) Sentinel-1 Mission Overview. *IEEE Trans Geosci Remote Sens* 36–39
- Barnes JW, Turtle EP, Trainer MG, et al (2021) Science Goals and Objectives for the Dragonfly Titan Rotorcraft Relocatable Lander. *Planet Sci J* 2:130. <https://doi.org/10.3847/PSJ/abfdcf>
- Bottke WF, Vokrouhlický D, Marschall R, et al (2023) Exploring the missing early history of the giant planet satellites. In: 54th Lunar and Planetary Science Conference p 1581
- Bugiolacchi R, Bamford S, Tar P, et al (2016) The Moon Zoo citizen science project: Preliminary results for the Apollo 17 landing site. *Icarus* 271:30–48. <https://doi.org/10.1016/J.ICARUS.2016.01.021>
- Charnay B, Forget F, Tobie G, et al (2014) Titan's past and future: 3D modeling of a pure nitrogen atmosphere and geological implications. *Icarus* 241:269–279. <https://doi.org/https://doi.org/10.1016/j.icarus.2014.07.009>
- Collins GS, Wünnemann K (2005) How big was the Chesapeake Bay impact? Insight from numerical modeling. *Geology* 925–928. <https://doi.org/10.1130/G21854.1>
- Darlington VJ, Blenkinsop TG (2013) Dimensioning the Lawn Hill Impact Structure: A Peak Ring Crater of NW Queensland. In: 76th Annual Meeting of the Meteoritical Society. p 5028
- Elachi C (1987). *Spaceborne Radar Remote Sensing: Applications and techniques*. IEEE Press

- Elachi C, Wall S, Allison M, et al (2005) Cassini Radar Views the Surface of Titan. *Science* 308:970 – 974. <https://doi.org/10.1126/science.1109919>
- Engel S, Lunine JI, Hartmann WK (1995) Cratering on Titan and implications for Titan's atmospheric history. *Planet Space Sci* 43:1059–1066. [https://doi.org/10.1016/0032-0633\(95\)00044-6](https://doi.org/10.1016/0032-0633(95)00044-6)
- Farr TG, Rosen PA, Caro E, et al (2007) The Shuttle Radar Topography Mission. *Rev Geophys* 45. <https://doi.org/https://doi.org/10.1029/2005RG000183>
- Grieve RAF, Robertson PB (1979) The terrestrial cratering record: I. Current status of observations. *Icarus* 38:212–229. [https://doi.org/https://doi.org/10.1016/0019-1035\(79\)90179-9](https://doi.org/https://doi.org/10.1016/0019-1035(79)90179-9)
- Hayes AG, Lorenz RD, Lunine JI (2018) A post-Cassini view of Titan's methane-based hydrologic cycle. *Nat Geosci* 11:306–313. <https://doi.org/10.1038/s41561-018-0103-y>
- Hedgepeth JE, Neish CD, Turtle EP, et al (2020) Titan's impact crater population after Cassini. *Icarus* 344:113664. <https://doi.org/10.1016/j.icarus.2020.113664>
- Hofgartner JD, Hand KP (2023) A continuum of icy satellites' radar properties explained by the coherent backscatter effect. *Nat Astron* 7:534–540. <https://doi.org/10.1038/s41550-023-01920-2>
- Hörst SM (2017) Titan's atmosphere and climate. *J Geophys Res Planets* 122:432–482. <https://doi.org/10.1002/2016JE005240>
- Kenkmann T (2021) The terrestrial impact crater record: A statistical analysis of morphologies, structures, ages, lithologies, and more. *Meteorit Planet Sci* 56:1024–1070. <https://doi.org/https://doi.org/10.1111/maps.13657>
- Kirchoff MR, Schenk P (2008) Bombardment History of the Saturnian Satellites. In: *Workshop on Early Solar System Impact Bombardment*

- Kirchoff MR, Schenk P (2009) Crater modification and geologic activity in Enceladus' heavily cratered plains: Evidence from the impact crater distribution. *Icarus* 202:656–668. <https://doi.org/10.1016/j.icarus.2009.03.034>
- Kirk RL, Howington-Kraus E, Redding B, et al (2012) Topographic Mapping of Titan. In: 43rd Lunar Planetary and Science Conference p 2759
- Korycansky DG, Zahnle KJ (2005) Modeling crater populations on Venus and Titan. *Planet Space Sci* 53:695–710. <https://doi.org/10.1016/J.PSS.2005.03.002>
- Lees T, O'Donohue D (2024) Formation of the Lawn Hill Impact Structure. *Aus J of Earth Sci* 71:307-318. <https://doi.org/10.1080/08120099.2023.2291729>
- Lopes RMC, Wall SD, Elachi C, et al (2019) Titan as Revealed by the Cassini Radar. *Space Sci Rev* 215:33. <https://doi.org/10.1007/s11214-019-0598-6>
- Lorenz RD, Wood CA, Lunine JI, et al (2007) Titan's young surface: Initial impact crater survey by Cassini RADAR and model comparison. *Geophys Res Lett* 34:1–5. <https://doi.org/10.1029/2006GL028971>
- Lorenz RD, Stiles BW, Aharonson O, et al (2013) A global topographic map of Titan. *Icarus* 225:367–377. <https://doi.org/10.1016/j.icarus.2013.04.002>
- Lorenz RD, MacKenzie SM, Neish CD, et al (2021) Selection and Characteristics of the Dragonfly Landing Site near Selk Crater, Titan. *Planet Sci J* 2:24. <https://doi.org/10.3847/PSJ/abd08f>
- Lunine, J, Atreya, S (2008) The methane cycle on Titan. *Nature Geosci* 1:159–164. <https://doi-org.proxy1.lib.uwo.ca/10.1038/ngeo125>
- Mandt KE, Waite JH, Teolis B, et al (2012) The 12 C/ 13 C Ratio on Titan From Cassini INMS Measurements and Implications for the Evolution of Methane. *Astrophys J* 749:160. <https://doi.org/10.1088/0004-637X/749/2/160>

- Mchone JF, Greeley R, Williams KK, et al (2002) Space shuttle observations of terrestrial impact structures using SIR-C and X-SAR radars. *Meteor & Planet Sci* 37: 407-420. <https://doi.org/10.1111/j.1945-5100.2002.tb00824.x>
- Melosh JH (1989) *Impact cratering: A geological process*. Clarendon Press, Oxford.
- Miranda N, Meadows PJ (2015) Radiometric Calibration of S-1 Level-1 Products Generated by the S-1 IPF. ESA Technical Report ESA-EOPG-CSCOP-TN-0002
- Neish CD, Lorenz RD (2012) Titan's global crater population: A new assessment. *Planet Space Sci* 60:26–33. <https://doi.org/10.1016/j.pss.2011.02.016>
- Neish CD, Kirk RL, Lorenz RD, et al (2013) Crater topography on Titan: Implications for landscape evolution. *Icarus* 223:82–90. <https://doi.org/https://doi.org/10.1016/j.icarus.2012.11.030>
- Neish CD, Lorenz RD (2014) Elevation distribution of Titan's craters suggests extensive wetlands. *Icarus* 228:27–34. <https://doi.org/10.1016/j.icarus.2013.09.024>
- Neish CD, Carter LM (2014) Planetary Radar. In: *Encyclopedia of the Solar System*. Elsevier, pp 1133–1159. <https://doi.org/10.1016/B978-0-12-415845-0.00053-0>
- Neish CD, Molaro JL, Lora JM, et al (2016) Fluvial erosion as a mechanism for crater modification on Titan. *Icarus* 270:114–129. <https://doi.org/10.1016/J.ICARUS.2015.07.022>
- Nixon CA, Temelso B, Vinatier S, et al (2012) Isotopic Ratios in Titan's Methane: Measurements and Modeling. *Astrophys J* 749:159. <https://doi.org/10.1088/0004-637X/749/2/159>
- Osinski GR, Pierazzo E (2012) Impact Cratering: Processes and Products. In: *Impact Cratering: Processes and Products*. Wiley-Blackwell pp 1–20 <https://doi.org/10.1002/9781118447307.ch1>

- Osinski GR, Grieve RAF (2019) Impact Earth: A New Resource for Outreach, Teaching, and Research. *Elements* p 15:70–71. <https://doi.org/10.2138/gselements.15.1.70>
- Osinski GR, Grieve RAF, Ferrière L, et al (2022) Impact Earth: A review of the terrestrial impact record. *Earth-Science Rev* 232:104112. <https://doi.org/10.1016/J.EARSCIREV.2022.104112>
- Poag CW, Powars DSP, Poppe LJ, Mixon RB (1994) Meteoroid mayhem in Ole Virginny: Source of the North American tektite strewn field. *Geology* 22:691–694
- Robbins SJ (2018) A New Global Database of Lunar Impact Craters > 1 – 2 km : 1. Crater Locations and Sizes, Comparisons with Published Databases, and Global Analysis *Journal of Geophysical Research: Planets*. *J Geophys Res Planets* 871–892. <https://doi.org/10.1029/2018JE005592>
- Robbins SJ, Antonenko I, Kirchoff MR, et al (2014) The variability of crater identification among expert and community crater analysts. *Icarus* 234:109–131. <https://doi.org/10.1016/J.ICARUS.2014.02.022>
- Rodionova ZF, Shevchenko VV, Karlov AA, et al (1987) The Density Distribution of Lunar Craters of Different Degrees of Rim Sharpness and Completeness. In: 18th Lunar and Planetary Science Conference p 846
- Rosenqvist A, Shimada M, Member S, et al (2007) ALOS PALSAR : A Pathfinder Mission for Global-Scale Monitoring of the Environment. *IEEE Trans Geosci Remote Sens* 45:3307–3316
- Schurmeier LR, Dombard AJ (2018) Crater relaxation on Titan aided by low thermal conductivity sand infill. *Icarus* 305:314–323. <https://doi.org/10.1016/J.ICARUS.2017.10.034>
- Schurmeier LR, Brouwer G, Fagents S, et al (2023) Crater relaxation caused by an insulating methane clathrate crust on Titan. In: 54th Lunar and Planetary Science Conference p 2813



- Smith SK, Grieve RAF, Harris JR, et al. (1999) The Utilization of RADARSAT-1 Imagery for the Characterization of Terrestrial Impact Landforms. *Canadian J of Remote Sens* 25:218–228. <https://doi.org/10.1080/07038992.1999.10874721>
- Stephan K, Jaumann R, Karkoschka E, et al (2009) Mapping products of Titan's surface. In: *Titan from Cassini-Huygens*. Springer, pp 489–510. [https://doi.org/10.1007/978-1-4020-9215-2\\_19](https://doi.org/10.1007/978-1-4020-9215-2_19)
- Tobie G, Lunine JJ, Sotin C (2006) Episodic outgassing as the origin of atmospheric methane on Titan. *Nature* 440:61–64. <https://doi.org/10.1038/nature04497>
- Tokano T, McKay CP, Neubauer FM, et al (2006) Methane drizzle on Titan. *Nature* 442:432–435. <https://doi.org/10.1038/nature04948>
- Turtle, EP, Pierazzo, E, Collins, GS, et al (2005) Impact structures: What does crater diameter mean? *Large meteorite impacts III*, 384, pp.1-24.
- Turtle EP, Trainer MG, Barnes JW, et al (2020) Dragonfly: In Situ Exploration of Titan's Organic Chemistry and Habitability. In: *51st Lunar and Planetary Science Conference*. p 2288
- Wakita S, Johnson BC, Soderblom JM, et al (2022) Methane-saturated Layers Limit the Observability of Impact Craters on Titan. *Planet Sci J* 3:50. <https://doi.org/10.3847/psj/ac4e91>
- Wood CA, Lorenz R, Kirk R, et al (2010) Impact craters on Titan. *Icarus* 206:334–344. <https://doi.org/https://doi.org/10.1016/j.icarus.2009.08.021>
- Zink M, Krieger G, Fiedler H, Moreira A (2007) The TanDEM-X Mission: Overview and Status. In: *IEEE International Geoscience and Remote Sensing Symposium*. pp 3944–3947

## Chapter 3

### 3 The Effect of the Crustal Thermal Gradient on Fresh Crater Morphometries on Titan

Titan, the largest moon of Saturn, stands out as the only planetary body in our solar system, aside from Earth, with stable liquids on its surface and a thick, nitrogen-rich atmosphere. NASA's Cassini mission detected an unusually low number of impact craters on Titan's surface, primarily attributed to degradation and burial by fluvial erosion and aeolian infilling. Because the rates of these crater degradation processes and the ages of Titan's craters are unknown, the 'uneroded' morphometry of Titan's impact craters is not well understood. Knowing the morphometries of fresh craters would allow us to break this degeneracy and constrain the amount of erosion that has occurred on Titan. A comparison of Titan and Ganymede crater depths reveals that Titan's craters are hundreds of metres shallower. However, Titan and Ganymede differ in surface compositions (methane clathrate vs. water ice) and interior thermal structures, which may influence the cratering process. Numerical investigations that use Titan's unique interior properties can provide an improved understanding of fresh crater morphometries on Titan. In this work, we employ the iSALE shock physics code to simulate crater formation on Titan. The simulations explore the effect of thermal gradient in the ice crust on crater depths across a range of diameters. With a fixed impact velocity of 11 km/s, we vary impactor diameters from 2 to 10 km. The lower thermal conductivity of methane clathrate results in a higher thermal gradient; we thus consider thermal gradients from 3 K/km (pure water ice case) to 10 K/km (methane clathrate layer case). By comparing the depths of fresh Titan impact craters inferred from the model outputs to observed crater depths on Titan, we aim to determine the extent of erosion that has occurred since their emplacement. Our findings suggest that an upper limit of  $<1.6 \times 10^{-6}$  m/yr on the fluvial erosion rate can account for the erosion observed at Titan's craters over the age of its atmosphere (500 Myr).

### 3.1 Introduction

Titan is the largest moon of Saturn, and the second largest in the solar system. It is an icy world thought to have a ~100 km thick ice crust overlaying a liquid water ocean (Mitri and Showman, 2008; Nimmo and Bills, 2010; Collins and Johnson, 2014). It has a thick, nitrogen-rich atmosphere, with a few percent methane (Lindal et al., 1983; Tomasko et al., 2005; Coustenis, 2014; Hörst, 2017), which supports an active hydrological cycle similar to Earth with methane as the working fluid (e.g. Atreya et al., 2006; Tokano et al., 2006; Lunine and Atreya, 2008; Hayes et al., 2018). This complex climate system creates surface features such as sand dunes, methane river networks, as well as lakes and seas (Lunine and Atreya, 2008; Lopes et al., 2020), which gives rise to active geological surface processes such as erosion and weathering.

The evidence of surface modification on Titan is clearly seen in its impact craters. The morphology and morphometry of Titan's craters point to modification by aeolian and fluvial erosion (Neish et al., 2013, 2016; Hedgepeth et al., 2020). Cassini's RADAR instrument shows sediments infilling crater centers and river channels cutting through crater rims (Soderblom et al., 2010; Neish et al., 2015). Moreover, Cassini's topography data revealed that craters on Titan are hundreds of meters shallower in depth compared to similarly sized craters on other icy satellites, such as Ganymede (Neish et al., 2013; Hedgepeth et al., 2020). In addition, the number of possible impact craters on Titan as seen by Cassini is remarkably low compared to the other Saturnian satellites (Lorenz et al., 2007; Hedgepeth et al., 2020). The low crater count on Titan may be a result of several factors including (1) disruption of small impactors in its atmosphere, (2) erosion and burial of craters by active geologic process, (3) impacts into marine environments, and (4) perhaps a rapid resurfacing mechanism on Titan in the recent past (Neish and Lorenz, 2014). However, the rates of crater degradation processes and the ages of Titan's craters are unknown (Neish et al., 2013, 2016), and thus the 'uneroded' morphology of Titan's impact craters is not well understood. Knowing the morphologies of fresh craters would allow us to break this degeneracy and constrain the amount of erosion that has occurred on Titan.

Previous studies have used Ganymede, an airless icy satellite, as a reference for what Titan's craters would look like in the absence of exogenic processes modifying them. This is a good approximation as Ganymede and Titan are similar in size and density (Buratti and Thomas, 2014). They also share a similar overall structure with a thick ice crust overlying a liquid water ocean and possibly a deeper high pressure ice layer (Collins and Johnson, 2014; Mitri and Showman, 2008; Nimmo and Bills, 2010). Under these assumptions, Titan crater depths are hundreds of meters shallower compared to the depths of fresh craters on Ganymede. This serves as a first-order constraint on the level of erosion that has occurred on Titan. However, we cannot directly use Ganymede as an analogue for fresh/uneroded craters on Titan given the differences in the surface composition and interior thermal structure of the two satellites.

For example, Ganymede has a mostly pure water-ice surface whereas Titan likely has a methane-saturated water-ice layer (Sotin et al., 2009) or a methane clathrate layer (Choukroun et al., 2010) overlying a water-ice basement. Methane clathrate hydrate remains stable under Titan's current surface temperature and pressure conditions, and may form a significant portion of Titan's upper crust (Choukroun et al., 2010; Vu et al., 2020). Due to higher strength of the methane clathrate compared to water ice (Durham et al., 2003), the presence of methane clathrate in the target material may have a significant influence on the formation of impact craters on Titan. More specifically, Wakita et al. (2022) showed that an impact into a methane clathrate target forms slightly smaller craters compared to a pure water-ice target, for a given impactor size (also suggested in Wünnemann et al., 2011).

The presence of methane clathrates also affects the target temperature at depth. Methane clathrate exhibits a lower thermal conductivity ( $0.5 \text{ W m}^{-1} \text{ K}^{-1}$ ) compared to water ice ( $2.2 \text{ W m}^{-1} \text{ K}^{-1}$ ) at 263 K (Sloan et al., 2007). Consequently, when methane clathrate is present in the crust, it leads to higher lithospheric thermal gradients compared to crusts composed solely of water ice with the same heat flow (Kalousová and Sotin, 2020). At these higher temperatures, the target material weakens, eventually losing its strength as the temperature approaches the melting point. As a result, the vertical temperature profile of the target plays a crucial role in crater formation and the resulting

morphology and morphometry (Bray et al., 2014; Silber and Johnson, 2017; Bjonnes et al., 2022).

Since previous studies on this topic have been limited to water-ice target materials, numerical models that incorporate methane clathrate conditions and associated thermal properties would allow for an improved understanding of crater morphologies and morphometries observed on Titan. A more recent study incorporating methane clathrate strength parameters (but not its thermal properties) investigated the effect of methane clathrate and methane saturation on crater formation on Titan (Wakita et al., 2022). Following that, Wakita et al., 2023 explored the effect of methane clathrate's temperature profile on the formation of Selk crater (80 km in diameter), one of the largest and freshest craters on Titan (Neish et al., 2018).

In this work, following Wakita et al. (2023), we further explore how the lithospheric thermal gradient influences crater formation and morphometry across various crater sizes observed on Titan. To isolate the influence of the thermal gradient, we consider gradients representative of methane clathrate, while keeping the target composition and strength to that of pure water-ice. We then compare the depths of fresh Titan impact craters inferred from the model outputs to observed crater depths on Titan. This allows us to place improved constraints on the extent of erosion and/or modification that has occurred since the craters' emplacement.

## 3.2 Methods

In this study we investigated the influence of the thermal gradient in Titan's ice shell on the resulting crater morphometries using numerical modelling. We simulated the formation of impact craters on Titan using iSALE-2D, a multimaterial, multirheology shock physics code (Collins et al., 2004; Ivanov et al., 1997; Melosh et al., 1992; Wünnemann et al., 2006; Collins et al., 2016). This is an extension of the SALE hydrocode (Amsden et al., 1980), which was developed to model planetary impact cratering. In our simulations, the impactor is assumed to be comet-like, composed entirely of water-ice. Titan impactors are mainly Centaurs (Zahnle et al., 2003), with a density of  $500 \text{ kg/m}^3$  (e.g., Richardson et al., 2007; Sierks et al., 2015) and an average impactor velocity of 11

km/s (Zahnle et al., 2003; Bell, 2020; Nesvorny et al., 2023). The impact cratering process on Titan is also influenced by atmospheric shielding. Titan's extensive and dense atmosphere decelerates and breaks up small impactors ( $D < 1$  km), but causes only slight disruption to impactors larger than 2 km in diameter (Artemieva and Lunine, 2003). Therefore, for our study, we consider impactor diameters of 2, 4, 5, 8, and 10 km. We chose a spatial resolution of 100, 125, and 250 m for the impactors of sizes 2, 4, and  $\geq 5$  km, respectively. In all these setups, the grid resolution was set to at least 10 cells per projectile radius (CPPR) in order to resolve the morphometry of the resulting crater while balancing computational time requirements (Wünnemann et al., 2006, 2008; Pierazzo et al., 2008; Elbeshhausen et al., 2009; Silber and Johnson, 2017). Due to the axial symmetry of the models (common for impact studies), we only considered vertical impacts ( $90^\circ$ ). However, we note that most impacts are oblique and occur at an average angle of  $45^\circ$  (Gilbert, 1893; Shoemaker, 1962).

The impact target surface is simplified to be a pure water-ice shell overlying a subsurface water ocean. The ice crust is represented by the Tillotson equation of state (Tillotson, 1962; Ivanov et al., 2002; Turtle and Pierazzo, 2001) and its thickness is varied from 50-150 km (Tobie et al., 2006; Nimmo and Bills, 2010; Béghin et al., 2012; Hemingway et al., 2013; Mitri et al., 2014) to test its influence on the resulting crater. The water ocean layer is represented by the Analytic Equation of State (ANEOS) for water (Thompson and Lauson, 1974; Turtle and Pierazzo, 2001). **Table 2** lists a summary of the material input parameters. To represent Titan's interior structure, we assumed a conductive lid on top of a convective ice layer (Mitri and Showman, 2005; 2008; McKinnon, 2006; Tobie et al., 2006). The thickness of this conductive lid depends on 1) the surface temperature fixed at 94 K (Lindal et al., 1983; Fulchignoni et al. 2005; Schinder et al., 2011), 2) the temperature of the convective ice set to 255 K (Kalousová and Sotin, 2020), and 3) the thermal gradient of the ice crust (varied from 3-10 K/km). A thermal gradient of 3 K/km is representative of a pure water-ice scenario (Wakita et al., 2022), whereas the higher thermal gradients (5 and 10 K/km) are more representative of methane clathrate presence in Titan's ice crust (Kalousová and Sotin, 2020). Note that we simulated thermal gradients representative of methane clathrate; we did not implement any other material parameters representing methane clathrates. Previous studies by Wakita et al. (2022, 2023)

considered the effects of methane clathrate. This study focuses on studying the effect of the thermal gradient as a follow-up. The lithospheric thermal gradients of 3, 5, and 10 K/km correspond to approximate conductive lid thicknesses of 54, 32, and 16 km, respectively. **Figure 3.1** illustrates a schematic showing the relative change in the lid thickness as the thermal gradient increases.

To analyze the resulting crater morphometries, we measured the rim to rim crater diameter and crater depths from the highest point on the rim to the lowest point on the crater floor. For impact simulations, uncertainties are commonly assumed to be two to three cells (Silber and Johnson, 2017). In our work, we take three grid cells in each direction as a conservative approach for uncertainty in crater diameter and depth.

**Table 2: Summary of input parameters (Bray et al., 2014 and references therein)**

<b>Description</b>	<b>Water Ice</b>	<b>Water Ocean</b>
EOS	Tillotson	ANEOS
Thermal softening parameter	1.2 <sup>b</sup>	None
Cohesion, intact (MPa)	10 <sup>a</sup>	XXX
Cohesion, damaged (MPa)	0.01	XXX
Frictional coefficient, intact	2.0 <sup>a</sup>	XXX
Frictional coefficient, damaged	0.6 <sup>c</sup>	XXX
Limiting strength, intact (GPa)	0.11 <sup>a</sup>	XXX
Limiting strength, damaged (GPa)	0.11 <sup>a</sup>	XXX

<sup>a</sup>Intact ice values from Durham et al. (1983)

<sup>b</sup>Derived by applying an Ohnaka (1995) style trend to data from Durham et al. (1983).

<sup>c</sup>Frictional coefficient, damaged from Bray (2008)

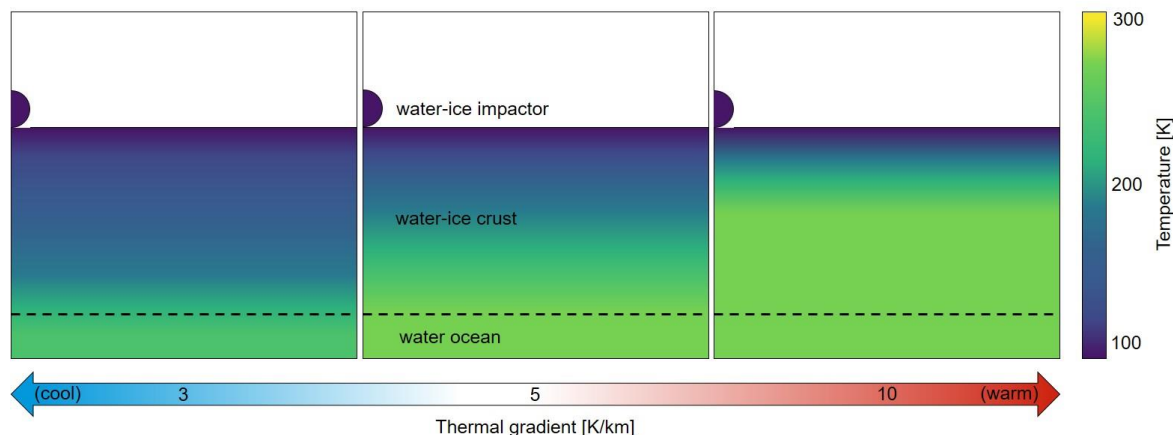


**Figure 3.1: Schematic of the model setup depicting how the thermal gradient of the ice crust affects the interior structure. Increasing thermal gradient (from left to right) of the ice crust brings warm material closer to the surface (Kalousová and Sotin, 2020). The 10 K/km case is representative of thermal properties in the presence of methane clathrates. The black dashed line represents the material boundary between the ice crust and the ocean (which varies from 50 to 150 km in depth for our models).**

### 3.3 Results

#### 3.3.1 Effect of Thermal Gradient

We examine the sensitivity of the thermal gradient on the resulting crater morphometries by varying its value from 3 K/km (water-ice representative) to 10 K/km (methane clathrate representative). We fix the ice shell thickness to 50 km and vertical impact velocity to 11 km/s. We vary the impactor diameters from 2-10 km to reproduce the variety of crater sizes observed on Titan. We used 2 km as the lower bound due to atmospheric shielding effects on smaller impactors.

In Figure 3.2, we illustrate the time series of crater formation for a 5 km diameter impactor with a temperature gradient of 5 K/km. Seconds after impact, a transient cavity/crater forms, followed by its collapse, resulting in the formation of a central uplift. As this uplift collapses, it forces warm material to flow over the crater rim. This overflow is observed in simulation studies of other icy moons with higher thermal gradients such as Europa (Silber and Johnson, 2017). Thus, the visible rim after crater formation is complete



is not truly representative of the true crater rim. The effect of the overflow is also likely exaggerated by the axisymmetric setup of iSALE. As such, we extract the crater rim measurement at a timestep between the collapse of the transient cavity and the collapse of the central uplift.

In **Figure 3.3/Table 3**, it is evident that, for a given impactor size, a higher thermal gradient produces a crater that is wider (in diameter) and shallower (in depth) compared to the cold case thermal gradient (3 K/km, representative of water ice). This aligns well with results from previous studies that have investigated the effect of the thermal gradient in the ice crust (e.g. Schenk, 2002; Bray et al., 2014; Silber and Johnson, 2017; Bjonnes et al., 2022; Wakita et al., 2022, 2023). Except in the case of a small impactor ( $d_{\text{imp}} = 2$  km), the resulting crater depths overlap for all three thermal gradient regimes. This is likely because a small impactor does not open up a transient cavity large enough to experience the effects of the warmer ice. The influence of the warmer thermal gradient becomes notably pronounced for larger impactors. For example, a 4 km impactor generates a crater that is several kilometers deeper under the coldest thermal gradient (3 K/km) compared to the warmest thermal gradient (10 K/km) (refer to **Table 3**). This discrepancy is likely due to the increased mobility of warm ice, allowing the water-ice boundary to move upwards, a phenomenon most noticeable in the case of a 10 km impactor, as illustrated in **Figure 3.4**. However, this effect becomes less pronounced as the ice thickness increases to 100 km. The 10 km diameter impactor creates a transient cavity large enough to disrupt the ice-water boundary at 50 km depth.

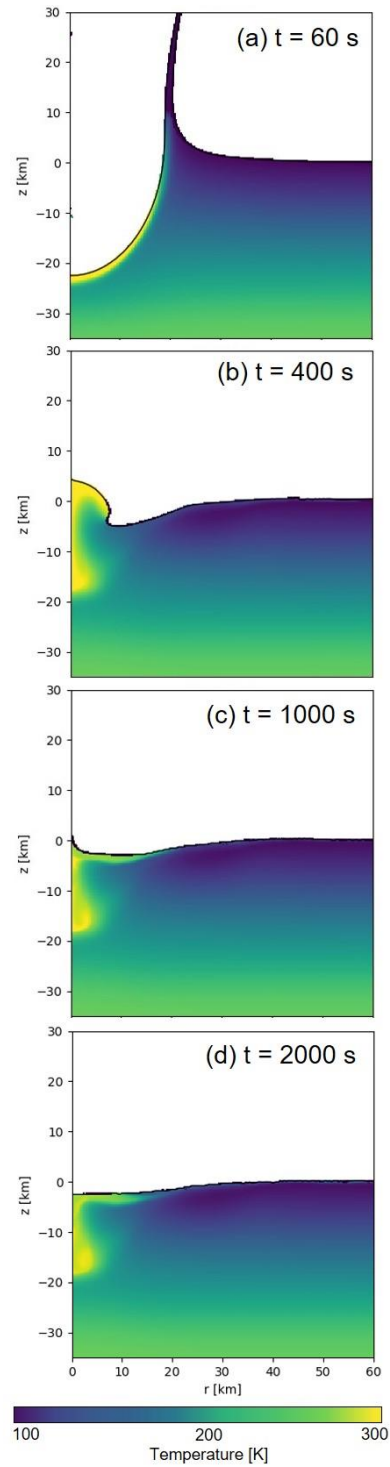


**Figure 3.2: Time series of crater formation for a 5 km diameter impactor hitting an ice crust with thickness of 50 km and thermal gradient of 5 K/km. Colour indicates the temperature in Kelvin.**

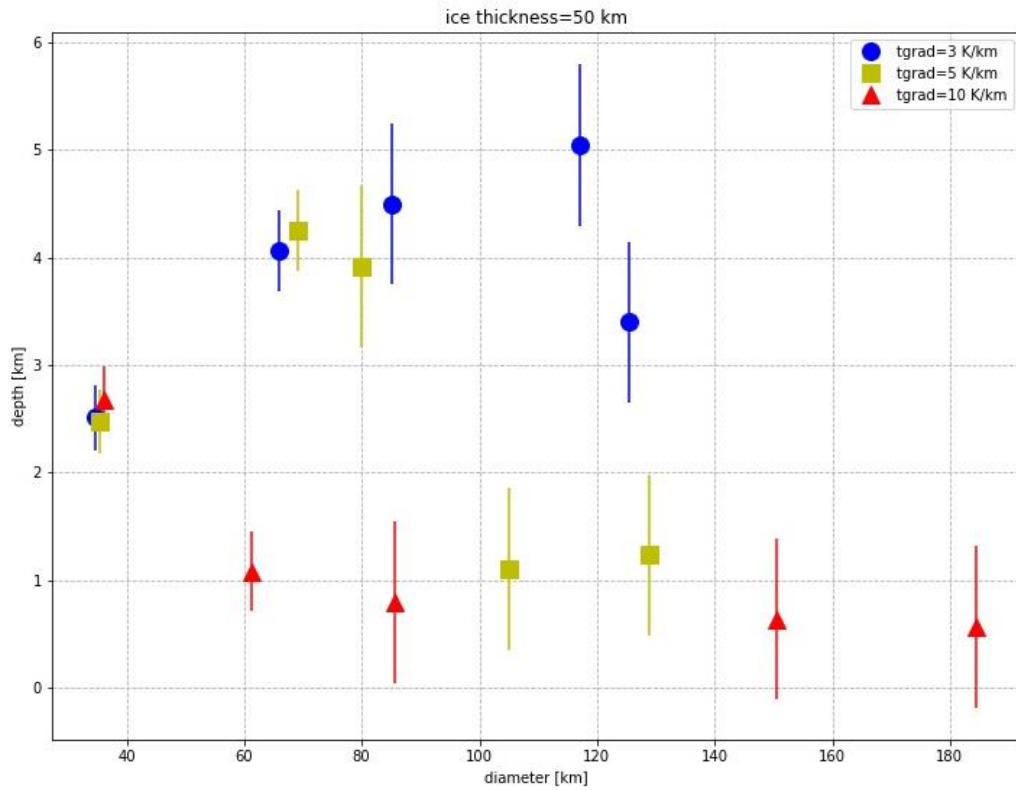


**Figure 3.3: Crater diameters and depths for varying thermal gradients. The blue circles represent a thermal gradient of 3 K/km, yellow squares a gradient of 5 K/km, and red triangles a gradient of 10 K/km.**

**Table 3: Crater diameters and depths. Impact velocity fixed at 11 km/s and convective temperature is set to 255 K.**

Impactor Diameter (km)	Thermal Gradient (K/km)	Crater Diameter (km)	Crater Depth (km)	Error ( $\pm$ km)
2	3	34.8	2.51	0.60
	5	35.4	2.47	
	10	36.2	2.68	
4	3	66.0	4.06	0.75
	5	69.0	4.25	
	10	61.2	1.08	
5	3	85.0	4.50	1.5
	5	80.0	3.91	
	10	85.5	0.80	
8	3	117.0	5.05	
	5	105.0	1.11	
	10	150.5	0.64	
10	3	125.5	3.40	
	5	129.0	1.23	
	10	184.5	0.56	

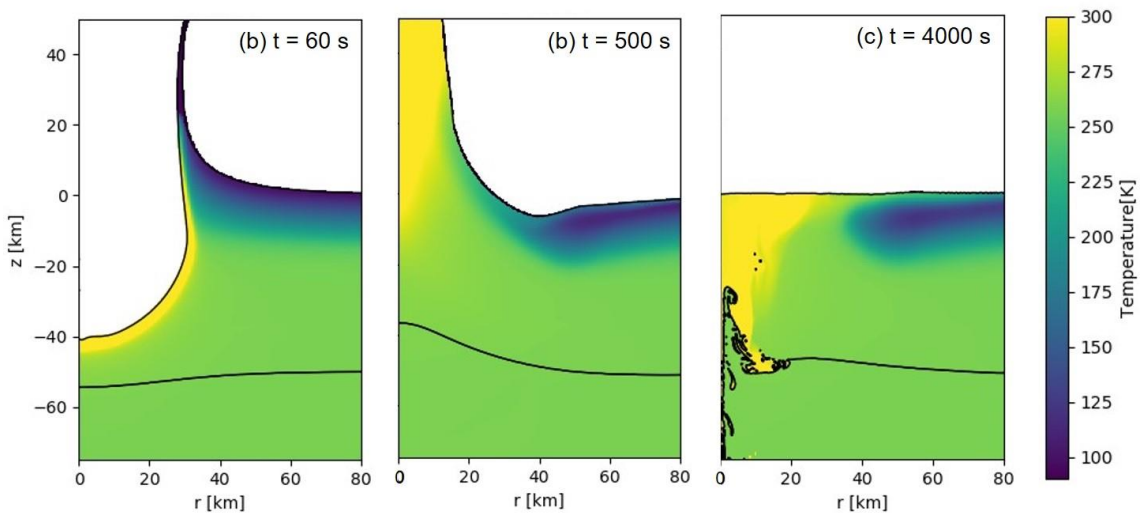


**Figure 3.4: Time series of crater formation for a 10 km diameter impactor hitting an ice crust with thickness of 50 km and thermal gradient of 10 K/km. Colour indicates the temperature in Kelvin and the solid black line represents the material boundary between the ice crust and the water ocean.**

### 3.3.2 Effect of Ice Thickness

Even though the thermal gradient of the ice shell is an important factor affecting crater morphometries, other properties (e.g. ice shell thickness, impactor velocity, target composition, gravity) also play a role. Here, we investigated the influence of the ice shell thickness on crater morphometry. To examine its effect, we vary the thickness of the ice shell from 50 to 150 km (Tobie et al., 2006; Nimmo and Bills, 2010; Béghin et al., 2012; Hemingway et al., 2013; Mitri et al., 2014), while setting the thermal gradient to 3 K/km. **Figure 3.5** shows that the crater depths are relatively consistent (within error) for a given impactor size as the ice shell thickness increases. However, we see that crater diameter increases with increasing ice shell thickness, for larger impactors ( $d_{\text{imp}} = 5$  km).

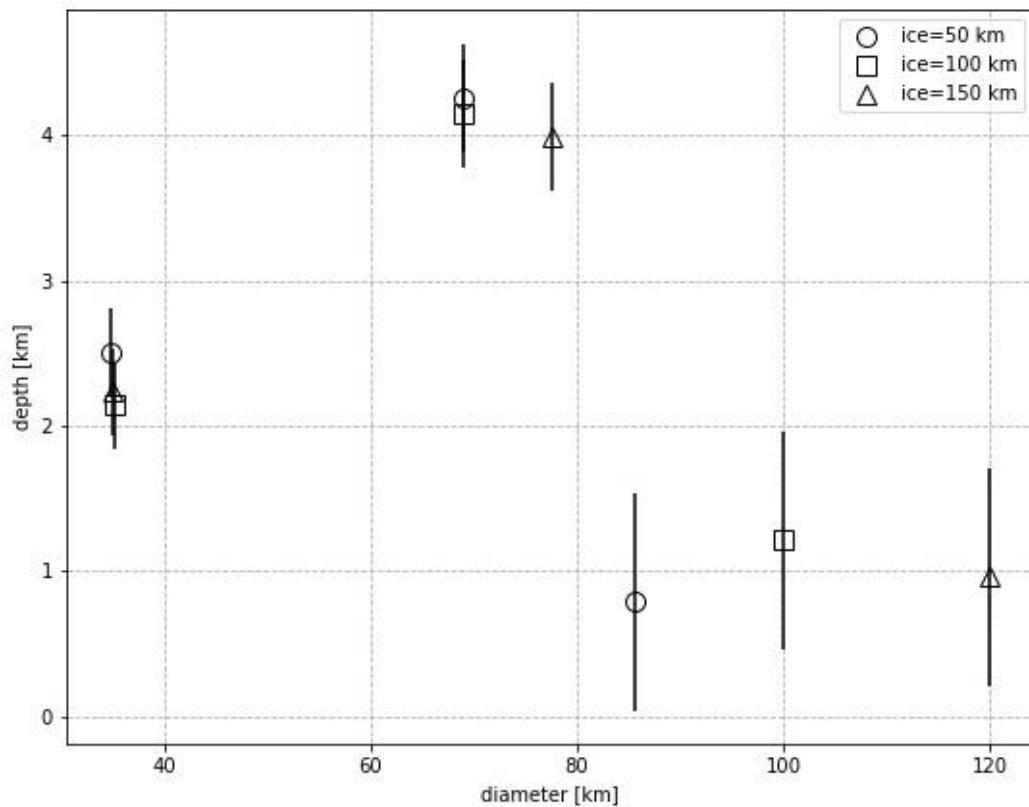


**Figure 3.5: Crater diameters and depths for varying ice shell thickness. The thickness is represented by the marker shape (circle = 50 km, square = 100 km, triangle = 150 km). The thermal gradient is set to 3 K/km and the impactor size is varied from 2 to 5 km.**

### 3.3.3 Effect of Impact Velocity

For our simulations, we fixed the impact velocity at the average for Titan (11 km/s). However, we also conducted simulations to determine the influence of this parameter on crater depth and diameter. We find that a 2 km impactor with velocity of 11 km/s (thermal gradient and ice thickness fixed at 3 K/km and 100 km, respectively) produces a crater that is  $35.2 \pm 0.3$  km wide and  $2.12 \pm 0.3$  km deep. In contrast, when the impactor's velocity is increased to 15 km/s, the resulting crater widens to around  $40.5 \pm 0.3$  km while maintaining a depth of  $2.16 \pm 0.3$  km. This is likely because an impactor travelling at a higher velocity will have more kinetic energy, which will produce a larger transient cavity. This stems from crater dimension scaling laws (e.g. Holsapple and Schmidt, 1982; Melosh, 1989; Holsapple, 1993). Nonetheless, the impactor velocity has a smaller influence on crater depth (the focus of this work) compared to the lithospheric thermal gradient.

## 3.4 Discussion

Our results indicate that the thermal gradient of the ice shell has a significant influence on crater depth compared to other parameters like the ice shell thickness or the impactor velocity. Delving deeper into the effect of the thermal gradient, we observe that a higher thermal gradient produces wider and shallower craters compared to a lower thermal gradient. The higher gradient is representative of methane clathrates, expected to be present at Titan's surface.

### 3.4.1 Constraints on Erosion

The modelling effort in this study is motivated by the low crater count on Titan, which is likely affected by the erosional processes present at Titan's surface. The rates of crater degradation on Titan are poorly constrained (e.g., Maue et al., 2022), which makes placing constraints on erosion difficult (Neish et al., 2016). To constrain erosion rates, we need model outputs that incorporate Titan conditions (i.e. methane clathrate) representative of 'fresh' or 'uneroded' crater morphologies on Titan. We use impact craters, because they are one of the few geologic features that have relatively well-known initial shapes and sizes (unlike, for example, mountains). In our work, we simulated crater formation for sizes

observed on Titan using a range of thermal gradients in the ice shell. We then compared this to crater depths measured by Hedgepeth et al. (2020) using Cassini data (**Figure 3.6**).

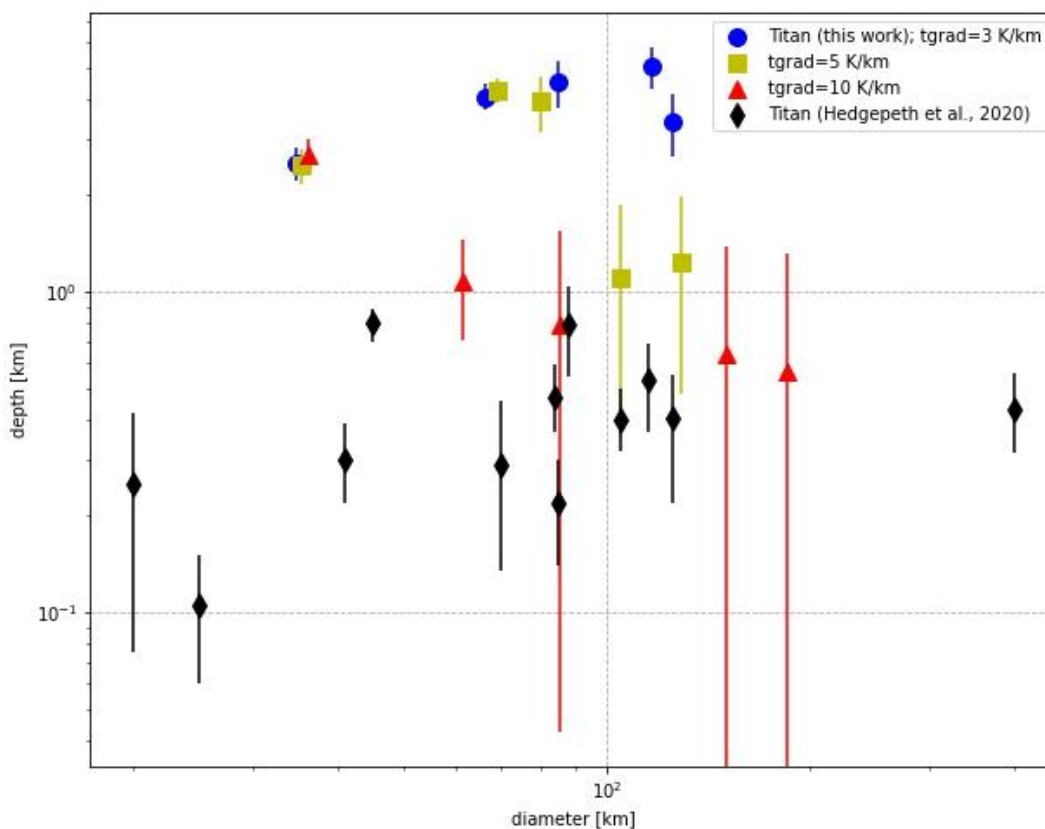


**Figure 3.6: Model output depths of ‘fresh’ craters compared to observed depths on Titan with Cassini data from Hedgepeth et al. (2020). The blue circles represent a thermal gradient of 3 K/km, yellow squares a gradient of 5 K/km, and red triangles a gradient of 10 K/km. The black diamonds represent Cassini observed crater depths.**

We find that a ‘cold’ thermal gradient (3 K/km) produces craters up to 4 km deep. This would imply kilometers of erosion over Titan's lifetime, a conclusion that appears inconsistent with previous studies investigating erosion on Titan (Black et al., 2012; Neish et al., 2016). Black et al. (2012) analyzed the shape of Titan’s drainage networks to quantify erosional exhumation. They developed a method to assess the extent of erosion in a fluvial setting, relying only on features measurable in plan view. The findings of their work suggest maximum erosion on the order of 100 m over  $10^8$  years, aligning with crater counting-derived surface ages for Titan ranging from  $10^8$  to  $10^9$  years (Lorenz et al., 2007;

Wood et al., 2010; Neish and Lorenz, 2012; Hedgepeth et al., 2020). Considering this limit, the depths produced in a cold thermal gradient case, indicating kilometers of erosion, seem implausible.

We can estimate erosion rates on Titan using the observed depths from our models, and an estimate for the age of Titan's methane-rich atmosphere (**Table 4**). Without such an atmosphere, fluvial erosion rates on Titan would be negligible in comparison (Charnay et al., 2014). Reasonable estimates for the age of Titan's methane-rich atmosphere are somewhere on the order of  $10^8$  years (Hörst, 2017). As an illustrative example, we consider a 5 km diameter impactor striking a 50 km thick ice shell, resulting in an approximately 80 km wide crater. We erode the entire crater as this would help to place an upper limit to the erosion rate. We calculate possible erosion rates over the age of Titan's atmosphere (500 Myr), cratering counting inferred surface age (250 Myr), and the age of the solar system (4.5 Gyr). This yields an average erosion rate on the order of  $10^{-7}$  to  $10^{-5}$  m/yr. In contrast, typical fluvial erosion rates on Earth range from  $\sim 10^{-5}$  to  $10^{-3}$  m/yr (Portenga and Bierman, 2011). Initially, Collins (2005) proposed that the erosion rates on Earth and Titan would be comparable. This is based on the fact that the lower abrasion resistance parameter of water ice at Titan surface temperatures is balanced with the lower kinetic energy of saltating grains on Titan. However, recent experimental work by Collins et al. (2012) suggests that ice on Titan may exhibit strength similar to quartzite or welded tuff, some of the strongest terrestrial materials (Sklar and Dietrich, 2001). This implies that river incision, and consequently, fluvial erosion, could be slower on Titan than Earth, assuming similar discharge rates. However, these discharge rates and frequency of high flow events on Titan may differ from those on Earth. Considering some physical parameters affecting fluvial incision on Earth and Titan vary by orders of magnitudes, overall, erosion rates on both planets are likely comparable. Based on average fluvial erosion rates on Earth, the estimated erosion rates from this work are 10 to  $10^{-4}$  times below that limit.



**Table 4: Possible erosional rates [m/yr] for a ~80 km crater in different thermal gradients.**

Thermal gradient [K/km]	Crater depth [km]	Erosional rates over a time period [m/yr]		
		500 Myr	250 Myr	4.5 Gyr
3	4.50	$9 \times 10^{-6}$	$1.8 \times 10^{-5}$	$1 \times 10^{-6}$
5	3.91	$7.8 \times 10^{-6}$	$1.6 \times 10^{-5}$	$8.7 \times 10^{-7}$
10	0.80	$1.6 \times 10^{-6}$	$3.2 \times 10^{-6}$	$1.8 \times 10^{-7}$

However, we acknowledge that erosion of kilometers of ice as would be inferred from the cold (3 K/km) thermal gradient is highly unlikely. Upon comparing our modeled depths to Cassini observed depths (**Figure 3.6**), we observe that craters impacting into an ice crust with a higher thermal gradient (10 K/km) produce depths more comparable to those of some of the freshest craters on Titan (Neish et al., 2018, Hedgepeth et al., 2020). Thus, eroding an 800 m deep crater to 0 m, the resulting erosion rate would be approximately  $1.6 \times 10^{-6}$  m/yr, assuming this level of erosion has occurred over the age of Titan’s atmosphere (**Table 4**). However, since craters are still preserved and observed on Titan, the erosional rate would have to be  $<1.6 \times 10^{-6}$  m/yr. We note this is likely a lower limit on the overall erosion rate, as this calculation only accounts for fluvial erosion. From Cassini observations, we recognize that aeolian infilling also plays a role in shallowing craters (Neish et al., 2013). However, this remains a very approximate constraint on erosion rate overall, as factors other than erosion likely contribute to the shallowing of craters on Titan.

### 3.4.2 Other Factors that Shallow Craters on Titan

Although our models show that a lithospheric thermal gradient plays a significant role in crater morphometry, especially in terms of crater depth, there are other factors on Titan that may influence the size and shape of a crater. Firstly, the higher strength of the methane clathrate (compared to water-ice) produces smaller and shallower craters for a given impactor (Wakita et al., 2022). For instance, according to Wakita et al. (2022), a 5 km diameter impactor colliding with a surface containing water-ice (without a clathrate layer) creates a crater approximately 80 km wide and 3.5 km deep. In contrast, when the same-sized impactor hits a surface with a 1 km thick clathrate layer, the resulting crater measures approximately 42 km in width and 2 km in depth. This represents roughly half

the diameter and slightly more than half the depth compared to the scenario without a clathrate layer. Methane saturation in the ice crust of Titan may also result in shallower craters, as low-strength, saturated regolith slumps back into the crater cavity shortly after formation. For some such cases, craters exhibit minimal to no topography (Wakita et al., 2022).

We note that viscous relaxation may also play a role in the shallowing of craters (Bland et al., 2017; Dombard and McKinnon, 2000, 2006; Schurmeier and Dombard, 2018; Schurmeier et al., 2023; Bland and Bray, 2023). The presence of a methane clathrate layer in the ice shell promotes ductile deformation and results in topographic relaxation, compared to an icy shell only composed of water ice. Topographic relaxation due to the insulating effect of a clathrate crust may be enough to reproduce the relative depths of some craters on Titan (e.g. Selk, Sinlap) without requiring fluvial erosion or sand fill (Schurmeier et al., 2023).

There are multiple factors contributing to the crater morphologies observed on Titan. Therefore, firm constraints on erosional rates cannot be established without considering all the influencing factors collectively. For example, viscous relaxation operates on more quickly on longer wavelengths, causing large crater interiors to shallow faster than their narrow rims. In contrast, fluvial erosion tends to erase the rim faster than it fills in the crater. Distinguishing the contribution of each process to the resulting crater morphologies and morphometries would be possible with improved data. The upcoming Dragonfly mission to Titan (e.g. Turtle et al., 2020; Turtle and Lorenz, 2021), set to explore Selk crater (Barnes et al., 2021), will help us to better characterize the morphology and morphometry of Titan craters and improve our understanding of the impact cratering process there.

### 3.4.3 iSALE Limitations

We note that iSALE is not suitable for studying post-impact relaxation or minor deformations over extended periods (i.e. after crater collapse). Longer run times can result in reflections from the shockwave and numerical diffusion. This combination may result in inaccurate, non-real shallowing of craters. Thus, deciding simulation durations and the

time of crater metric measurements is critical. For depth measurements, we qualitatively assess when all motion and temperature changes stop from the time series. We check that no notable change occurs in the depth in the following time frames before taking the measurement (Silber and Johnson, 2017; Wakita et al., 2022).

### 3.5 Conclusions

In this work, we use iSALE to simulate the formation of impact craters on Titan, incorporating the thermal properties of methane clathrates expected to be stable on its surface. This is motivated by the need for a more comprehensive understanding of the uneroded morphology and morphometry of craters on Titan. The initial morphometries are needed to constrain the amount of erosion that may have occurred there. Cassini observations provide evidence of crater modification due to erosional processes, with the observed depths of Titan craters appearing shallower than those of similarly sized craters on Ganymede. Our results reveal that a cold thermal gradient (3 K/km), equivalent to pure water-ice, implies kilometers of erosion, a finding inconsistent previous studies. However, when a higher thermal gradient (10 K/km) representative of methane clathrate is considered, our simulations produce crater depths aligning with those of the freshest craters observed on Titan. Using our modeled depths, we estimate a fluvial erosion rate of  $<1.6 \times 10^{-6}$  m/yr, accounting for approximately 800 m of erosion over the age of Titan's atmosphere. It is important to note, though, that this calculation does not incorporate the contribution of aeolian infilling or other factors influencing the shallowing of craters on Titan.

### 3.6 References

- Amsden AA, Ruppel HM, Hirt CW (1980) SALE: A Simplified ALE computer program for fluid flow at all speeds. Los Alamos National Lab Report LA-8095 101.  
<https://doi.org/10.2172/5176006>
- Artemieva N, Lunine J (2003) Cratering on Titan: impact melt, ejecta, and the fate of surface organics. *Icarus* 164:471–480.  
[https://doi.org/10.1016/S0019-1035\(03\)00148-9](https://doi.org/10.1016/S0019-1035(03)00148-9)
- Atreya SK, Adams EY., Niemann HB, et al (2006) Titan's methane cycle. *Planet Space Sci* 54:1177–1187. <https://doi.org/10.1016/J.PSS.2006.05.028>
- Béghin C, Randriamboarison O, Hamelin M, et al (2012) Analytic theory of Titan's Schumann resonance: Constraints on ionospheric conductivity and buried water ocean. *Icarus* 218:1028–1042. <https://doi.org/10.1016/J.ICARUS.2012.02.005>
- Bell SW (2020) Relative Crater Scaling Between the Major Moons of Saturn: Implications for Planetocentric Cratering and the Surface Age of Titan. *J Geophys Res Planets* 125:1–18. <https://doi.org/10.1029/2020JE006392>
- Bjonnes E, Johnson BC, Silber EA, et al (2022) Ice Shell Structure of Ganymede and Callisto Based on Impact Crater Morphology. *J Geophys Res Planets* 127:1–14.  
<https://doi.org/10.1029/2021JE007028>
- Black BA, Perron JT, Burr DM, Drummond SA (2012) Estimating erosional exhumation on Titan from drainage network morphology. *J Geophys Res* 117:E08006.  
<https://doi.org/10.1029/2012JE004085>
- Bland MT, Bray VJ (2023) Large Shallow Craters on Callisto and Ganymede as an Inevitable Result of Viscous Relaxation. In: *LPI Contributions*. p 2104
- Bland MT, Singer KN, McKinnon WB, Schenk PM (2017) Viscous relaxation of Ganymede's impact craters: Constraints on heat flux. *Icarus* 296:275–288.  
<https://doi.org/10.1016/J.ICARUS.2017.06.012>

- Bray VJ, Collins GS, Morgan JV, et al. (2008) The effect of target properties on crater morphology: Comparison of central peak craters on the Moon and Ganymede. *Meteorit Planet Sci* 43:1979-1992.  
<https://doi.org/10.1111/j.1945-5100.2008.tb00656.x>
- Bray VJ, Collins G., Morgan Jv, et al (2014). Hydrocode simulation of Ganymede and Europa cratering trends – How thick is Europa’s crust? *Icarus* 231:394–406.  
<https://doi.org/10.1016/J.ICARUS.2013.12.009>
- Buratti BJ, Thomas PC (2014) Planetary Satellites. *Encycl Sol Syst* 759–777.  
<https://doi.org/10.1016/B978-0-12-415845-0.00034-7>
- Charnay B, Forget F, Tobie G, et al (2014) Titan’s past and future: 3D modeling of a pure nitrogen atmosphere and geological implications. *Icarus* 241:269–279.  
<https://doi.org/https://doi.org/10.1016/j.icarus.2014.07.009>
- Choukroun M, Grasset O, Tobie G, Sotin C (2010) Stability of methane clathrate hydrates under pressure: Influence on outgassing processes of methane on Titan. *Icarus* 205:581–593. <https://doi.org/10.1016/J.ICARUS.2009.08.011>
- Collins GC (2005) Relative rates of fluvial bedrock incision on Titan and Earth. *Geophys Res Lett* 32:1–4. <https://doi.org/10.1029/2005GL024551>
- Collins GS, Elbenschhausen D, Wunnemann K, et al (2016) iSALE: A multi-material, multi-rheology shock physics code for simulating impact phenomena in two and three dimensions. iSALE-Dellen release.
- Collins GS, Johnson TV (2014) Ganymede and Callisto. In: *Encyclopedia of the Solar System*. Elsevier, pp. 813–829
- Collins GS, Melosh HJ, Ivanov BA (2004) Modeling damage and deformation in impact simulations. *Meteorit Planet Sci* 39:217–231.  
<https://doi.org/10.1111/j.1945-5100.2004.tb00337.x>

- Collins GC, Sklar LS, Litwin KL, Polito PJ (2012) Do Titan's river channels carve into ice bedrock or loose regolith? In: Titan Through Time; Unlocking Titan's Past, Present and Future p 30.
- Coustonis A (2014) Titan. In: Encyclopedia of the Solar System. Elsevier, pp. 883–905
- Dombard AJ, McKinnon WB (2000) Long-term retention of impact crater topography on Ganymede. *Geophys Res Lett* 27:3663–3666.  
<https://doi.org/10.1029/2000GL011695>
- Dombard AJ, McKinnon WB (2006) Elastoviscoplastic relaxation of impact crater topography with application to Ganymede and Callisto. *J Geophys Res Planets* 111:1–22. <https://doi.org/10.1029/2005JE002445>
- Durham WB, Heard HC, Kirby SH (1983) Experimental deformation of polycrystalline H<sub>2</sub>O ice at high pressure and low temperature: Preliminary results. *J Geophys Res* 88:B377–B392. <https://doi.org/10.1029/JB088iS01p0B377>
- Durham WB, Kirby SH, Stern LA, Zhang W (2003) The strength and rheology of methane clathrate hydrate. *J Geophys Res Solid Earth* 108:1–11.  
<https://doi.org/10.1029/2002jb001872>
- Elbeshhausen D, Wünnemann K, Collins GS (2009) Scaling of oblique impacts in frictional targets: Implications for crater size and formation mechanisms. *Icarus* 204:716–731. <https://doi.org/10.1016/J.ICARUS.2009.07.018>
- Fulchignoni M, Ferri F, Angrilli F, et al (2005) In situ measurements of the physical characteristics of Titan's environment. *Nature* 438:785–791.  
<https://doi.org/10.1038/nature04314>
- Gilbert GK (1893) The moon's face: A study of the origin of its features. *Science* 21:305–307. <https://doi.org/10.1126/science.ns-21.539.305-c>

- Hayes AG, Lorenz RD, Lunine JI (2018) A post-Cassini view of Titan's methane-based hydrologic cycle. *Nat Geosci* 11:306–313.  
<https://doi.org/10.1038/s41561-018-0103-y>
- Hedgepeth JE, Neish CD, Turtle EP, et al (2020) Titan's impact crater population after Cassini. *Icarus* 344:113664. <https://doi.org/10.1016/j.icarus.2020.113664>
- Hemingway D, Nimmo F., Zebker H, Iess L (2013) A rigid and weathered ice shell on Titan. *Nature* 500:550–552. <https://doi.org/10.1038/nature12400>
- Holsapple KA (1993) The Scaling of Impact Processes in Planetary Sciences. *Annu Rev Earth Planet Sci* 21:333–373.  
<https://doi.org/10.1146/annurev.ea.21.050193.002001>
- Holsapple KA and Schmidt RM (1982) On the scaling of crater dimensions 2. Impact processes. *J of Geophys Res* 87:1849–1870.  
<https://doi.org/10.1029/JB087iB03p01849>
- Hörst SM (2017) Titan's atmosphere and climate. *J Geophys Res Planets* 122:432–482.  
<https://doi.org/10.1002/2016JE005240>
- Ivanov BA, Deniem D, Neukum G (1997) Implementation of dynamic strength models into 2D hydrocodes: Applications for atmospheric breakup and impact cratering. *Int J Impact Eng* 20:411–430. [https://doi.org/10.1016/S0734-743X\(97\)87511-2](https://doi.org/10.1016/S0734-743X(97)87511-2)
- Ivanov BA, Langenhorst F, Deutsch A, Hornemann U (2002) How strong was impact-induced CO<sub>2</sub> degassing in the Cretaceous-Tertiary event? Numerical modeling of shock recovery experiments. In: *Catastrophic events and mass extinctions: Impacts and beyond*. Geological Society of America, pp. 29–49.  
<https://doi.org/10.1130/0-8137-2356-6.587>
- Kalousová K, Sotin C (2020) The Insulating Effect of Methane Clathrate Crust on Titan's Thermal Evolution. *Geophys Res Lett* 47:e2020GL087481.  
<https://doi.org/https://doi.org/10.1029/2020GL087481>

- Lindal GF, Wood GE, Hotz HB, et al (1983) The atmosphere of Titan: An analysis of the Voyager 1 radio occultation measurements. *Icarus* 53:348–363.  
[https://doi.org/10.1016/0019-1035\(83\)90155-0](https://doi.org/10.1016/0019-1035(83)90155-0)
- Lopes RMC, Malaska MJ, Schoenfeld AM, et al (2020) A global geomorphologic map of Saturn's moon Titan. *Nat Astron* 4:228–233.  
<https://doi.org/10.1038/s41550-019-0917-6>
- Lorenz RD, Wood CA, Lunine JI, et al (2007) Titan's young surface: Initial impact crater survey by Cassini RADAR and model comparison. *Geophys Res Lett* 34:1–5.  
<https://doi.org/10.1029/2006GL028971>
- Lunine JI, Atreya SK (2008) The methane cycle on Titan. *Nat Geosci* 1:159–164.  
<https://doi.org/10.1038/ngeo125>
- Maue AD, Levy JS, Burr DM, et al (2022) Rapid rounding of icy clasts during simulated fluvial transport in the Titan Tumbler. *Icarus* 375:114831.  
<https://doi.org/10.1016/J.ICARUS.2021.114831>
- McKinnon WB (2006) On convection in ice I shells of outer Solar System bodies, with detailed application to Callisto. *Icarus* 183:435–450.  
<https://doi.org/10.1016/J.ICARUS.2006.03.004>
- Melosh HJ, Ryan EV, Asphaug E (1992). Dynamic fragmentation in impacts: Hydrocode simulation of laboratory impacts. *J Geophys Res*, 97:14735–14759.  
<https://doi.org/10.1029/92JE01632>
- Mitri G, Showman AP (2005) Convective–conductive transitions and sensitivity of a convecting ice shell to perturbations in heat flux and tidal-heating rate: Implications for Europa. *Icarus* 177:447–460.  
<https://doi.org/10.1016/J.ICARUS.2005.03.019>
- Mitri G, Showman AP (2008) Thermal convection in ice-I shells of Titan and Enceladus. *Icarus* 193:387–396. <https://doi.org/10.1016/j.icarus.2007.07.016>



- Mitri G, Meriggiola R, Hayes A, et al (2014) Shape, topography, gravity anomalies and tidal deformation of Titan. *Icarus* 236:169-177.  
<https://doi.org/10.1016/j.icarus.2014.03.018>
- Neish CD, Barnes JW, Sotin C, et al (2015) Spectral properties of Titan's impact craters imply chemical weathering of its surface. *Geophys Res Lett* 42:3746–3754.  
<https://doi.org/10.1002/2015GL063824>
- Neish CD, Kirk RL, Lorenz RD, et al (2013) Crater topography on Titan: Implications for landscape evolution. *Icarus* 223:82–90.  
<https://doi.org/https://doi.org/10.1016/j.icarus.2012.11.030>
- Neish CD, Lorenz RD (2012) Titan's global crater population: A new assessment. *Planet Space Sci* 60:26–33. <https://doi.org/10.1016/J.PSS.2011.02.016>
- Neish CD, Lorenz RD (2014) Elevation distribution of Titan's craters suggests extensive wetlands. *Icarus* 228:27-34. <https://doi.org/10.1016/j.icarus.2013.09.024>
- Neish CD, Lorenz RD, Turtle EP, et al (2018) Strategies for detecting biological molecules on Titan. *Astrobiology* 18:571-585.  
<http://doi.org/10.1089/ast.2017.1758>
- Neish CD, Molaro JL, Lora JM, et al (2016) Fluvial erosion as a mechanism for crater modification on Titan. *Icarus* 270:114–129.  
<https://doi.org/10.1016/j.icarus.2015.07.022>
- Nesvorný D, Dones L, de Prá M, et al (2023) Impact Rates in the Outer Solar System. *Planet Sci J* 4:139. <https://doi.org/10.3847/PSJ/ace8ff>
- Nimmo F, Bills BG (2010) Shell thickness variations and the long-wavelength topography of Titan. *Icarus* 208:896–904.  
<https://doi.org/10.1016/j.icarus.2010.02.020>
- Ohnaka M (1995) A shear failure strength law of rock in the brittle-plastic transition regime. *Geophys Res Lett* 22:25-28. <https://doi.org/10.1029/94GL02791>

- Pierazzo E, Artemieva N, Asphaug E, et al (2008) Validation of numerical codes for impact and explosion cratering: Impacts on strengthless and metal targets. *Meteorit Planet Sci* 43:1917–1938.  
<https://doi.org/10.1111/j.1945-5100.2008.tb00653.x>
- Portenga EW, Bierman PR (2011) Understanding Earth's eroding surface with  $^{10}\text{Be}$ . *GSA Today* 21:4–10. <https://doi.org/10.1130/G111A.1>
- Richardson JE, Melosh HJ, Lisse CM, Carcich B (2007) A ballistics analysis of the Deep Impact ejecta plume: Determining Comet Tempel 1's gravity, mass, and density. *Icarus*, 191:176–209. <https://doi.org/10.1016/J.ICARUS.2007.08.033>
- Schenk P (2002) Thickness constraints on the icy shells of the galilean satellites from a comparison of crater shapes. *Nature* 417:419–421.  
<https://doi.org/10.1038/417419a>
- Schinder PJ, Flasar FM, Marouf EA, et al (2011) The structure of Titan's atmosphere from Cassini radio occultations. *Icarus* 215:460–474.  
<https://doi.org/10.1016/J.ICARUS.2011.07.030>
- Schurmeier LR, Brouwer GE, Fagents SA, et al (2023) Crater Relaxation Caused by an Insulating Methane Clathrate Crust on Titan. In: *LPI Contributions*. p 2813
- Schurmeier LR, Dombard AJ (2018) Crater relaxation on Titan aided by low thermal conductivity sand infill. *Icarus* 305:314–323.  
<https://doi.org/10.1016/J.ICARUS.2017.10.034>
- Shoemaker EM (1962) Interpretation of lunar craters. In: *Physics and astronomy of the moon*. New York: Academic Press, pp. 283–359
- Sierks H, Barbieri C, Lamy PL, et al (2015) On the nucleus structure and activity of comet 67P/Churyumov-Gerasimenko. *Science* (80- ) 347:1–6.  
<https://doi.org/10.1126/science.aaa1044>

- Silber EA, Johnson BC (2017) Impact crater morphology and the structure of Europa's ice shell. *J Geophys Res Planet* 122:2685–2701.  
<https://doi.org/10.1002/2017JE005456>
- Sklar LS, Dietrich WE (2001) Sediment and rock strength controls on river incision into bedrock. *Geology* 29:1087–1090.  
[https://doi.org/10.1130/0091-7613\(2001\)029<1087:SARSCO>2.0.CO](https://doi.org/10.1130/0091-7613(2001)029<1087:SARSCO>2.0.CO)
- Sloan ED, Koh CA, Koh CA (2007) *Clathrate Hydrates of Natural Gases*, Third Edition. CRC Press. <https://doi.org/10.1201/9781420008494>
- Soderblom JM, Brown RH, Soderblom LA, et al (2010) Geology of the Selk crater region on Titan from Cassini VIMS observations. *Icarus* 208:905–912.  
<https://doi.org/10.1016/J.ICARUS.2010.03.001>
- Sotin C, Mielke R, Choukroun M, et al (2009) Ice-Hydrocarbon Interactions Under Titan-like Conditions: Implications for the Carbon Cycle on Titan. In: *LPI Contributions*. p 2088
- Thompson SL, Lauson HS (1974) Improvements in the CHART D radiation-hydrodynamic code III: revised analytic equations of state. Rep, Sandia National Laboratories
- Tillotson JH (1962). Metallic equations of state for hypervelocity impact. Rep, DTIC Document pp. 141
- Tobie G, Lunine J, Sotin C (2006) Episodic outgassing as the origin of atmospheric methane on Titan. *Nature* 440:61–64. <https://doi.org/10.1038/nature04497>
- Tokano T, McKay C, Neubauer F et al (2006) Methane drizzle on Titan. *Nature* 442:432–435. <https://doi.org/10.1038/nature04948>
- Tomasko MG, Archinal B, Becker T, et al (2005) Rain, winds and haze during the Huygens probe's descent to Titan's surface. *Nature* 438:765–778.  
<https://doi.org/10.1038/nature04126>

- Turtle EP, Pierazzo E (2001) Thickness of a European Ice Shell from Impact Crater Simulations. *Science* 294:1326–1328. <https://doi.org/10.1126/science.1062492>
- Turtle EP, Lorenz RD (2021) The Dragonfly Mission to Titan: Technological Development and Science Converge to Enable New Exploration. *Bridge* 51:59–66
- Turtle EP, Trainer MG, Barnes JW, et al (2020) Dragonfly: In situ exploration of Titan's organic chemistry and habitability. In: *LPI Contributions*. p 2288.
- Vu TH, Choukroun M, Sotin C, et al (2020) Rapid Formation of Clathrate Hydrate From Liquid Ethane and Water Ice on Titan. *Geophys Res Lett* 47:1–8. <https://doi.org/10.1029/2019GL086265>
- Wakita S, Johnson BC, Soderblom JM, et al (2022) Methane-saturated Layers Limit the Observability of Impact Craters on Titan. *Planet Sci J* 3:50. <https://doi.org/10.3847/psj/ac4e91>
- Wakita S, Johnson BC, Soderblom JM, et al (2023) Modeling the Formation of Selk Impact Crater on Titan: Implications for Dragonfly. *Planet Sci J* 4:51. <https://doi.org/10.3847/PSJ/acbe40>
- Wood CA, Lorenz R, Kirk R, et al (2010) Impact craters on Titan. *Icarus* 206:334–344. <https://doi.org/10.1016/J.ICARUS.2009.08.021>
- Wünnemann K, Collins GS, Melosh HJ (2006) A strain-based porosity model for use in hydrocode simulations of impacts and implications for transient crater growth in porous targets. *Icarus* 180:514–527. <https://doi.org/10.1016/j.icarus.2005.10.013>
- Wünnemann K, Collins GS, Osinski, GR (2008) Numerical modelling of impact melt production in porous rocks. *Earth Planet Sci Lett* 269:530–539. <https://doi.org/10.1016/J.EPSL.2008.03.007>

Wünnemann K, Nowka D, Collins GS, et al (2011) Scaling of impact crater formation on planetary surfaces – insights from numerical modeling. In: Proceedings of the 11th Hypervelocity Impact Symposium. pp 1–16

Zahnle K, Schenk P, Levison H, Dones L (2003) Cratering rates in the outer Solar System. *Icarus* 163:263–289. [https://doi.org/10.1016/S0019-1035\(03\)00048-4](https://doi.org/10.1016/S0019-1035(03)00048-4)

## Chapter 4

### 4 Lessons Learned from the Rover-Aerial Vehicle Exploration Network (RAVEN): Applications for Future Operational Procedures for Unoccupied Aircraft Systems (UAS) Missions

Unoccupied Aircraft Systems (UAS) present a novel approach to planetary surface exploration, offering access to terrains that are either challenging or entirely inaccessible to rovers. The Ingenuity helicopter, part of the Mars 2020 mission, serves as a pioneer and technology demonstration for UAS missions. However, given the new and unique nature of UAS planetary exploration missions, optimal applications and operational strategies using UAS capabilities are yet to be fully understood. Terrestrial analogue terrains provide an opportunity to test the development and implementation of UAS missions. As part of the Rover-Aerial Vehicle Exploration Network (RAVEN) project, we simulated a mission operations scenario using a UAS equipped with a scientific payload. This UAS was modeled after future Mars UAS concept studies, such as the Mars Science Helicopter. It was capable of capturing in-flight and landed imagery, and it was equipped with instruments for conducting contact science at the UAS landing site. The mission simulation took place at the Holuhraun lava flow field in Iceland, an ideal analogue for geologically young volcanic terrain on Mars. Throughout the mission simulation, we discovered that oblique imagery acquired in-flight provided the most useful data for scouting landing sites and identifying sampling locations. Grounded imagery of the foreground lacked sufficient contrast for detailed studies, and microimages at the landing site did not offer enough textural details. In a subsequent ground-truthing exercise, we found that the UAS successfully imaged different lava morphologies in the region and provided details about the adjacent sand sheet. These lessons are valuable for drawing applications for future UAS-style missions, such as Dragonfly, scheduled to explore the surface of Titan in the 2030s.

## 4.1 Introduction

Planetary exploration strategies have evolved significantly since the start of the space age, propelled by scientific curiosity and advancements in technology. Specifically, robotic exploration within the solar system has transformed from early flyby missions to the more sophisticated deployment of orbiters, landers, and rovers. A recent addition is the use of Unoccupied Aircraft Systems (UAS) as a new tool for planetary exploration. Planetary aviation is possible by leveraging the atmospheres of planetary bodies such as Mars and Titan (e.g. Lorenz, 2022a), and can help enhance the exploration of their surfaces. The Ingenuity helicopter (Balaram et al., 2021), accompanying the Perseverance rover (Farley et al., 2020), serves as a technology demonstration for exploration of the Martian environment via an aerial platform. Lessons learned from this mission are informing future UAS-style missions to Mars, including their potential use in Mars Sample Return (Muirhead et al., 2020). Continuing this progression, the upcoming Dragonfly mission to Titan (e.g. Turtle & Lorenz, 2021; Lorenz et al., 2018) will be the first UAS-style exploration mission equipped with a scientific payload (Barnes et al., 2021). Controlled, aerial-flight vehicles equipped with capable scientific payloads represent a novel approach to planetary surface exploration, engaging in both in-flight and landed science and operations.

One of the main benefits of a UAS is that its aerial capability allows access to locations inaccessible by surface assets like rovers. Additionally, it can scout and acquire high-resolution imagery for a larger region than a rover. The resultant images can be used for science but also for identifying safe future landing sites. The landed capability of a UAS allows for remote and contact science in the landing-site workspace (Bapst et al., 2021; Johnson et al., 2020). For combined rover-UAS missions, like Perseverance and Ingenuity, the UAS acquired imagery can be used to produce Digital Terrain Models (DTM), which can improve rover positioning and trafficability.

UAS offers a novel and rather important method of investigating planetary surfaces. However, operations strategies for these types of missions are not as fully developed as they are for the more established orbital and surface exploration assets. Consequently, mission simulations conducted in planetary analogue terrains on Earth can provide a space

for testing UAS-mission capabilities and operational strategies. Terrestrial analogues are sites that approximate the geological, environmental, and/or biological conditions on a planetary body of interest (Osinski et al, 2019a; Hamilton et al., 2023). Thus, analogue sites provide an opportunity for conducting not only comparative planetology science studies, but also provide a testing ground for new mission technologies, designs, architectures, and operations. Such simulations are also useful in training of personnel for future mission science planning and operations (Osinski et al., 2019a). Simulating exploration missions using rovers and humans in analogue environments is a common practice and there exists a suite of such studies (e.g. Cannon et al., 2007; Marion et al, 2020; Osinski et al, 2019b). Building on these previous analogue mission simulations, we conduct a UAS-based mission simulation in a Mars analogue terrain. Here, we present the lessons learned and its potential applications for future UAS-style missions such as Dragonfly.

#### 4.1.1 Rover-Aerial Vehicle Exploration Network

The Rover-Aerial Vehicle Exploration Network (RAVEN), funded through NASA's Planetary Science and Technology through Analog Research (PSTAR) program, was designed to develop new planetary mission designs that integrate both UAS and rover platforms. The goals of the RAVEN project are to test three mission architectures. The first two goals are to test a rover-only (Gwizd et al., 2023) and a UAS-only mission simulation to understand the capabilities and limitations of the two platforms. These missions were both completed in 2022 in Iceland. The third goal is to use lessons learned from the two independent simulations to design a combined rover-UAS mission simulation to enhance the scientific output of future missions to Mars. This mission was completed in 2023 in California. The first two missions tested different science operations strategies at a Mars analogue site located at the Holuhraun lava flow-field in Iceland (Hamilton et al., 2015, 2023; Voigt et al., 2023). Holuhraun is the site of the largest flood lava eruption in Iceland in the past 230 years and serves as an ideal analogue for geologically young volcanic regions on Mars. The third mission tested the rover-UAS combined simulation at an undisclosed location in the southern California desert, which hosts Mars analogue terrains and rock types.



The science motivation for RAVEN is driven by better understanding the hydrothermal systems associated with flood lava eruptions on Mars, as they represent key targets for astrobiological studies (e.g. Burr et al., 2002, 2009; Plescia, 2003; McEwen et al., 2005; Jaeger et al., 2007, 2010; Lanagan et al., 2001; Fagents & Thordarson, 2007; Cousins and Crawford, 2011; Cousins, 2011). However, traversing rough lava flows would not be possible using only a rover platform. Hence, combining a ground-based science laboratory and the aerial capabilities of UAS enables exploration of volcanic terrains and the lava-induced hydrothermal systems within.

Even though the main objective of the RAVEN project is to test mission architecture and operations, we established secondary science goals to guide and evaluate science operations strategies. A Science Traceability Matrix (STM) was developed to meet the science goals of NASA's Mars Exploration Program Analysis Group (MEPAG) (e.g. Grant et al., 2006; Diniega et al., 2019). The high-level mission observables that drove science planning and operations included lava flow morphology, lava–water interactions, hydrothermal alteration features, sediments/rocks with high biosignature preservation potential, geochemistry and mineralogy of active sand, and morphology of aeolian bedforms. Here, we present the mission development and operational results of the UAS-independent mission simulation.

## 4.2 Mission Development

For the RAVEN mission simulation, we designed a UAS helicopter in accordance with potential next generation Mars UAS specifications, specifically drawing inspiration from the Mars Science Helicopter (MSH; Saez et al, 2021; Bapst et al., 2021; Johnson et al., 2020). These spacecraft are intended to build upon the technology demonstration of Ingenuity and possess scientific capabilities for executing in-flight and landed operations. Consequently, we set constraints on our simulated UAS based on the MSH, including a 5 kg scientific payload, and a daily flight duration and range of approximately 6 minutes, and 1 km, respectively. Additionally, we imposed daily power and data budgets of 333 Wh and 140 MB, respectively. These limits were established by scaling the specifications of the aforementioned Mars UAS concept studies. It is important to note, though, that the detailed development of the resource and power budget is beyond the scope of this thesis.

For the purpose of this simulation, we did not manufacture our own UAS system, as it would be beyond the cost budget. Instead, we implemented the mission using a variety of commercial drones and hand-held instruments to accommodate the full science payload. A DJI Matrice 300 fitted with the Zenmuse P1 camera acquired images in the air and on the ground. Since this camera is fitted on the UAS with a single-axis 180° gimbal only a few centimeters above ground level, it would not be able to focus on the ground. Consequently, we also added a microscopic imager (microimager) to acquire images of the sampling locations and investigate the landing site at the grain-size scale. Two DJI Matrice 600s were used for sampling. One of these drones was equipped with a claw/scoop sampler with 4 (interchangeable) designs to test the best instrument configurations for future Mars missions (**Figure 4.1**). This is a prototype developed by Honeybee Robotics, called RAVEN Claw. The other DJI Matrice 600 was equipped with a coring drill. In practice, the drill was not yet capable of coring basalt (it was too hard), so a hand coring drill was used instead. There were two additional hand-held payloads to acquire information about the composition of the terrain. The team initially planned to use a hyperspectral imager (VIS–IR/400–2500 nm) for the first payload. However, due to practical field conditions (variable illumination) and technical challenges (image cubes too large to work within the mission simulation bandwidth), we opted instead to use a point spectrometer. This worked successfully to obtain VIS–IR spectra at landing locations. The remaining payload was a Laser-Induced Breakdown Spectrometer (LIBS) (1064 nm). This is analogous to the SuperCam instrument (Nelson et al., 2020) onboard the Perseverance rover, which is designed to determine the mineralogy of the study site.

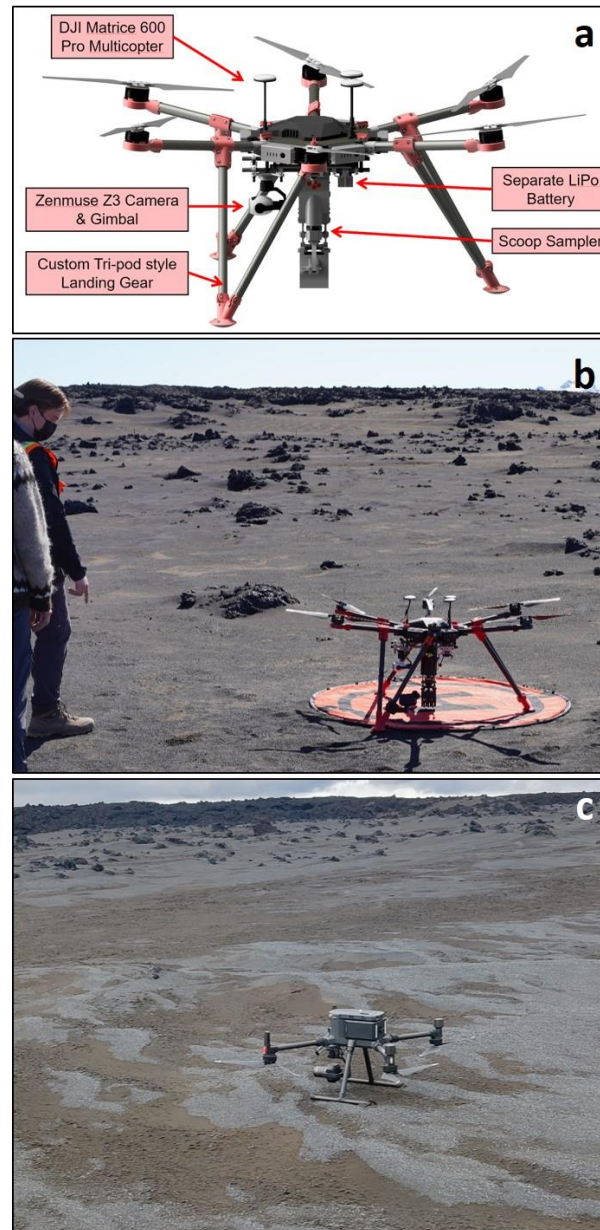


**Figure 4.1: (a) A schematic of the DJI Matrice 600 UAS with custom landing gear and scoop (with swappable jaws). (b) DJI Matrice 600 with the sampling scoop and (c) DJI Matrice 300 with the P1 camera landed in the field site.**

#### 4.2.1 Team Structure

The UAS mission simulation involved the collaboration of two distinct teams: operations and implementation. The science operations team determined the science targets and drafted the flight plans, consisting of four members: Tactical Science Lead, Science

Planner, UAS Planner, and Documentarian. Each team member undertook specific tasks and also served as support scientists, contributing to science target selection and discussion. The team was assembled with the relevant scientific expertise, taking into account the volcanic nature of the field site and the associated science goals. It's important to acknowledge that in a real mission operations scenario, a larger and more scientifically diverse team would be essential. The field implementation team, serving as the counterpart to the operations team, carried out the UAS operations in the field and created downlink products.

#### 4.2.2 Planning Procedures

In addition to calculating the specifications for the simulated UAS, the operations team developed and followed a Sol (Mars day) Planning Meeting Protocol based on the format of Mars rover mission operations. This planning procedure closely mirrored that of the rover-only RAVEN mission (Gwizd et al., 2023) running concurrently, allowing for comparisons of the science returns between the different mission scenarios. The procedure was comprised of the following segments: (1) Downlink Assessment: summary of previous sol and review of data provided by the implementation team; (2) Planning Kickoff: summary of mission to date and review of current UAS location and proximity of science targets; (3) Science Target and Activity Discussion: main planning segment which included discussion of science targets and activities, as well as formulation of the flight plan for the next sol; (4) Plan Building: UAS resource calculations to create a final plan and write up the Plan Translation Form (to send to the field implementation team). This form outlined the UAS flight plan, detailing all science targets and activities scheduled for execution the following sol. The Plan Building segment also served as the final step for eliminating science targets and activities that did not align with the technical plan; (5) Look Ahead Planning: brainstorming science targets and activities for  $N + 1$  and  $N + n$  sol (where  $N$  represents the current sol and  $n$  is any positive integer); and (6) Post-Planning Activities: generation of daily sol reports by all team members and plan translation to implementation team.

### 4.2.3 Science Operations

The science planning and operations were guided by the science goals outlined earlier, while balancing UAS resources and safety. The operations were supported by pre-mission planning using remote sensing data of the Holuhraun region. The data included visible imagery (25 cm/pixel) and a digital elevation model (DEM, 1 m/pixel) with resolutions equivalent to the High Resolution Imaging Experiment (HiRISE) instrument (McEwen et al., 2007) onboard the Mars Reconnaissance Orbiter. The imagery was used to identify science targets. Additionally, a slope/hazard map was derived from the 1-meter DEM to aid in identifying potential landing sites. We were also provided with a lava flow morphological map from Voigt et al. (2021) to inform science targeting. Using this information, we developed and implemented data collection strategies for the in-flight and landed capabilities of the UAS.

The in-flight operations were driven by scouting the study area for landing sites and science targets. For in-flight data collection, we relied on 3 imaging modes. 1) The photogrammetry survey was conducted at an altitude of 80-120 m and had the advantage of covering a large area in a single flight at high resolution. These surveys were planned to be used for identifying future landing sites for the UAS. 2) The aerial oblique imaging mode acquired images in flight at 40-60 m above ground level (AGL), for the purpose of identifying science targets. 3) Lastly, the ascent and descent images were planned to be used for gathering context and close-up imagery of the landing site at altitudes ranging from 3 to 120 m. The landed operations were governed by sampling goals and contact science locations. In addition to contact science, we planned to use the landed capabilities to acquire landed images and microimages of the landing-site workspace and sampling locations.

We conducted a subsequent field exercise in 2023 to ground-truth the UAS acquired data with a small team led by a volcanology expert. Ground truthing exercises have proven to be useful in validating remote sensing data and providing improved orbital data acquisition methods (e.g. Steven, 1987; Rossi & van Gasselt, 2018). In addition, ground-truthing is not currently an option for other planetary bodies (e.g. Mars, Titan). As such, conducting this exercise at the analogue sites where operations are being tested is

valuable. In this ground-truthing exercise, time and field accessibility constraints did not allow for following the UAS flight path directly. However, we visited the characteristic sites of the different terrains the UAS explored.

## 4.3 Results

### 4.3.1 Mission Summary

The UAS team completed a 12-sol mission, of which 9 sols included flights and 3 sols were used for sampling. The UAS flew a total of 10 km (**Figure 4.2**), surveyed an area of 70,000 m<sup>2</sup>, acquired 86 images, and collected 3 samples, 10 LIBS measurements, and 10 VIS-IR point spectrometer measurements. On flight sols, the average flight distance was 1395 m and the average flight time was 224 s. Recall, the daily flight duration and range limits were set to ~6 mins (360 s) and ~1 km, respectively. The UAS was capable of exceeding the 1 km limit on days when it did not engage in power-intensive tasks, such as photogrammetric surveys.

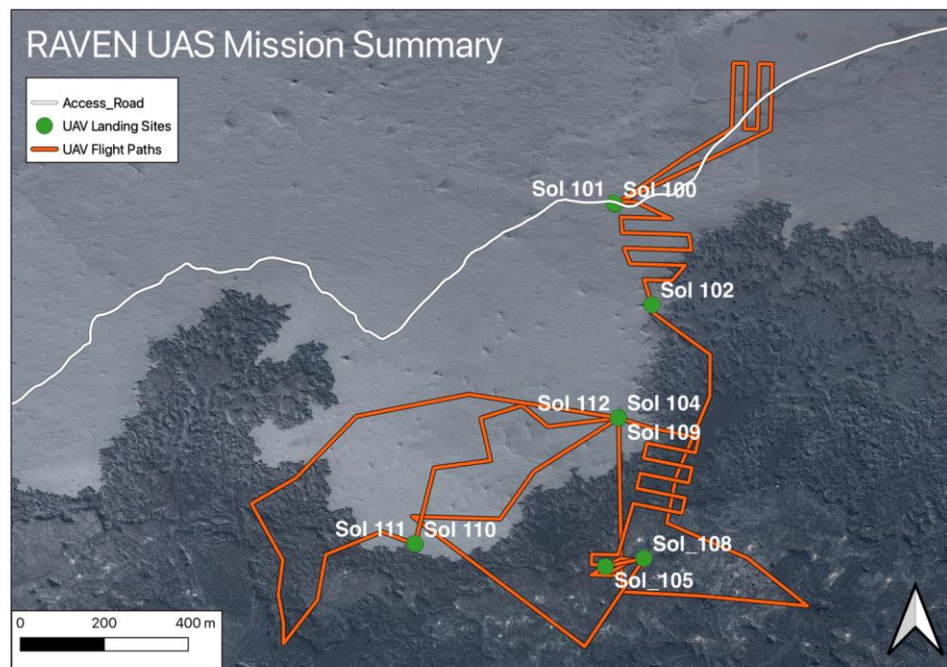


**Figure 4.2:** Map showing the UAS landing sites (in green) and flight paths (in orange) with the sol number annotated, overlain on the UltraCam-Xp pre-mission basemap.

### 4.3.2 Simulation Results

There were some key lessons learned from the simulation exercise, mainly related to how the data was acquired. These lessons are outlined below:

- a. The UAS team initially planned and conducted high-resolution photogrammetric surveys to scout for landing sites and science targets. The utility of these surveys for N + 1 mission planning was deemed low, and as such, the associated resource allocation was not justified. These surveys did not provide adequate detail or contrast to identify further targets at selected sites. However, they have proven valuable for post-mission analysis, particularly for detailed studies of morphology (e.g. dune amplitude & wavelength, width of channels and fractures, size of blocks). A caveat to note is that this process consumed a significant amount of power and data. Therefore, while crucial for post-planning and mission science analysis, it is not deemed essential for decisional downlink.
- b. Oblique airborne images acquired at low altitudes demonstrated the most usefulness for mission planning, offering a good sense of depth and scale of the surface features of interest. Drawing from these early mission simulation insights, we modified our airborne imaging strategy to incorporate additional flight time and airborne images, while reducing the emphasis on mapping surveys.
- c. Nadir-looking images acquired during a photogrammetric survey flight and/or during ascent/descent imaging failed to offer sufficient contrast (likely due to imaging geometry) for identifying detailed features. Furthermore, the UAS could capture its closest-to-the-ground descent image at approximately 5 meters AGL without landing, imposing limitations on the level of detail extractable from descent images.
- d. Grounded images acquired from the P1 camera, positioned only a few centimeters above ground level (AGL), did not yield optimal contrast between the science target in the foreground and the horizon (see **Figure 4.3**). More than one-third of the grounded image contains the bright sky, which fails to provide the contrast

necessary to distinguish the darker surface in the foreground. This effect is further demonstrated in **Figure 4.4**, where the dark lava flow in the foreground is overpowered by the brighter sky. Therefore, it would be advantageous for future missions to possess the capability to capture images during descent at a relatively low AGL, equivalent to human eye level. Another alternative is to acquire two images, one focused on the near-field and one on the far-field, in areas with high-contrast fields.

- e. Imaging prospective landing sites, even from a distance, on a sol prior to visiting the site proved crucial for validating landing hazard analyses derived from pre-mission orbital data. This practice facilitated more accurate landings in diverse areas that would otherwise have been constrained to large, flat sandy patches.
- f. The UAS was limited to contact science on materials upon which it could land. Surface types that proved too rubbly for landing (e.g. any lava flow surface lacking a smooth crust) were not subjected to detailed analysis by the UAS.

Our mission planning was primarily informed by the interpretation of oblique images and expertise in volcanology, given the team's science proficiency. Despite the UAS acquiring sufficient geochemistry data, the LIBS and VIS-IR data sets were underutilized in the planning phase due to the team's lack of expertise in these specific domains.

In this simulation exercise, we discerned that in-flight oblique imaging mode was most useful for scouting landing sites and identifying science targets, compared to photogrammetric surveys which proved to be more informative for post-planning scientific discussions. This lesson is crucial as it contributed to prioritizing the order of in-flight operations and data downlink. Additionally, we identified that the current camera configuration imposes limitations on the grounded imaging capabilities of the UAS. These insights serve as valuable guidance for informing and refining future operational strategies.



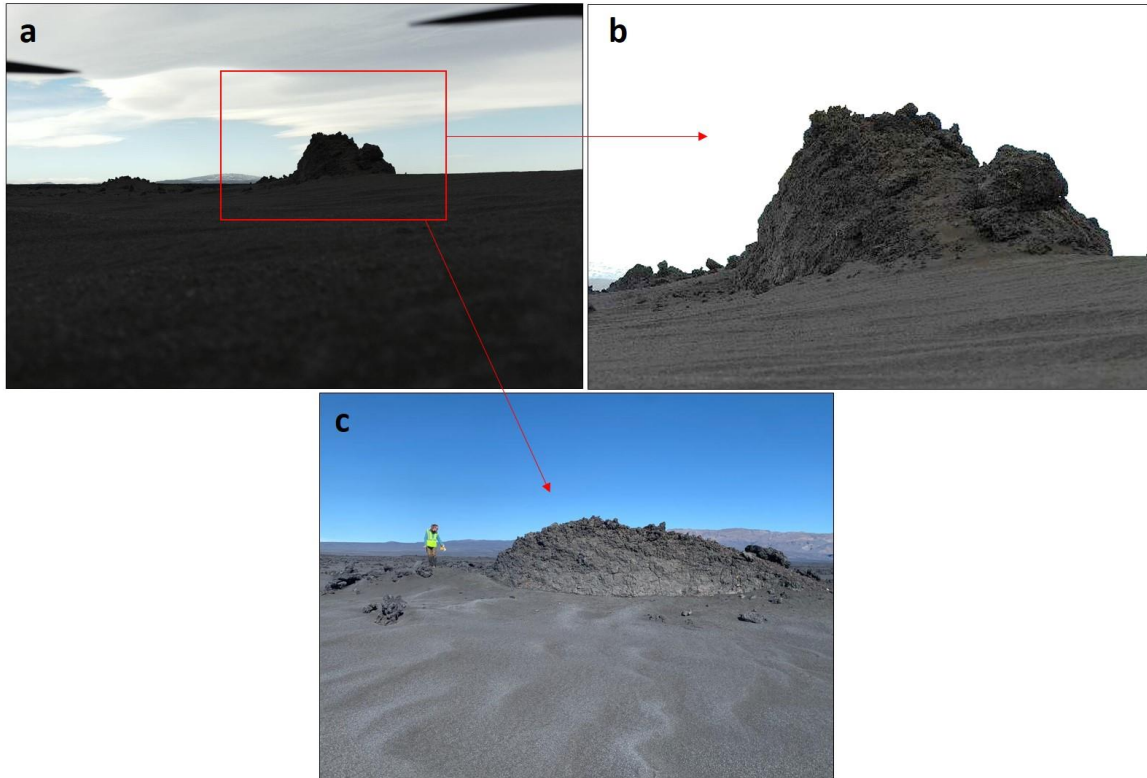


**Figure 4.3: (a) Sol 102 UAS grounded image of a feature interpreted to be a rotated lava flow crust. (b) A zoomed in and stretched version of image (a). (c) Field image of the same feature.**



**Figure 4.4: Sol 111 UAS grounded image on the lava flow.**

### 4.3.3 Ground-truthing Results

The lessons learned from the ground-truthing exercise can further improve our understanding of a UAS mission capabilities and limitations.

- a. The UAS proved highly successful in observing aeolian features within the study area (Figure 4.5). We detected large cross-bedding sinuous ripples using both oblique imagery and photogrammetric surveys. The contrast in the oblique images enabled us to identify the wind transport direction, later confirmed during ground-truthing. With the addition of pre- and post-sampling images and geochemistry data, we also identified grain-size variations between the small, light-toned ripples and the underlying darker sediment.
- b. In addition to the aeolian observations, the UAS, with its capacity to survey a large area, successfully captured the various lava morphologies present in the study region.
- c. One key lesson learned from the field was that, despite having a volcanologist on the operations team, we overlooked some observations because they were more familiar with lava morphologies different than those encountered at Holuhruan. Consequently, it appears essential to include at least one team member on the science operations team who possesses knowledge of a similar field environment to guide target selection and decisional science. While this may not be feasible for planetary missions, given the absence of firsthand experience on Mars, analogue studies and mission simulations like this one become vital for training operations personnel. Running analogue missions in relevant terrestrial environments allows us to approximate what to anticipate from the data returned in future missions.
- d. Another lesson learned in the field was the challenge of perceiving scale in aerial imagery. We attribute this difficulty, in part, to our familiarity with conventional rover-level imagery and insufficient experience in working with aerial data for mission science planning. The limited understanding of scale constrained our interpretations of the observed volcanic features. It is important to note that while

we did not create a scale for the images captured by the UAS due to personnel constraints, it is feasible to generate a scale using UAS telemetry data and camera specifications. Additionally, the absence of natural "scale bars", such as human structures or vegetation did not help. However, this serves as a valuable comparison, as these natural scale bars would be unavailable on other planets as well.

- e. We also observed that the microimager provided adequate grain-size context for the sampling location, but it was less effective in providing textural clues about the lava flow. In Figure 4.6 below, we present a photograph acquired with the microimager alongside a field image illustrating the spiny texture of the lava flow. The microimager failed to capture the spiny texture, which serves as an indicator of lava morphology and flow direction. It is noteworthy that lighting conditions have an influence on image contrast and, consequently, on the visibility of highlighted features. This consideration should be taken into account in future planning.

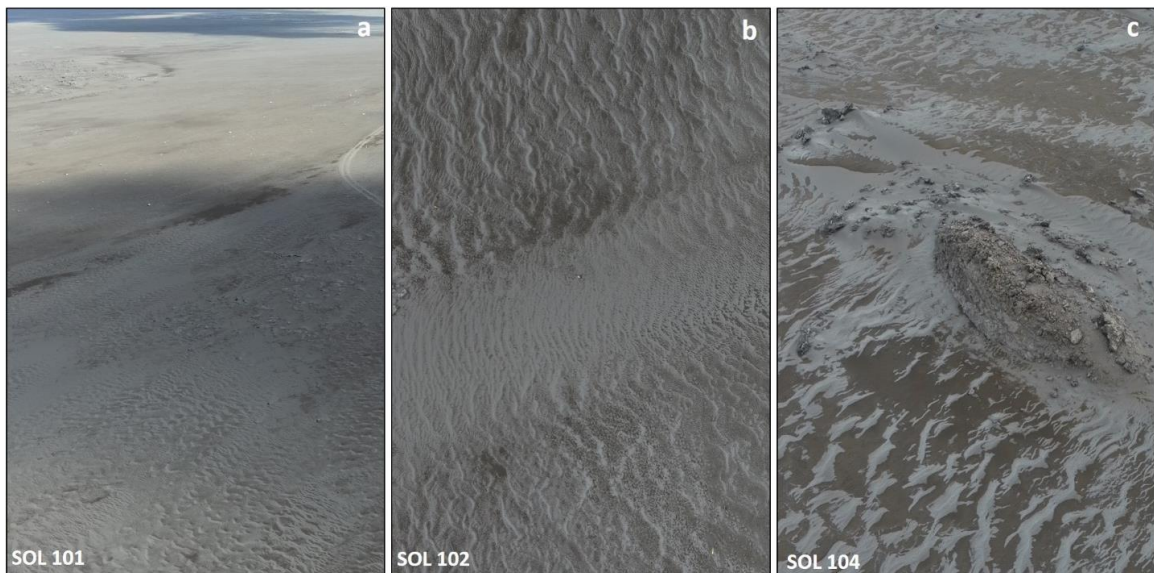


**Figure 4.5: Select UAS images of the sandsheet in the study area showing large ripples made up of two different (light and dark-toned) sediments.**

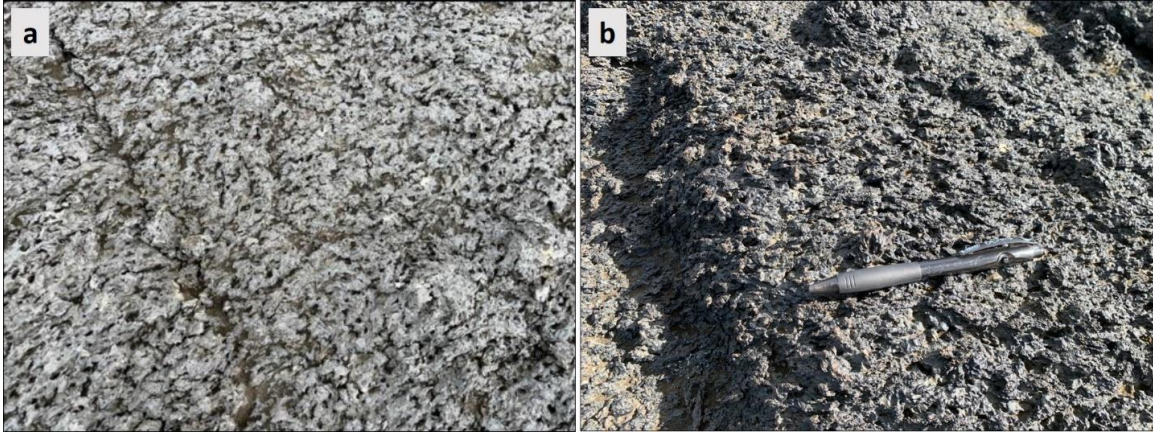


**Figure 4.6: (a) Image acquired with the UAS microimager on Sol 105 of the lava flow compared to (b) the field image of a similar feature.**

## 4.4 Discussion

The RAVEN mission simulation offered valuable insights into the capabilities and limitations of a UAS-based mission. Several general applications emerged from the simulation that can inform future UAS mission operations. One crucial lesson learned is that oblique imagery yields better contrast compared to nadir-looking imagery, useful for identifying surface details and features of interest. This finding underscores the importance of incorporating oblique imaging capabilities into future UAS camera designs, allowing gimbals to capture images at various look angles. Furthermore, the use of oblique imaging proved advantageous in planning future in-flight operations, particularly when scouting for sampling locations and landing sites. Prioritizing oblique imaging in these scenarios enhances the ability to capture comprehensive and informative visual data.

Lastly, but significantly, it is advisable to familiarize oneself with working with aerial imagery and developing a sense of scale perception before undertaking operations. This preparation is essential for adapting to a UAS grounded view, which differs from the conventional rover perspective. However, this is dependent on UAS configurations. For instance, the camera in the mission simulation is only a few centimeters above the ground, whereas the cameras are situated much higher on the Dragonfly spacecraft, as it is more comparable in size to the Perseverance rover (Lorenz et al., 2022a). Therefore, it would be useful to understand the height of the cameras before the mission and how the different

perspectives provide different information. In general, providing appropriate scale bars using objects of known size for different imaging perspectives (landed and in-flight at different altitudes) would be beneficial. By doing so, the operations team can optimize their decision-making processes and enhance the overall success of UAS missions. Scale perception is especially important because the scale of the feature will dictate the optimal imaging geometry to implement.

#### 4.4.1 Applications to Dragonfly

We can apply some of our findings to the future operations of NASA's upcoming Dragonfly mission to Titan, currently scheduled to launch in 2028 (e.g., Turtle & Lorenz, 2021). Dragonfly is designed as a relocatable lander with rotorcraft capabilities, using Titan's dense atmosphere to fly to various locations on the surface. The aerial capability is motivated by the desire to acquire samples from different sites on Titan (e.g., Lorenz et al., 2018). Moreover, a UAS platform serves as a safer exploration method compared to a rover, given the limited knowledge about Titan's surface. The surface may prove to be non-traversable, especially if the organic sand on Titan is sticky or muddy (e.g., Radebaugh, 2009; Lorenz, 2022b). In this sense, Dragonfly essentially functions as a UAS with a scientific payload, capable of both in-flight and landed operations, similar to the RAVEN UAS.

The Dragonfly operations will be guided by the following primary science goals: investigating prebiotic chemistry through the sampling of Titan's surface, understanding Titan's methane cycle, conducting further studies on Titan's geology, and identifying biosignatures to enhance our understanding of Titan's astrobiology and habitability (Barnes et al., 2021). To address these goals, Dragonfly will be equipped with 5 instruments: 1) DragonCam: a set of cameras (**Figure 4.7**), 2) DraGMet: a geophysics and meteorology package, 3) DrACO: a drill for sampling organics and transporting them to 4) DraMS: a mass spectrometer, and 5) DraGNS: a gamma-ray and neutron spectrometer for determining bulk surface composition (Barnes et al., 2021).

Dragonfly's primary study site is Selk crater, a relatively fresh impact crater offering the opportunity to sample the two main materials expected to be present on Titan's

surface: organic-rich and water-ice-rich materials (Barnes et al., 2021). However, its initial landing is planned for the interdunes of the Shangri-La sand sea, a relatively flat, smooth, and rock-free area selected to minimize landing risks (Lorenz et al., 2021). Subsequently, Dragonfly will fly towards Selk crater, conducting studies of the dunes along its path. Although this geological terrain differs from Holuhraun, the dunes that Dragonfly will traverse should bear resemblance to the sand sheet and associated aeolian processes encountered at Holuhraun. Our UAS simulation revealed that in-flight imaging was successful in providing adequate information of the sand sheet.

The Dragonfly science payload is specifically designed to explore Titan's terrain, namely organic sand dunes, interdunes, and an ice-rich impact crater, and therefore differs from that of the RAVEN UAS, which focused on the analysis of silicate rocks. Furthermore, since the UAS contact science data was not used for science planning due to a lack of expertise in interpretation, we refrain from drawing parallels regarding landed and contact science. Nevertheless, we can comment on the imaging practices employed by the RAVEN UAS and how they might be applicable to Dragonfly.

Dragonfly's camera suite, DragonCam (**Figure 4.7**), includes forward and downward cameras for in-flight and landed imaging, as well as a microscopic imager (microimager) capable of examining the surface at a sand-grain scale. The microimager will be equipped with light-emitting diode (LED) lights to compensate for the poor illumination conditions on Titan (Lorenz et al., 2018). In this scenario, the ability of the Dragonfly microimager to acquire a stereo pair along with LED illuminators might mitigate the challenges in highlighting surface textures experienced by the UAS microimager (because of the variable lighting conditions in Iceland). The LEDs can also provide compositional information. Additionally, if these stereo image pairs can be used to create a Digital Terrain Model (DTM), it could be useful for mapping the directionality of surface microtextures and features. In addition to lighting conditions, it would be important to consider cloud cover and how that affects the quality of the image. Although this was not directly investigated during the RAVEN UAS simulation, it would be worth exploring during future Dragonfly analogue/simulation studies.

As learned from the UAS mission simulation, scouting landing sites a sol prior to the planned landing was valuable in validating landing hazards. This practice is expected to be particularly crucial for Dragonfly, given the limited availability of high-resolution pre-mission data. The current surface operations plan for Dragonfly (see **Figure 4.8**) already includes scouting flights, which will search for new landing sites, and leapfrog flights, which will fly over previously scouted landing sites to identify potential future landing sites.

Considering the challenges encountered in finding a safe landing site on the lava flow during the RAVEN simulation, even with the assistance of high-resolution pre-mission data (unavailable for Titan), we anticipate that Dragonfly may need to conduct multiple scouting flights. This becomes especially pertinent when flying closer to Selk crater and identifying a secure landing site in that vicinity. The Selk crater rim region is likely composed of rough and fractured water-ice material (Lorenz et al., 2021; Bonnefoy et al., 2022), which may pose challenges for landing.

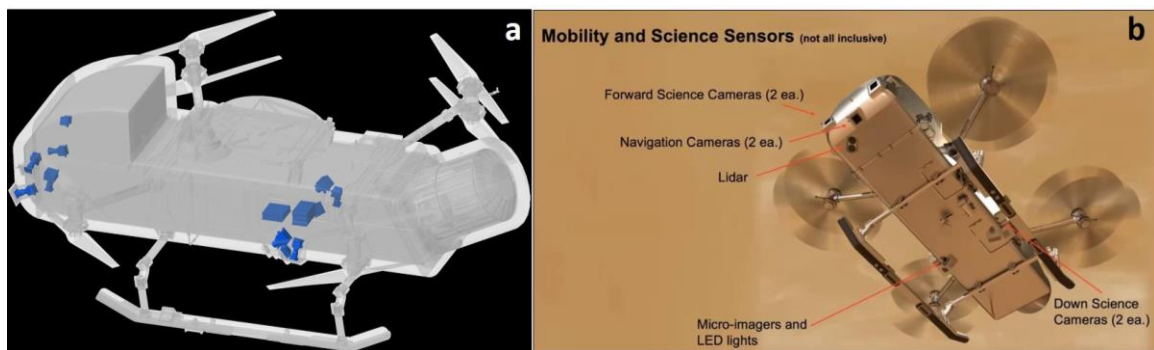


**Figure 4.7:** (a) Schematic of the DragonCam layout on the Dragonfly spacecraft. Each blue region is a different component of the DragonCam suite. (b) A labelled schematic of DragonCam with the locations of the different cameras. This exact configuration is subject to change. Credit: David Napolillo and Magda Saina/APL.

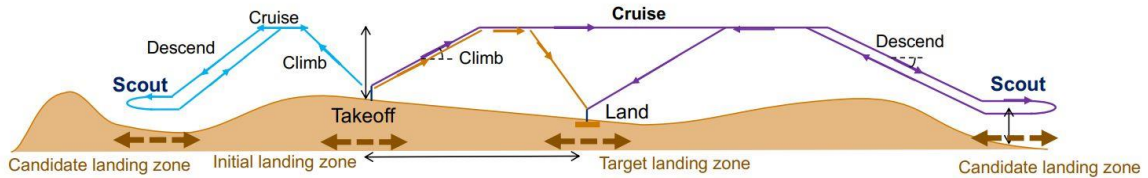


**Figure 4.8: Types of aerial flights planned for Dragonfly surface operations. Scout flights (blue) are used to identify future landing sites. Jump flights (orange) are used to exit the local exploration region. Leapfrog flights (purple) are used to scout the next landing site, flying over a previously scouted landing site and then returning to land there. Credit: APL.**

#### 4.4.2 Limitations

While this mission simulation provided important insights for operating future UAS missions, we acknowledge the inherent limitations that constrain its applications. Firstly, the UAS exploration capacity was restricted to areas accessible by the field implementation team on foot. In theory, there might have been locations on the lava flow where the UAS could have landed, but if the field team could not traverse the terrain, it was excluded from the operations plan. Since daily science planning relies on the data returned from the UAS, the mission's trajectory is significantly influenced by what is observed and, conversely, what remains unseen.

Additionally, we faced limitations imposed by field conditions, such as lighting and weather, sometimes leading to no-flying breaks and poor imagery. This constraint is applicable not only to terrestrial missions but also extends to planetary missions. Another crucial limitation is that the lessons derived from this simulation are grounded in a volcanic terrain. Therefore, the imaging preferences identified may be most applicable to similarly rough and homogenous terrains, such as the Holuhraun lava field site. Consequently, different imaging campaigns may be necessary for identifying safe landing and sampling locations within, for instance, an impact crater. The Houghton crater in the Canadian High Arctic serves as an excellent candidate for future work. This complex crater is situated in a polar desert environment and has been moderately eroded by fluvial processes, rendering



it a suitable analogue for Selk crater on Titan (Osinski et al., 2005; Neish et al., 2018; 2021).

Initially, it would be beneficial to test various imaging campaigns aimed at identifying sampling locations within a crater and its surrounding region. Replicating images that DragonCam is expected to capture, particularly those depicting landed and micro images, may not necessarily alter current configurations but would aid in optimizing scientific operations. Moreover, considering that the RAVEN UAS descent and grounded images did not provide meaningful context for the landing site workspace, it is crucial to explore best imaging practices for Dragonfly. Originally, Dragonfly was planned to feature a panoramic camera (PanCam) capable of acquiring a 360° image at a landing site. However, due to mass constraints, this feature was rearranged. Presently, all cameras are positioned in the spacecraft body (**Figure 4.7**), providing a maximum coverage of 270 degrees. Simulating the acquisition of a 360° aerial image just before landing, by hovering a few meters above ground and rotating the spacecraft, could potentially compensate for the lack of a grounded 360° panoramic image. This can also be achieved upon returning from a scout flight and landing (at the same site it took off from) 180° off from its original azimuth at that location. These two images, each with 180° coverage, can then be mosaicked together to provide a comprehensive 360° coverage product. Alternatively, conducting an exercise comparing a 360° image to a 270° panoramic image would reveal any potential gaps in information. This analysis could shed light on whether acquiring a full panorama would have led to different conclusions or science decisions. Lastly, it is advisable to train science operations personnel at terrestrial analogue sites, such as sand dunes and impact craters, in preparation for Dragonfly.

## 4.5 Conclusions

As part of the RAVEN network, we conducted a 12-sol mission simulation using a UAS platform capable of in-flight and landed science at the Holuhraun lava field in Iceland. The RAVEN project is driven by the necessity to test new exploration strategies using UAS for accessing rough terrains, such as volcanic regions on Mars, which are inaccessible via rovers. Our UAS performed imaging flights to scout for safe landing sites and sampling locations. UAS landed operations included grounded imagery, sampling, and geochemistry

measurements (using hand-held LIBS and VIS-IR spectrometer). From this exercise, we garnered key lessons useful for informing future UAS missions, such as the Mars Science Helicopter and the Dragonfly mission to Titan. We conclude that oblique imagery acquired in-flight provided the most context for identifying safe landing sites and sampling locations. In contrast, landed imagery did not prove to be useful for capturing features in the foreground. Similarly, images captured using the microscopic imager did not provide enough textural information at the landing site. However, we acknowledge that field lighting conditions also play a role here. Some of these lessons can be applied to aid in preparation for Dragonfly surface operations in the 2030s.

The current Dragonfly surface operations plan for scouting new landing sites aligns well with the results from the UAS mission simulation. Scouting new landing sites in advance of landing proved to be very helpful, especially for landing on rough surfaces. We anticipate that multiple scouting flights might be needed for Dragonfly before landing in the Selk crater vicinity, as Titan lacks high-resolution pre-mission surface data. Lastly, we recommend further work simulating DragonCam imaging campaigns in Titan analogue terrain in preparation for Dragonfly operations. Additionally, training operations personnel in such terrain would help enhance Dragonfly science operations in the future. Continued mission simulations conducted in terrestrial analogue terrain can further provide insights into informing future UAS mission operations, representing the new frontier for planetary exploration.

## 4.6 References

- Balaram J, Aung MM, Golombek MP (2021) The Ingenuity Helicopter on the Perseverance Rover. *Space Sci Rev* 217:1–11.  
<https://doi.org/10.1007/s11214-021-00815-w>
- Bapst J, Parker TJ, Balaram J, et al (2021) Mars Science Helicopter: Compelling Science Enabled by an Aerial Platform. White paper.
- Barnes JW, Turtle EP, Trainer MG, et al (2021) Science Goals and Objectives for the Dragonfly Titan Rotorcraft Relocatable Lander. *Planet Sci J* 2:130.  
<https://doi.org/10.3847/PSJ/abfdcf>
- Bonnefoy LE, Lucas A, Hayes AG, et al (2022) Composition, Roughness, and Topography from Radar Backscatter at Selk Crater, the Dragonfly Landing Site. *Planet Sci J* 3:201. <https://doi.org/10.3847/PSJ/ac8428>
- Burr DM, McEwen AS, Sakimoto SEH (2002) Recent aqueous floods from the Cerberus Fossae, Mars. *Geophys Res Lett* 29:13-1–13–4.  
<https://doi.org/10.1029/2001GL013345>
- Burr DM, Wilson L, Bargery AS (2009). Floods from fossae: a review of Amazonian-aged extensional-tectonic megaflood channels on Mars. In *Megaflooding on Earth and Mars*. Cambridge Univ Press, pp. 194–208.  
<https://doi.org/10.1017/CBO9780511635632.010>
- Cannon HN, Stoker CR, Dunagan SE, et al (2007) MARTE: Technology development and lessons learned from a Mars drilling mission simulation. *J Field Robotics* 24:877– 905. <https://doi.org/10.1002/rob.20224>
- Cousins CR (2011) Volcano-ice interaction: a haven for life on Mars? *Astron Geophys* 52:1.36–1.38. <https://doi.org/10.1111/j.1468-4004.2011.52136.x>

- Cousins CR, Crawford IA (2011) Volcano-Ice Interaction as a Microbial Habitat on Earth and Mars. *Astrobiology* 11:695–710.  
<https://doi.org/10.1089/ast.2010.0550>
- Diniega S, Banfield D, Johnson J, et al (2019) Preparation for the Planetary Decadal Survey: The 2018 MEPAG Goals Document and Plans for 2019 Updates. Authorea. <https://doi.org/10.1002/essoar.10500792.1>
- Fagents SA, Thordarson T (2007) Rootless volcanic cones in Iceland and on Mars. In: *The Geology of Mars: Evidence from Earth-Based Analog* p. 151.  
<https://doi.org/10.1017/CBO9780511536014.007>
- Farley KA, Williford KH, Stack KM, et al (2020) Mars 2020 Mission Overview. *Space Sci Rev* 216:142. <https://doi.org/10.1007/s11214-020-00762-y>
- Grant J, Amend J, Steele A, et al (2006) Mars Science Goals, Objectives, Investigations, and Priorities: 2006. White paper
- Gwizd S, Stack KM, Calef F, et al (2023) Rover-Aerial Vehicle Exploration Network (RAVEN): Mission Planning, Implementation, and Results from the 2022 Rover-Only Field Campaign at Holuhraun, Iceland. In: *LPI Contributions*. p 1748
- Hamilton CW. (2015) Team gets firsthand look at the new Holuhraun eruption site. *Eos* 96. <https://doi.org/10.1029/2015EO041197>
- Hamilton CW, Voigt JRC, Zanetti M, et al (2023) The Holuhraun Region of Iceland as a High-Fidelity Planetary Analog Site for Science and Exploration. In: *LPI Contributions*. p 3010
- Jaeger WL, Keszthelyi LP, McEwen AS, et al (2007) Athabasca Valles, Mars: A lava-draped channel system. *Science*, 317:1709–1711.  
<https://doi.org/10.1126/science.1143315>

- Jaeger WL, Keszthelyi LP, Skinner JA (2010) Emplacement of the youngest flood lava on Mars: A short, turbulent story. *Icarus* 205:230–243.  
<https://doi.org/10.1016/j.icarus.2009.09.011>
- Johnson W, Withrow S, Young LA, et al (2020) Mars Science Helicopter Conceptual Design. NASA Report TM—2020–220485
- Lanagan PD, McEwen AS, Keszthelyi LP, et al (2001) Rootless cones on Mars indicating the presence of shallow equatorial ground ice in recent times. *Geophys Res Lett* 28:2365–2367. <https://doi.org/10.1029/2001GL012932>
- Lorenz R (2022a) Planetary Exploration with Ingenuity and Dragonfly: Rotary-wing Flight on Mars and Titan. American Institute of Aeronautics and Astronautics, Incorporated
- Lorenz RD (2022b) Sand Transport on Titan: A Sticky Problem. *Geophys Res Lett* 49: e2022GL098375. <https://doi.org/10.1029/2022GL098375>
- Lorenz RD, Turtle EP, Barnes JW, et al (2018) Dragonfly: A rotorcraft lander concept for scientific exploration at titan. *Johns Hopkins APL Tech Dig* 34:374–387
- Lorenz RD, MacKenzie SM, Neish CD, et al (2021) Selection and Characteristics of the Dragonfly Landing Site near Selk Crater, Titan. *Planet Sci J* 2:24.  
<https://doi.org/10.3847/PSJ/abd08f>
- Marion CL, Osinski GR, Bourassa M, et al (2020) Overview of the CanMoon Lunar Sample Return Analogue Mission. In: *LPI Contributions*. p 2349
- McEwen AS, Eliason EM, Bergstrom JW, et al (2007) Mars reconnaissance orbiter's high resolution imaging science experiment (HiRISE). *J Geophys Res Planets* 112:1–40. <https://doi.org/10.1029/2005JE002605>
- McEwen AS, Preblich BS, Turtle EP, et al (2005) The rayed crater Zunil and interpretations of small impact craters on Mars. *Icarus* 176:351–381.  
<https://doi.org/10.1016/J.ICARUS.2005.02.009>

- Muirhead BK, Nicholas A, Umland J (2020) Mars Sample Return Mission Concept Status. In: IEEE Aerospace Conference. pp 1–8  
<https://doi.org/10.1109/AERO47225.2020.9172609>
- Neish CD, Lorenz RD, Turtle EP, et al (2018) Strategies for Detecting Biological Molecules on Titan. *Astrobiology* 18:571–585.  
<https://doi.org/10.1089/ast.2017.1758>
- Neish CD, Lorenz RD, MacKenzie S, Hedgepeth JE (2021) The Haughton Impact Structure as a Titan Impact Crater Analogue: Applications to the Dragonfly Mission. In: Workshop on Terrestrial Analogs for Planetary Exploration. p 8007
- Nelson T, Wiens R, Clegg S, et al (2020) The SuperCam Instrument for the Mars 2020 Rover. In: IEEE Aerospace Conference. pp 1–12  
<https://doi.org/10.1109/AERO47225.2020.9172661>
- Osinski GR, Lee P, Spray JG, et al (2005) Geological overview and cratering model for the Haughton impact structure, Devon Island, Canadian High Arctic. *Meteorit Planet Sci* 40:1759–1776. <https://doi.org/10.1111/j.1945-5100.2005.tb00145.x>
- Osinski G, Marion C, Morse Z, et al (2019a) Returning to the Moon: CanMoon and the Role of Analogue Missions. In: AGU Fall Meeting Abstracts, pp P33C-08
- Osinski GR, Battler M, Caudill CM, et al (2019b) The CanMars Mars Sample Return analogue mission. *Planet Space Sci* 166:110–130.  
<https://doi.org/10.1016/J.PSS.2018.07.011>
- Plescia JB (2003) Cerberus Fossae, Elysium, Mars: a source for lava and water. *Icarus* 164:79–95. [https://doi.org/10.1016/S0019-1035\(03\)00139-8](https://doi.org/10.1016/S0019-1035(03)00139-8)
- Radebaugh J (2009) Titan’s sticky dunes? *Nat Geosci* 2:608–609.  
<https://doi.org/10.1038/ngeo623>

- Rossi AP, van Gasselt S (2018) Ground Truth. In: Planetary Geology. Springer International Publishing, pp 71–100.  
[https://doi.org/10.1007/978-3-319-65179-8\\_5](https://doi.org/10.1007/978-3-319-65179-8_5)
- Saez A, Manzo M, Ciarcià M (2021) Mars Drone Configurations And Approaches to Rotor Design: A Review. In: ASME International Mechanical Engineering Congress and Exposition, IMECE2021-71876.  
<https://doi.org/10.1115/IMECE2021-71876>
- Steven MD (1987) Ground truth An underview. Int J Remote Sens 8:1033–1038.  
<https://doi.org/10.1080/01431168708954745>
- Turtle EP, Lorenz RD (2021) The Dragonfly Mission to Titan: Technological Development and Science Converge to Enable New Exploration. Bridge 51:59–66
- Voigt JRC, Hamilton CW, Scheidt SP, et al (2021) Geomorphological characterization of the 2014–2015 Holuhraun lava flow-field in Iceland. J Volcanol Geotherm Res 419:107278. <https://doi.org/10.1016/J.JVOLGEORES.2021.107278>
- Voigt JRC, Hamilton CW, Stack KM (2023) The 2014-2015 Holuhraun Lava Flow-Field in Iceland as an Analog Site for Young Volcanic Terrains in Elysium Planitia, Mars. In: LPI Contributions. p 1646

## Chapter 5

### 5 Discussion and Conclusions

#### 5.1 Discussion

In this thesis, we used impact craters as a tool to investigate active surface processes on Titan. Our focus on Titan stems from its strong astrobiological significance, marked by the presence of a thick atmosphere and surface liquids. Notably, it is the target for NASA's Dragonfly mission, which aims to study Titan's prebiotic chemistry. Our choice of craters as a focal point is grounded in their role as markers for processes that modify Titan's surface. **Chapter 2** delves into the radar image analysis of terrestrial craters as analogues to constrain the crater population on Titan. Many of these craters are challenging to observe via orbit due to their extensive degradation. **Chapter 3** builds on this analysis, attempting to quantify the level of erosion that may have occurred at Titan's craters. We employed numerical modeling to simulate the depths of fresh craters and compared them to depths observed by Cassini. Finally, we presented insights from an analogue mission simulation conducted using a UAS, outlining how these lessons might be applicable in the context of Dragonfly operations in **Chapter 4**. Here, we discuss the high-level conclusions of these three chapters.

##### 5.1.1 Cratering as a Window into Surface Processes

###### 5.1.1.1 Constraining the Crater Population on Titan

In Chapter 2, we undertook the task of characterizing the visibility of non-buried terrestrial craters in radar images, revealing that approximately 50% of craters are not visible. We applied this finding to Titan, aiming to constrain the crater population and, consequently, estimate its surface age. To make this translation, we assumed that dominant processes responsible for erasing craters on both Earth and Titan are fluvial and aeolian erosion. However, we acknowledge the presence of other exogenic processes, such as impacts into marine environments, a potential rapid resurfacing mechanism on Titan in the recent past, and/or viscous relaxation, all of which contribute to making craters



unobservable via orbit (Korycansky & Zahnle, 2005; Neish et al., 2013; Neish & Lorenz, 2014; Neish et al., 2016; Schurmeier & Dombard, 2018; Schurmeier et al., 2023).

Furthermore, we recognize that the terrestrial radar datasets used in our study, while not operating on the same centimeter scale, are comparable for the qualitative characterization of craters. Working under these assumptions, we conclude that approximately 50% of craters on Titan are "missing" from its crater catalog. Assuming a constant impact rate on Titan, we scale this to the surface age, suggesting that Titan is likely twice as old as the crater counting-derived surface age of 200 Ma to 1 Ga (Lorenz et al., 2007; Wood et al., 2010; Neish & Lorenz, 2012; Hedgepeth et al., 2020). However, it is essential to note that this likely serves as a lower limit because Titan lacks global SAR coverage, potentially leaving many more craters unidentified. This holds true for Earth as well, where numerous craters have eroded to the point of remaining unidentified.

#### 5.1.1.2 Simulating the Formation of Fresh Craters on Titan

In Chapter 2, our investigation revealed that craters on Titan undergo substantial erosion, rendering them unrecognizable and thus, excluded from the crater database. Building on this in Chapter 3, our goal was to constrain the extent of erosion that may have occurred at Titan's craters. However, identifying fresh or 'uneroded' craters morphologies on Titan is challenging due to erosional processes modifying the surface. Previous studies have compared Titan's craters to those on Ganymede (Neish et al., 2016; Hedgepeth et al., 2020). However, the presence of methane clathrate in Titan's ice crust results in a higher thermal gradient, making Ganymede (composed mainly of pure water-ice) a less suitable comparison.

In our work, we used iSALE to simulate formation of fresh craters, incorporating the thermal properties associated with methane clathrates. Our results suggest that a thermal gradient of 10 K/km (due to the presence of clathrates) produces craters comparable in depth to some of the freshest craters on Titan observed in Cassini topography data (Hedgepeth et al., 2020). From this, we calculated a lower bound for a fluvial erosion rate of  $<1.6 \times 10^{-6}$  m/yr over the age of Titan's atmosphere ( $\sim 10^8$  yr; Hörst, 2017).

However, our study is limited to investigating the influence of only the thermal properties of on the resulting crater morphometry. Other studies considering the material strength properties of methane clathrates (Wakita et al., 2022), suggest that a methane-saturated layer or a layer of pure methane clathrate overlying the ice crust would produce shallower craters. Additionally, factors such as viscous relaxation may also contribute to the shallowing of craters on Titan (Dombard & McKinnon, 2000, 2006; Schurmeier and Dombard, 2018; Schurmeier et al., 2023; Bland & Bray, 2023). Therefore, future work that couples these different shallowing factors would provide improved estimates on the level of erosion. The Dragonfly mission to Titan (e.g. Turtle et al., 2020) will have the capability to investigate the subsurface structure at Selk crater, providing constraints on the surface composition and thermal properties – parameters used in the crater formation simulations.

### 5.1.2 Informing Operational Strategies for Dragonfly

The Dragonfly mission to Titan is set to explore Selk crater. The preparation for surface operations is pivotal in optimizing the scientific returns of the mission, offering further insights into the impact cratering process on Titan—topics relevant to the discussions presented in Chapters 2 and 3.

We conducted an analogue mission simulation at the Holuhraun lava flow in Iceland, chosen as an analogue for Mars, using a UAS platform capable of in-flight and landed science, similar to Dragonfly. Although the simulation was designed with the aim of informing future UAS Mars missions, we can draw parallels to the Dragonfly mission. Our findings highlight that oblique in-flight imaging provides excellent contrast, facilitating the identification of safe landing and sampling locations.

Additionally, we anticipate that Dragonfly may need to conduct multiple scouting flights to gather sufficient hazard data before landing in rougher areas within the Selk crater vicinity. It is important to note that these results and applications are specific to a Mars volcanic analogue terrain. Future work involving simulations of imaging campaigns in a Titan analogue terrain would be valuable in refining and informing science operations for Dragonfly.

## 5.2 Conclusions

This thesis focuses on understanding the impact cratering process on Titan. In Chapter 2, we investigated terrestrial craters in radar images as analogues for impact craters on Titan. Through this exploration, we gained insights into interpreting how eroded craters may appear in remote sensing data, specifically SAR and topography data. Additionally, by numerically modeling fresh impact craters on Titan, we inferred the level of erosion affecting craters. Lastly, in Chapter 4, we garnered insights into UAS exploration strategies and their potential applicability to Dragonfly surface operations.

Combining the lessons learned in this thesis, future work could explore conducting fieldwork in a Titan analogue terrain, such as the Haughton impact structure in the Canadian High Arctic (e.g., Neish et al., 2018, 2021). Simulating imagery likely to be obtained by Dragonfly can provide improved insights into the best operational practices for exploring Selk crater.

This work, investigating impact craters on Titan, constitutes a small part of the larger effort to study Titan comprehensively. Future missions to Titan, such as Dragonfly, will play a crucial role in validating these previous studies and providing better constraints on Titan's geologic history and processes. Our efforts to study Titan would be further enhanced with a future orbiter mission providing high-resolution global data.

### 5.3 References

- Bland MT, Bray VJ (2023) Large Shallow Craters on Callisto and Ganymede as an Inevitable Result of Viscous Relaxation. In: LPI Contributions p 2104
- Dombard AJ, McKinnon WB (2000) Long-term retention of impact crater topography on Ganymede. *Geophys Res Lett* 27:3663–3666.  
<https://doi.org/https://doi.org/10.1029/2000GL011695>
- Dombard AJ, McKinnon WB (2006) Elastoviscoplastic relaxation of impact crater topography with application to Ganymede and Callisto. *J Geophys Res Planets* 111:1–22. <https://doi.org/10.1029/2005JE002445>
- Hedgepeth JE, Neish CD, Turtle EP, et al (2020) Titan's impact crater population after Cassini. *Icarus* 344:113664. <https://doi.org/10.1016/j.icarus.2020.113664>
- Hörst SM (2017) Titan's atmosphere and climate. *J Geophys Res Planets* 122:432–482.  
<https://doi.org/10.1002/2016JE005240>
- Korycansky DG, Zahnle KJ (2005) Modeling crater populations on Venus and Titan. *Planet Space Sci* 53:695–710. <https://doi.org/10.1016/J.PSS.2005.03.002>
- Lorenz RD, Wood CA, Lunine JJ, et al (2007) Titan's young surface: Initial impact crater survey by Cassini RADAR and model comparison. *Geophys Res Lett* 34:1–5.  
<https://doi.org/10.1029/2006GL028971>
- Neish CD, Kirk RL, Lorenz RD, et al (2013) Crater topography on Titan: Implications for landscape evolution. *Icarus* 223:82–90.  
<https://doi.org/https://doi.org/10.1016/j.icarus.2012.11.030>
- Neish CD, Lorenz RD (2012) Titan's global crater population: A new assessment. *Planet Space Sci* 60:26–33. <https://doi.org/10.1016/j.pss.2011.02.016>

- Neish CD, Lorenz RD (2014) Elevation distribution of Titan's craters suggests extensive wetlands. *Icarus* 228:27-34. <https://doi.org/10.1016/j.icarus.2013.09.024>
- Neish CD, Lorenz RD, MacKenzie S, Hedgepeth JE (2021) The Haughton Impact Structure as a Titan Impact Crater Analogue: Applications to the Dragonfly Mission. In: Workshop on Terrestrial Analogs for Planetary Exploration. p 8007
- Neish CD, Lorenz RD, Turtle EP, et al (2018) Strategies for Detecting Biological Molecules on Titan. *Astrobiology* 18:571–585.  
<https://doi.org/10.1089/ast.2017.1758>
- Neish CD, Molaro JL, Lora JM, et al (2016) Fluvial erosion as a mechanism for crater modification on Titan. *Icarus* 270:114–129.  
<https://doi.org/10.1016/j.icarus.2015.07.022>
- Schurmeier LR, Brouwer G, Fagents S, et al (2023) Crater relaxation caused by an insulating methane clathrate crust on Titan. In: LP Contributions p 2813
- Schurmeier LR, Dombard AJ (2018) Crater relaxation on Titan aided by low thermal conductivity sand infill. *Icarus* 305:314–323.  
<https://doi.org/10.1016/J.ICARUS.2017.10.034>
- Turtle EP, Trainer MG, Barnes JW, et al (2020) Dragonfly: In situ exploration of Titan's organic chemistry and habitability. In: LPI Contributions p 2288
- Wakita S, Johnson BC, Soderblom JM, et al (2022) Methane-saturated Layers Limit the Observability of Impact Craters on Titan. *Planet Sci J* 3:50.  
<https://doi.org/10.3847/psj/ac4e91>
- Wood CA, Lorenz R, Kirk R, et al (2010) Impact craters on Titan. *Icarus* 206:334–344.  
<https://doi.org/10.1016/J.ICARUS.2009.08.021>

## Appendices

### Appendix A: iSALE asteroid input file

#ISINP

-----  
 --- this is the new input file used by iSALE versions of v7.0 and higher

----- General Model Info -----

VERSION	__DO NOT MODIFY__	: 4.1
DIMENSION	dimension of input file	: 2
PATH	Data file path	: ./
MODEL	Modelname	: ice50km_dimp5km_temp5Km

----- Mesh Geometry Parameters -----

GRIDH	horizontal cells	: 0	: 200	: 100
GRIDV	vertical cells	: 100	: 350	: 100
GRIDEXT	ext. factor	: 1.03D0		
GRIDSPC	grid spacing (m)	: 2.5D+2		
CYL	Cylind. geometry	: 1.0D0		
GRIDSPCM	max. grid spacing	: -40.D0		

----- Global setup parameters -----

S_TYPE	setup type	: DEFAULT
T_SURF	Surface temp	: 94.D0
R_PLANET	planet radius (m)	: 2.576D+06
GRAV_V	gravity	: -1.35D0
DTDZSURF	Near-surface dT/dz (K/m)	: 5.0D-03
D_LITH	Lithospheric thickness (m)	: 32.404D+03
LP_TOLER	Tolerance in LP iteration	: 1.D-9
	Minimum density in LP	
LP_ROLOW	iter.	: 0.8D0
	Maximum density in LP	
LP_ROHIGH	iter.	: 1.25D0

----- Projectile ("Object") Parameters -----

OBJNUM	number of objects	: 1
OBJRESH	CPPR horizontal	: 10
OBJVEL	object velocity (m/s)	: -11.0D3
OBJMAT	object material	: H2O_ice
OBJTYPE	object type	: SPHEROID

----- Target Parameters -----

LAYNUM	layers number	: 2	
LAYPOS	layer position	: 150	: 350
LAYMAT	layer material	: water__	: H2O_ice
LAYTPROF	layer thermal profile	: CONST	: CONDCONVCAP

----- Time Parameters -----

```

DT          initial time increment      : 1.00D-4
DTMAX       maximum timestep           : 5.0D+1
TEND        end time                   : 6.0D3
DTSAVE      save interval              : 20.0D+0
TDUMP       dump interval              : -23.9D0
----- Ac. Fluid. Parameters (see also material.inp) -----
TOFF        toff                      : 200.D0
CVIB        c_vib                     : 0.2D0
VIB_MAX     Max. vib.vel.              : 200.0
VIBDAMP     Thermal damping            : 0
----- Boundary Condition Parameters -----
BND_L       left                      : FREESLIP
BND_R       right                     : FREESLIP
BND_B       bottom                    : NOSLIP
BND_T       top                       : OUTFLOW
----- Numerical Stability Parameters -----
AVIS        art. visc. linear          : 0.2D0
AVIS2       art. visc. quad.           : 1.0D0
ROCUTOFF    density lower limit (d=5)  : 100.D0
----- (Material) Model parameters (global) -----
STRESS      Consider stress            : 1
TENSILE     Consider tensile failure   : 0
----- Tracer Particle Parameters -----
TR_QUAL     integration qual.          : 1
TR_SPCH     tracer spacing X           : -1.D0      : -1.D0      : -1.D0
TR_SPCV     tracer spacing Y           : -1.D0      : -1.D0      : -1.D0
TR_VAR      add tracer fields          : #TrP-TrT#
----- Data Saving Parameters -----
QUALITY     Compression rate           : -50
            : #Den-Tmp-Pre-Sie-Yld-Dam-TPS-Vis-VEL-PVb-
VARLIST     List of variables          : YAc-VSt#
-----
<<END

```

## Appendix B: iSALE material input file

#ISMAT

```

-----
MATNAME      Material name           : H2O_ice           : water__
EOSNAME      EOS name              : ice_____       : water__
EOSTYPE      EOS type             : tillo            : aneos
STRMOD       Strength model    : ICE              : HYDRO
DAMMOD       Damage model     : IVANOV           : NONE
ACFL         Acoustic fluidization : BLOCK           : NONE
PORMOD       Porosity model    : NONE             : NONE
THSOFT       Thermal softening  : OHNAKA          : NONE
LDWEAK       Low density weakening : POLY            : NONE
VISCO        Viscosity model    : NONE             : NONE
-----general parameters-----
POIS         pois           : 3.3000D-01       : 5.0000D-01
-----thermal parameters-----
TMELTO       tmelt0         : 2.7300D+02       : 2.7300D+02
CHEAT        C_heat         : 2.1000D+03       : 4.2200D+03
TFRAC        tfrac          : 1.2000D+00       : 1.5000D+00
ASIMON       a_simon        : 1.2530D+09       : 2.3400D+10
CSIMON       c_simon        : 3.0000D+00       : 1.5000D+00
-----shear strength of intact material-----
YINTO        yint0          : 1.0000D+07       : XXXXX
FRICINT      fricint        : 2.0000D+00       : XXXXX
YLIMINT      ylimint       : 1.1000D+08       : XXXXX
-----shear strength of damaged material-----
YDAMO        ydam0 (ycoh)    : 1.0000D+04       : XXXXX
FRICDAM      fricdam        : 6.0000D-01       : XXXXX
YLIMDAM      ylimdam       : 1.1000D+08       : XXXXX
-----
IVANOV_A     Damage parameter        : 1.00D-04         : XXXXX
IVANOV_B     Damage parameter        : 1.00D-11         : XXXXX
IVANOV_C     Damage parameter        : 3.00D+08         : XXXXX
-----acoustic fluidization (block model)-----
GAMETA       gam_eta         : 1.35677D-1       : XXXXX
GAMBETA      gam_beta        : 3.55401D+2       : XXXXX
-----
<<END

```



**Appendix C: Characteristics of all 132 non-buried terrestrial craters. The last three columns are the characterizations made in this study regarding the crater's visibility in radar (C-band and L-band) and DEM.**

Crater	Latitude	Longitude	Country	Target rock type (Crystalline, Sedimentary, Mixed)	Apparent diameter (km)	Age Range (Ma)	Visible in C-band?	Visible in L-band?	Visible in DEM?
Acraman	-32.1	135.27	Australia	C	90	541 - 635	Y	Y	
Agoudal	31.98	5.51	Morocco	S	0.5	<168.5	N	N	N
Amelia Creek	-20.51	134.53	Australia	M	20	660 - 1660	N	N	N
Amguid	26.5	4.23	Algeria	S	0.45	0.01 - 0.1	Y	Y	
Aorounga	19.06	19.15	Chad	S	16	0.00350 - 383	Y	Y	
Aouelloul	20.15	-12.41	Mauritania	S	0.39	3.1 ± 0.3	N	no data	Y
Araguainha	-16.47	-52.59	Brazil	M	40	248 - 264	no data	N	N
B.P. Structure	25.19	24.2	Libya	S	3.2	<120	Y	Y	
Barringer	35.2	-111.1	U.S.A.	S	1.19	0.0611 ± 0.0048	Y	Y	
Beaverhead	44.36	-113	U.S.A.	M	60	470 - 900	N		N
Beyenchime-Salaatin	71.5	123.3	Russia	S	8	1.8 - 66	N		N
Bigach	48.3	82	Kazakhstan	M	8	6 ± 3	Y		
Bosumtwi	6.3	-1.25	Ghana	C	10.5	1.13 ± 0.1	Y	Y	
Boxhole	-22.37	135.12	Australia	C	0.185	0.030 ± 0.005	N	N	N
Campo del Cielo	-27.38	-61.42	Argentina	S	0.004	0.00338 - 0.00405	N	N	N
Carancas	-16.4	-69.03	Peru	S	0.0135	Recent	N	N	N
Carswell	58.27	-109.3	Canada	M	39	481.5 ± 0.8	N	N	Y
Cerro do Jarau	-30.2	-56.53	Brazil	M	13.5	≤135	Y	Y	Y

Charlevoix	47.32	-70.18	Canada	M	70	430 - 453	Y	N	Y
Chiylil	49.1	57.51	Kazakhstan	S	5.5	41 - 56	N	N	N
Chukcha	75.42	97.48	Russia	M	6	<70	N		N
Cleanskin	-18.17	137.94	Australia	S	15	520 - 1400	N	N	Y
Clearwater East	56.5	-74.7	Canada	C	26	460 - 470	Y	Y	
Clearwater West	56.14	-74.3	Canada	M	36	286.2 ± 2.6	Y	Y	
Colonia	-23.52	-46.42	Brazil	C	3.6	2.5 - 36	Y	Y	
Connolly Basin	-23.32	124.45	Australia	S	9	23 - 66	Y		
Couture	60.8	-75.2	Canada	C	8	429 ± 25	Y	Y	
Crooked Creek	37.5	-91.23	U.S.A.	S	7	323 - 485	N	N	N
Dalgaranga	-27.38	117.17	Australia	C	0.02	<0.003	N	N	N
Decaturville	37.54	-92.43	U.S.A.	M	6	< 323	N	N	Y
Dellen	61.48	16.48	Sweden	C	19	140.82 ± 0.51	Y	Y	
Dhala	25.3	78.13	India	C	11	1700 - 2500	Y	Y	
Douglas	42.68	-105.47	U.S.A	S	0.073	~280	N	N	N
El'gygytgyn	67.3	172.5	Russia	C	18	3.65 ± 0.08	Y		
Flynn Creek	36.17	-85.4	U.S.A.	S	3.8	~382	N	N	N
Foelsche	-16.4	136.47	Australia	S	6	520 - 1496	Y	Y	
Gardnos	60.39	9	Norway	C	5	546 ± 5	N	no data	N
Glikson	-23.59	121.34	Australia	S	19	<513	Y	Y	
Glover Bluff	43.58	-89.32	U.S.A.	S	8	<485	N	N	N
Goat Paddock	-18.2	126.4	Australia	S	5	48 - 56	Y	Y	
Gosses Bluff	-23.49	132.19	Australia	S	32	165 - 383	Y	Y	
Gow	56.27	-104.29	Canada	C	4	196.8 ± 9.9	Y	Y	
Goyder	-13.9	135.2	Australia	S	7	150 - 1325	Y	Y	
Gweni-Fada	17.25	21.45	Chad	S	22	<383	Y	Y	

Haughton	75.22	-89.41	Canada	M	23	31.04 ± 0.37	Y		
Haviland	37.35	-99.1	U.S.A.	S	0.01	0.02 ± 0.002	N	N	N
Henbury	-24.34	133.08	Australia	S	0.15	0.0042 ± 0.0019	N	N	N
Hickman	-23.03	119.68	Australia	M	0.26	0.01 - 0.1	N	N	Y
Hummeln	57.22	16.19	Sweden	M	1.2	~465	Y	no data	
Ile Rouleau	50.41	-73.53	Canada	S	4	0.011 - 1800	N	N	N
Janisjarvi	61.58	30.55	Russia	C	14	687 ± 5	Y	Y	
Jebel Waqf as Suwwan	31.03	36.48	Jordan	S	5.5	2.6 - 30	Y	Y	
Jeokjung-Chogye Basin	35.55	128.27	South Korea	S	0.0001	0.030 - 0.063	N	N	N
Kaalijarv	58.24	22.4	Estonia	S	0.11	0.003237 ± 0.000010	N	N	N
Kalkkop	-32.43	24.34	South Africa	S	0.64	0.250 ± 0.050	Y	no data	
Kamil	22.01	26.05	Egypt	S	0.045	<0.004	N	N	N
Kara-Kul	39.1	73.27	Tajikistan	C	52	<60	Y	Y	
Karikkoselka	63.13	25.15	Finland	C	1.5	230 - 260	Y	Y	
Karla	54.54	48	Russia	S	12	4 - 6	N	N	N
Kentland	40.45	-87.27	U.S.A.	S	7	1 - 300	N	N	N
Kgagodi	-22.29	27.35	Botswana	C	3.4	≤180	N	N	N
La Moinerie	57.26	-66.37	Canada	C	8	453 ± 5	Y	Y	
Lappajarvi	63.12	23.42	Finland	M	23	77.85 ± 0.78	Y	Y	
Lawn Hill	-18.4	138.39	Australia	M	16.8	476 ± 8	Y	Y	
Liverpool	-12.24	134.3	Australia	S	1.6	541 - 1870	N	N	Y
Lonar	19.58	76.31	India	C	1.83	0.576 ± 0.047	Y	Y	
Luizi	-10.1	27.55	Congo	S	15	≤573	Y	Y	
Malingen	62.1	16.57	Sweden	C	1	~455	N	no data	N
Manicouagan	51.23	-68.42	Canada	M	10	215.40 ± 0.16	Y	Y	

Matt Wilson	-15.3	131.11	Australia	S	7.5	<1344	N	N	N
Middlesboro	36.37	-83.44	U.S.A.	S	5.5	<299	N	N	Y
Mien	56.25	14.52	Sweden	C	9	~121	Y	no data	
Mishina Gora	58.4	28	Russia	M	4	<360	N	N	N
Mistastin	55.53	-63.18	Canada	C	28	37.83 ± 0.05	Y	Y	
Monturaqui	-23.56	-68.17	Chile	C	0.46	0.663 ± 0.023	N	N	N
Morasko	52.29	16.54	Poland	S	0.1	~0.005	N	no data	N
Mount Toondina	-27.57	135.22	Australia	S	4	<125	Y	Y	
New Quebec	61.17	-73.4	Canada	C	3.44	1.4 ± 0.1	Y	Y	
Nicholson	62.4	-102.41	Canada	M	12.5	387 ± 5	N		N
Oasis	24.35	24.24	Libya	S	15.6	<120	Y	Y	
Odessa	31.45	-102.29	U.S.A.	S	0.16	<0.05	N	N	N
Ouarzkiz	29	-7.33	Algeria	S	3.5	65 - 345	Y	Y	
Paasselkä	62.2	29.5	Finland	M	10	231.0 ± 2.2	N	N	N
Pantasma	13.37	-85.95	Nicaragua	C	14	0.815 ± 0.011	Y	Y	
Pilot	60.17	-111.1	Canada	C	6	450 ± 2	Y	Y	
Popigai	71.4	111.4	Russia	M	100	36.63 ± 0.92	N		Y
Presqu'île	49.43	-74.48	Canada	C	15	<2729	Y	Y	
Ramgarh	25.33	76.62	India	S	10	165 - 750	Y	Y	
Riachao Ring	-7.43	-46.39	Brazil	S	4	<299	N	N	N
Ries	48.53	10.37	Germany	M	24	14.808 ± 0.038	Y	Y	
Ritland	59.41	6.25	Norway	M	2.7	500 - 541	N	no data	N
Rochechouart	45.5	0.56	France	C	32	206.92 ± 0.32	N	N	N
Rock Elm	44.72	-92.14	U.S.A.	S	6.5	458 - 485	N	N	Y
Roter Kamm	-27.46	16.18	Namibia	M	2.5	3.8 ± 0.3	Y	Y	
Saaksjarvi	61.24	22.24	Finland	C	5	602 ± 17	Y	Y	

Saarijarvi	65.17	28.23	Finland	C	2	<600	Y		
Santa Fe	35.45	-105.55	U.S.A.	C	13	350 - 1472	N	N	N
Santa Marta	-10.17	-45.23	Brazil	S	10	<100	Y	Y	
Serpent Mound	39.2	-83.24	U.S.A.	S	8	<359	N	N	N
Serra da Cangalha	-8.05	-46.51	Brazil	S	13.7	≤250	Y	Y	
Shoemaker	-25.52	120.53	Australia	M	30	568 - 1300	Y	Y	
Shunak	47.12	72.42	Kazakhstan	C	2.8	7 - 17	Y	Y	
Sierra Madera	30.36	-102.55	U.S.A.	S	20	<113	Y	Y	
Sikhote Alin	46.07	134.4	Russia	C	0.02	Recent	N	N	N
Siljan	61.05	15	Sweden	M	75	380.9 ± 4.6	Y	no data	
Slate Islands	48.4	-87	Canada	M	30	~450	Y	Y	
Spider	-16.44	126.05	Australia	S	13	580 - 900	Y	Y	
Steinheim	48.41	10.04	Germany	S	3.8	~14.8	N	no data	Y
Strangways	-15.12	113.35	Australia	M	25	657 ± 43	Y	Y	
Suavjarvi	63.07	33.23	Russia	C	16	2200 - 2700	N	no data	N
Sudbury	46.36	-81.11	Canada	C	250	1849.53 ± 0.21	Y	Y	Y
Suvasvesi South	62.35	28.17	Finland	C	3.8	710 - 1880	N		N - poor coverage
Tabun-Khara-Obo	44.06	109.36	Mongolia	C	1.3	130 - 170	Y	Y	
Talemzane	33.19	4.02	Algeria	S	1.75	≤3	Y	limited data	Y
Tenoumer	22.55	10.24	Mauritania	C	1.9	1.57 ± 0.14	Y	Y	
Tin Bider	27.36	5.07	Algeria	S	6	<66	Y	no data	
Tsenkher	43.64	98.37	Mongolia	S	4.2	4.9 ± 0.9	Y	no data	
Tswaing	-25.24	28.05	South Africa	C	1.13	0.220 ± 0.104	Y	no data	
Tunnunik	72.28	-113.58	Canada	S	28	430 - 450	N		N

Upheaval Dome	38.26	-109.54	U.S.A.	S	5.2	<183	Y	Y	
Vargeao Dome	-26.48	-52.1	Brazil	M	12.4	123 ± 1.4	N	N	Y
Veevers	-22.58	125.22	Australia	S	0.05625	~0.004	N	N	N
Vista Alegre	-25.57	-52.41	Brazil	M	9.5	111 - 134	N	Y	Y
Vredefort	-27	27.3	South Africa	C	300	2023 ± 4	Y		
Wabar	21.3	50.28	Saudi Arabia	S	0.00014	Recent	no clear data – excluded from the study		
Wells Creek	36.23	-87.4	U.S.A.	S	13.7	100 - 323	N	N	N
Wetumpka	32.31	-86.1	U.S.A.	M	6.25	~83.5	N	N	N
Whitecourt	54	-115.36	Canada	S	0.04	<0.0011	N	N	N
Wolfe Creek	-19.1	127.47	Australia	S	0.8	0.120 ± 0.009	Y	Y	Y
Xiuyan	40.21	123.27	China	C	1.8	0.05 - 5	N	N	Y
Yarrabubba	-27.1	119.5	Australia	C	70	2229 ± 5	N	N	N
Yilan	46.38	129.31	China	C	30	0.0493 ± 0.0032	Y	N	Y
Zhamanshin	48.24	60.58	Kazakhstan	M	13	0.91 ± 0.14	N	limited data	N

**Appendix D: Results of the Zooniverse crowdsourcing campaign for 16 craters (plus 4 controls). For reference, in four areas with no craters (1) 35.3% of 34 users, (2) 61.3% of 31 users, (3) 64.7% of 34 users, and (4) 25.8% of 31 users identified no craters.**

Crater	Crater diameter [km]	No. of participants	No crater detected (%)	Correct Guesses for R Parameter (%)			Correct Guesses for X Parameter (%)		Correct Guesses for Y Parameter (%)	
				0.10	0.15	0.20	1 km	2 km	1 km	2 km
Amelia Creek	20	31	61	3.2	3.2	3.2	0.0	0.0	9.7	12.9
Aorounga	16	35	11	17.1	22.9	28.6	71.4	74.3	74.3	74.3
Aouelloul	0.39	33	15	0.0	0.0	0.0	0.0	0.0	0.0	3.0
Boxhole	0.185	33	70	0.0	3.0	3.0	0.0	0.0	0.0	0.0
B.P. Structure	3.2	33	9	45.5	78.8	103.0 <sup>a</sup>	75.8	75.8	72.7	75.8
Cleanskin	15	32	25	0.0	3.1	3.1	0.0	0.0	0.0	0.0
Goat Paddock	5	32	28	31.3	56.3	78.1	53.1	53.1	53.1	53.1
Gweni-Fada	22	32	16	46.9	62.5	65.6	65.6	71.9	68.8	71.9
Kara-Kul	52	30	63	3.3	3.3	6.7	3.3	3.3	3.3	6.7
Lonar	1.83	31	10	61.3	77.4	93.5	83.9	87.1	83.9	83.9
Matt Wilson	7.5	36	36	30.6	33.3	36.1	22.2	22.2	0.0	0.0
Ramgarh	10	30	37	20.0	26.7	40.0	30.0	30.0	30.0	30.0
Sääksjärvi	5	35	57	2.9	2.9	2.9	0.0	0.0	2.9	5.7
Serra da Cangalha	13.7	33	48	0.0	3.0	6.1	42.4	42.4	42.4	42.4
Sikhote Alin	0.02	35	54	0.0	0.0	0.0	2.9	5.7	0.0	2.9
Tenoumer	1.9	31	13	48.4	58.1	71.0	67.7	67.7	71.0	77.4
Volcano <sup>b</sup>		35	n/a	222.9 <sup>a</sup>	234.3 <sup>a</sup>	234.3 <sup>a</sup>	57.1	60.0	51.4	57.1

<sup>a</sup>People guessed the same location multiple times.

<sup>b</sup>This refers to the Emi Koussi volcano located in Chad. This circular feature is visible in the survey image for Aorounga crater. Since it appears circular with a bright rim, it is falsely identified as a crater along with Aorounga crater. It is only with topography data that one can decipher it as a topographic high feature, and therefore, not a crater.

## Curriculum Vitae

**Name:** Jahnvi Shah

### Post-secondary Education and Degrees

PhD student in Geophysics and Planetary Science 2018 – 2024  
University of Western Ontario

BSc in Physics and Astronomy 2013 – 2018  
University of Toronto

### Honours and Awards

Province of Ontario Graduate Scholarship 2021 – 2022

Technologies for Exo-Planetary Science (TEPS) program trainee 2020 – 2022  
Natural Sciences and Engineering Research Council of Canada

### Related Work Experience

Research Affiliate Program Intern May – Aug 2021  
Canadian Space Agency

Lunar Science and Exploration Summer Intern May – Aug 2019  
Lunar and Planetary Institute

Graduate Teaching Assistant Sept 2018 – Apr 2023  
Department of Earth Sciences, University of Western Ontario

### Publications

**Shah J**, Neish CD, Trozzo, S (2023) An analogue study of impact craters on Titan: Implications for Titan's surface age. *Icarus (Under review)*.

**Shah J**, Neish CD, Wakita S, Soderblom JM, Johnson BC, and Steckloff JK. The effect of the crustal thermal gradient on fresh crater morphometries on Titan. *Planetary Science Journal (in prep)*.

**Shah J**, Carr BB, Varnam M, Hadland N, Voigt JRC, Seelos K, Neish CD, and Hamilton CW. Lessons learned from the Rover-Aerial Vehicle Exploration Network (RAVEN) mission simulation: Applications for future operational procedures for Unoccupied Aircraft Systems (UAS) missions. *Planetary Science Journal (in prep)*.



- Wakita S, Johnson BC, Soderblom JM, **Shah J**, Neish CD, Steckloff JK (2023) Modeling the formation of Selk impact crater on Titan: Implications for Dragonfly. *Planetary Science Journal* 4:51. <https://doi.org/10.3847/PSJ/acbe40>
- Boazman SJ, **Shah J**, Harish, Gawronska AJ, Halim SH, Satyakumar AV, Gilmour CM, Bickel VT, Barrett N, Kring DA (2022) The Distribution and Accessibility of Geologic Targets near the Lunar South Pole and Candidate Artemis Landing Sites. *Planetary Science Journal* 3:275. <https://doi.org/10.3847/PSJ/aca590>
- Wakita S, Johnson BC, Soderblom JM, **Shah J**, Neish CD (2022) Methane-saturated layer limit the observability of impact craters on Titan. *Planetary Science Journal* 3:50. <https://doi.org/10.3847/psj/ac4e91>
- Gawronska AJ, Barrett N, Boazman SJ, Gilmour C, Halim S, Harish, McCanaan K, Satyakumar AV, **Shah J**, Meyer HM, Kring DA (2020) Geological Context and Potential EVA Targets at the Lunar South Pole. *Advances in Space Research* 66:1247–1264. <https://doi.org/10.1016/j.asr.2020.05.035>
- Halim S, Barrett N, Boazman SJ, Gawronska AJ, Gilmour C, Harish, McCanaan K, Satyakumar AV, **Shah J**, Kring DA (2020) Numerical modeling of the formation of Shackleton crater at the lunar south pole. *Icarus* 354, 113992. <https://doi.org/10.1016/j.icarus.2020.113992>